University of Windsor
Scholarship at UWindsor

Electronic Theses and Dissertations | Theses, Dissertations, and Major Papers

2008

The effects of freestream turbulence on the drag of a sphere

Niloofar Moradian
University of Windsor

Follow this and additional works at: https://scholar.uwindsor.ca/etd

Recommended Citation

Moradian, Niloofar, "The effects of freestream turbulence on the drag of a sphere" (2008). *Electronic Theses and Dissertations*. 8020.
https://scholar.uwindsor.ca/etd/8020

This online database contains the full-text of PhD dissertations and Masters' theses of University of Windsor students from 1954 forward. These documents are made available for personal study and research purposes only, in accordance with the Canadian Copyright Act and the Creative Commons license—CC BY-NC-ND (Attribution, Non-Commercial, No Derivative Works). Under this license, works must always be attributed to the copyright holder (original author), cannot be used for any commercial purposes, and may not be altered. Any other use would require the permission of the copyright holder. Students may inquire about withdrawing their dissertation and/or thesis from this database. For additional inquiries, please contact the repository administrator via email (scholarship@uwindsor.ca) or by telephone at 519-253-3000ext. 3208.

THE EFFECTS OF FREESTREAM TURBULENCE ON THE DRAG OF A SPHERE

by

Niloofar Moradian

A Thesis
Submitted to the Faculty of Graduate Studies
through the Department of Mechanical, Automotive & Materials Engineering
in Partial Fulfillment of Requirements for
the Degree of Master of Applied Science at the
University of Windsor

Windsor, Ontario, Canada
2008
© 2008 Niloofar Moradian

Library and Archives Canada

Published Heritage Branch

395 Wellington Street
Ottawa ON K1A 0N4
Canada

Bibliothèque et Archives Canada

Direction du Patrimoine de l'édition

395, rue Wellington
Ottawa ON K1A 0N4
Canada

Your file Votre référence
ISBN: 978-0-494-47024-4
Our file Notre référence
ISBN: 978-0-494-47024-4

NOTICE:
The author has granted a non-exclusive license allowing Library and Archives Canada to reproduce, publish, archive, preserve, conserve, communicate to the public by telecommunication or on the Internet, loan, distribute and sell theses worldwide, for commercial or non-commercial purposes, in microform, paper, electronic and/or any other formats.

The author retains copyright ownership and moral rights in this thesis. Neither the thesis nor substantial extracts from it may be printed or otherwise reproduced without the author's permission.

AVIS:
L'auteur a accordé une licence non exclusive permettant à la Bibliothèque et Archives Canada de reproduire, publier, archiver, sauvegarder, conserver, transmettre au public par télécommunication ou par l'Internet, prêter, distribuer et vendre des thèses partout dans le monde, à des fins commerciales ou autres, sur support microforme, papier, électronique et/ou autres formats.

L'auteur conserve la propriété du droit d'auteur et des droits moraux qui protège cette thèse. Ni la thèse ni des extraits substantiels de celle-ci ne doivent être imprimés ou autrement reproduits sans son autorisation.

In compliance with the Canadian Privacy Act some supporting forms may have been removed from this thesis.

While these forms may be included in the document page count, their removal does not represent any loss of content from the thesis.

Conformément à la loi canadienne sur la protection de la vie privée, quelques formulaires secondaires ont été enlevés de cette thèse.

Bien que ces formulaires aient inclus dans la pagination, il n'y aura aucun contenu manquant.

Canada

DECLARATION OF PREVIOUS PUBLICATION

This thesis includes 2 original papers that have been previously published/submitted for publication in peer reviewed journals, as follows:

Thesis Chapter	Publication title/full citation	Publication status*
Chapter 3 & 4	The Effects of Freestream Turbulence on the Drag Coefficient of a Sphere	Submitted to ETFS Journal
Chapter 3 & 4	Advancing the Drag Crisis of a Sphere via Integral Length Manipulation	Will be Submitted to JFE

I certify that I have obtained a written permission from the copyright owner(s) to include the above published material(s) in my thesis. I certify that the above material describes work completed during my registration as a graduate student at the University of Windsor.

I declare that, to the best of my knowledge, my thesis does not infringe upon anyone's copyright nor violate any proprietary rights and that any ideas, techniques, quotations, or any other material from the work of other people included in my thesis, published or otherwise, are fully acknowledged in accordance with the standard referencing practices. Furthermore, to the extent that I have included copyrighted material that surpasses the bounds of fair dealing within the meaning of the Canada Copyright Act, I certify that I have obtained a written permission from the copyright owner(s) to include such material(s) in my thesis.

I declare that this is a true copy of my thesis, including any final revisions, as approved by my thesis committee and the Graduate Studies office, and that this thesis has not been submitted for a higher degree to any other University or Institution.

ABSTRACT

The effects of freestream turbulence intensity and integral length scale as freestream turbulent parameters on the drag coefficient of a solid sphere were experimentally investigated in a closed-circuit wind tunnel. The Reynolds number, $Re = Ud/\nu$, was varied from 2.2×10^4 to 8×10^4 by using spheres of different sizes in addition to altering the freestream velocity, U. Two different kinds of spheres, PVC spheres with diameter d of 20, 51 and 102 mm and wooden spheres with diameter d of 20, 51, 65, 102, 140 and 210 mm, were used in Experiments I and II, respectively. The freestream turbulence intensity Tu and flow integral length scale Λ were manipulated by using orificed perforated plates. The proper combination of orificed perforated plate hole diameter, sphere size, and sphere location enabled the independent variations of turbulence intensity and relative integral length scale (Λ/d) from 1.8% to 10.7% and from 0.1 to 2.6, respectively at each studied Reynolds number in Experiment I, and in Experiment II, the independent variations of turbulence intensity and relative integral length scale (Λ/d) from 2.5% to 6.3% and from 0.04 to 3.3, respectively at each studied Reynolds number. To ease the experiment process, the sphere was fixed while the location of the orificed perforated plate was varied in Experiment II. Our 'smooth flow' ($Tu < 0.3\%$) results agree with the standard C_D versus Re results in the literature. Over the range of conditions studied, current results have confirmed that the drag always decreases with increasing Tu and the critical Reynolds number at which the drag coefficient is dramatically reduced is advanced with increasing Tu. It is found that the effectiveness of Tu in reducing C_D is optimized when Λ is about 0.65d.

ACKNOWLEDGEMENTS

The author would like to express her sincere gratitude to Dr. David Ting and Dr. Shaohong Cheng for their excellent guidance and support during this study. The invaluable comments and assistance from the committee members are gratefully acknowledged. Technical assistance from the staff of the University of Windsor Technical Support Centre is appreciated. Gratitude goes especially to Mr. Andy Jenner who made all the spheres needed for this experiment and Mr. Marc St. Pierre.

The financial support from the Natural Sciences and Engineering Research Council of Canada in the form of Research Assistantship and an Equipment Grant are gratefully acknowledged. The financial support from the Department of Mechanical, Automotive and Materials Engineering in the form of a Graduate Assistantship is acknowledged. Thanks also go to the Faculty of Graduate Studies and Research of the University of Windsor for awarding the author the University of Windsor Tuition Scholarship.

TABLE OF CONTENTS

DECLARATION OF PREVIOUS PUBLICATION..... Iii

ABSTRACT..... iv

ACKNOWLEDGEMENTS..... v

LIST OF TABLES..... ix

LIST OF FIGURES..... x

NOMENCLATURE..... xiv

CHAPTER 1: INTRODUCTION..... 1

1.1 Objectives..... 1

1.2 Scope of Study..... 2

3

CHAPTER 2: LITERATURE REVIEW.....

2.1 Flow past a sphere 3

2.2 Freestream turbulence and its effect on drag force of a sphere 7

2.3 Effect of blockage on drag force of a sphere 15

2.4 Effect of surface roughness on drag force of a sphere..... 16

CHAPTER 3: EXPERIMENTAL DETAILS..... 18

3.1 Wind tunnel setup 18

3.2 Characteristics of the turbulent flow measurement in wind tunnel... 19

3.2.1 Measurement velocity 20

3.2.2 Calibration of hot-wire probes 21

3.2.3 Hot-wire data analysis 23

3.3 Sphere setup..... 26

3.3.1 PVC spheres..... 26
3.3.2 Wooden spheres..... 27
3.4 Drag measurement 28
3.4.1 Load cell specifications..... 28
3.4.2 Load cell setup 28
3.4.3 Load cell adjustment 31

CHAPTER 4: RESULTS AND DISCUSSION..... 32
4.1 Characteristics of flow downstream of the oerificed perforated plates..... 33
4.1.1 Root mean square velocity and relative turbulence intensity... 33
4.1.2 Integral length scale..... 37
4.2 Drag Results..... 39
4.2.1 Blockage effect on drag coefficient 39
4.2.2 Drag of sphere under "smooth flow" condition (Tu < 0.3%).... 40
4.2.3 Effect of turbulence intensity..... 43
4.2.4 Effect of relative integral length scale 46
4.2.5 Effect of integral length scale 50
4.2.6 Effect of Reynolds number..... 52

CHAPTER 5: CONCLUSION AND RECOMMENDATIONS..... 54
5.1 Conclusions..... 54
5.2 Recommendations for future works..... 54

REFERENCES..... 55

APPENDIX A: SELECTING SAMPLING FREQUENCY AND NUMBER 64

APPENDIX B: ANALYSIS OF HOT-WIRE DATA..... 72
APPENDIX C: MATLAB PROGRAM..... 82

APPENDIX D: SPHERE SETUPS..... 91

APPENDIX E: UNCERTAINTY ANALYSIS..... 92

APPENDIX F: X-PROBE RESULTS..... 102

APPENDIX G: DETAILS OF SPHERE SIZE IN RESULTS..... 107

APPENDIX H: FREE BODY DIAGRAM OF THE SPHERE..... 113

VITA AUCTORIS..... 116

LIST OF PUBLICATIONS..... 117

LIST OF TABLES

Table D.1	Springs angle in PVC sphere setup	91
Table D.2	String angle in wooden sphere setup	91

LIST OF FIGURES

Figure 1	Drag coefficient of the sphere as a function of Reynolds number [Torobin & Gauvin, 1959]	4
Figure 2	Schematic of flow past a sphere at (a) Re $\lesssim$ 0.1 (b) 0.1 $\lesssim$Re $\lesssim$ 24, (c) 24 $\lesssim$Re$\lesssim$ 270, (d) 270 $\lesssim$Re$\lesssim$ 10^3, (e) $10^3 \lesssim$Re$\lesssim$ 3 $\times 10^5$ and (f) Re $\gtrsim$ 3 $\times$ 10^5	7
Figure 3	Effect of turbulence on sphere drag [Torobin & Gauvin, 1960; Clamen & Gauvin, 1969]	10
Figure 4	Effect of relative turbulence intensity on the drag coefficient of spheres [Uhlherr & Sinclair, 1970]	11
Figure 5	Correlations for the effect of turbulence on drag [Clift & Gauvin, 1971]	12
Figure 6	Critical Reynolds number of spheres as a function of the relative intensity of turbulence, [Clift & Gauvin, 1970]	13
Figure 7	Effect of sphere diameter on drag coefficient [Zarin & Nicholls, 1971]	15
Figure 8	Blockage effect on the drag coefficient of a sphere in Phoreman et al.'s results [2007]	16
Figure 9	Variation of the drag coefficient owing to active and passive controls as of the Reynolds number: • Jeon et al. [2004]; ··· dimples (golf ball) by Bearman and Harvey [1976]; ---, roughness (k/d) by Achenbach [1974*b*]; ——, Choi et al. [2006]	17
Figure 10	Closed-loop wind tunnel used for the experiment	18
Figure 11	Schematic of the orificed perforated plates (a) Plate D-25, (b) Plate D-37.5, and (c) Plate D-50	19
Figure 12	The orificed perforated plate	19
Figure 13	Hot-wire system	20
Figure 14	Old hot-wire calibration system	22
Figure 15	Dantec Model streamline 90H02 hot-wire calibration system	23
Figure 16	Schematic of flow velocity and hot-wire	25
Figure 17	Schematic of threaded hole in a sphere	27

Figure 18	Schematic of experiment layout	28
Figure 19	Load cell	29
Figure 20	Schematic of the load cell setup with the sphere supported by strings	30
Figure 21	Geometric condition strings	30
Figure 22	Load cell adjustment setup	31
Figure 23	Variation of rms velocity (m/s) with respect to (x/D) in 1D hot-wire measurement: (a) with perforated plate D-25 (b) with perforated plate D-37.5 and (c) with perforated plate D-50	35
Figure 24	Variation of relative turbulence intensity with respect to (x/D) in 1D hot-wire measurement: (a) with perforated plate D-25 (b) with perforated plate D-37.5 and (c) with perforated plate D-50	36
Figure 25	Variation of integral length scale with respect to (x/D) in 1D hot-wire measurement: (a) with perforated plate D-25 (b) with perforated plate D-37.5 and (c) with perforated plate D-50	38
Figure 26	Blockage effect on the drag coefficient of PVC spheres in "smooth flow"	40
Figure 27	Blockage effect on the drag coefficient of wooden spheres in "smooth flow"	40
Figure 28	Drag coefficient versus Reynolds number in the absence of orificed perforated plate in comparison with other standard curves, (Curve (1): Schlichting [1979] and Lee [1987], Curve (2): Lapple and Shepherd, [1940] and Clift and Gauvin [1970 & 1971], Curve (3): Achenbach [1972])	41
Figure 29	Drag coefficient versus Reynolds number in the absence of orificed perforated plate in comparison with Standard band	42
Figure 30	Impact of turbulence intensity on PVC sphere drag	44
Figure 31	Impact of turbulence intensity on wooden sphere drag	45
Figure 32	Impact of relative integral length scale on PVC sphere drag when (a) Tu = 2.5% (b) Tu = 4% (c) Tu = 6.3%	47

Figure 33	Impact of relative integral length scale on wooden sphere drag when (a) Tu = 2.5% (b) Tu = 4% (c) Tu = 6.3%	49
Figure 34	Impact of integral length scale on PVC sphere drag when (a) Tu = 2.5% (b) Tu = 4% (c) Tu = 6.3%	51
Figure 35	Impact of Reynolds number on PVC sphere drag	52
Figure 36	Impact of Reynolds number on wooden sphere drag	53
Figure A.1	Minimum required sampling number for $\overline{U}$ at U ≈ 12 m/s, f_s = 80 kHz (1D Probe)	65
Figure A.2	Minimum required sampling number for u at U ≈ 12 m/s, f_s = 80 kHz (1D Probe)	66
Figure A.3	Minimum required sampling number for Λ at U ≈ 12 m/s, f_s = 80 kHz (1D Probr)	67
Figure A.4	Minimum required sampling number for $\overline{U}$ at U ≈ 12.1 m/s, f_s = 80 kHz (X-Probe)	68
Figure A.5	Minimum required sampling number for u at U ≈ 12.1 m/s, f_s = 80 kHz (X-Probe)	69
Figure A.6	Minimum required sampling number for Λ at U ≈ 12.1 m/s, f_s = 80 kHz (X-Probe)	70
Figure B.1	Schematic of flow velocity and hot-wire	73
Figure E.1	The roughness of PVC spheres	100
Figure E.2	The roughness of wooden spheres	100
Figure F.1	Variation of rms velocity (m/s) in x direction with respect to (x/D) in 2D hot-wire measurement: (a) with perforated plate D-25 (b) with perforated plate D-37.5 and (c) with perforated plate D-50	103
Figure F.2	Variation of relative turbulence intensity with respect to (x/D) in 2D hot-wire measurement: (a) with perforated plate D-25 (b) with perforated plate D-37.5 and (c) with perforated plate D-50	104
Figure F.3	Variation of integral length scale with respect to (x/D) in 2D hot-wire measurement: (a) with perforated plate D-25 (b) with perforated plate D-37.5 and (c) with perforated plate D-50	105

Figure F.4	Variation of rms velocity (m/s) in y direction with respect to (x/D) in 2D hot-wire measurement: (a) with perforated plate D-25 (b) with perforated plate D-37.5 and (c) with perforated plate D-50	106
Figure G.1	Impact of integral length scale on PVC sphere drag when (a) Tu = 2.5% (b) Tu = 4% (c) Tu = 6.3%	107
Figure G.2	Impact of relative integral length scale on PVC sphere drag when (a) Tu = 2.5% (b) Tu = 4% (c) Tu = 6.3%	108
Figure G.3	Impact of turbulence intensity on PVC sphere drag	109
Figure G.4	Impact of Reynolds number on PVC sphere drag	109
Figure G.5	Impact of relative integral length scale on wooden sphere drag when (a) Tu = 2.5% (b) Tu = 4% (c) Tu = 6.3%	110
Figure G.6	Impact of turbulence intensity on wooden sphere drag	111
Figure G.7	Impact of Reynolds number on wooden sphere drag	112
Figure H.1	Schematic of net forces of the strings in the sphere and load cell setup	113
Figure H.2	Geometric condition of the top strings	114

NOMENCLATURE

A	sphere cross-sectional area, $A = \frac{\pi d^2}{4}$ [m]^2
B	Blockage ratio
C_0, C_1, C_2, C_3, C_4	hot-wire calibration coefficients
C_{01}, C_{11}, C_{21}, C_{31}, C_{41}	hot-wire calibration coefficients
C_{02}, C_{12}, C_{22}, C_{32}, C_{42}	hot-wire calibration coefficients
C_D	drag coefficient
D	diameter of holes of the orifice perforated plates [m]
d	diameter of spheres [m]
E_c	voltage data [mV] of 1D probe
E_{1c}, E_{2c}	voltage data [mV] of 1D probe
F_{bottom}	tensile force in a bottom string [N]
F_{D_Bottom}	streamwise tensile component in a bottom string [N]
F_D	drag force [N]
F_{D_Top}	streamwise tensile component in a top string [N]
F_{top}	tensile force in a top string [N]
f_s	sampling frequency, f_s = 80 kHz
L	Eulerian scale of turbulence
N	sampling number
Re	Reynolds number, Ud/ν
Re_{cr}	critical Reynolds number
rms	root mean square
Tu	turbulence intensity $u_{rms}/\overline{U}$ (%)
U	mean flow velocity [m/s]
$\overline{U}$	time averaged velocity [m/s]
U_{eff}	effective velocity in x component [m/s]
U_i	instantaneous velocity [m/s]

u	instantaneous fluctuating velocity [m/s]
u_{rms}	root mean square velocity [m/s]
V_{eff}	effective velocity in y component [m/s]

Greek Symbols

$\alpha, \alpha', \beta, \beta'$	geometrical angle of sphere setup
Λ	integral length scale [m]
ν	kinetic viscosity [m^2/s]
ρ	density [kg/m^3]
ς	autocorrelation factor
τ	time [s]
τ_Λ	integral time scale [s]

Latin and other Symbols

$\Delta(\cdot)$	relative uncertainty of $(\cdot)$
$\overline{(\cdot)}$	time-average of $(\cdot)$
Δt	time interval between consecutive samples [s]

CHAPTER 1: INTRODUCTION

Sphere as a three dimensional bluff body in turbulent freestream is a common phenomenon in our everyday life. In many engineering problems such as the flight of a weather balloon, the dispersion of aerosols sprays, rocket system, and the course of pollutants in the air and water, knowledge of parameters such as aerodynamic forces of spherical bodies in the presence of turbulent flow is often required. Sphere aerodynamics is also very important in sports such as golf, baseball and tennis.

There have been several studies on the characteristics of flow over a sphere [Fage, 1937; Achenbach, 1972; Achenbach, 1974*a*; Taneda, 1978; Kim & Durbin, 1988; Sakamoto & Haniu, 1990; Mittal, 1999; Kim & Choi, 2002; Yun et al., 2003]. The main characteristic of flow around a sphere is the existence of turbulent wake with recirculation [Chomaz et al., 1993; Tyagi et al., 2006], which has a dominant effect on the drag and lift of the sphere. The extent of this region depends on the size of the body, the velocity and viscosity of the fluid, which are cumulatively expressed as the Reynolds number. Moreover, it may be strongly influenced by a wide variety of flow disturbances, which may originate from different sources.

1.1 OBJECTIVES

Due to its importance, a sphere in a flow has been studied extensively, over the last few decades. In spite of the effort, there remains many discrepancies on the effect of turbulence on the aerodynamics of a sphere. These may be caused by the multi-aspect of turbulence, i.e. the dependency of one turbulent parameter on another. There appears to be a lack of systematic studies aiming at uncovering the underlying independent roles of these turbulent parameters on the drag C_D.

Therefore, the focus of this thesis is to study the effect of freestream turbulence on the drag of a sphere. The objective is to separate the influences of 1) integral length scale Λ and/or relative integral length scale Λ/d (where d is the sphere diameter); 2) turbulence intensity Tu; and 3) freestream Reynolds number Re on the drag coefficient of a solid sphere exposed to freestream turbulence. Also, in "smooth flow", the effect of blockage ratio on the drag coefficient of a sphere is examined.

1.2 SCOPE OF STUDY

In this study, the effects of Tu, Λ and Λ/d of freestream turbulent flow generated downstream of orificed perforated plates on C_D were investigated experimentally at different Reynolds number in a closed-loop wind tunnel. This consideration was done in two different experimental setups, Experiments I and II with PVC and wooden spheres, respectively. In order to measure the turbulence parameters, a single normal hot-wire of DISA type 55P11 and X-type hot-wire probe of Dantec type 55P61 were used in Experiments I and II, respectively. And, model ELG-V-1N-L03M ENTRAN load cell was utilized in the drag force measurements.

Within the limitations of our experimental facility, the Reynolds number based on freestream velocity and sphere diameter was varied from 2.2×10^4 to 8×10^4. The freestream turbulent flow generated by the available orificed perforated plates provided a range of turbulence intensity from 1.9% to 10% and relative integral length scale Λ/d from 0.04 to 3.25.

CHAPTER 2: LITERATURE REVIEW

2.1 FLOW PAST A SPHERE

For a single, smooth sphere in steady, isothermal, non-turbulent, incompressible flow, the drag coefficient, which has been quantified in many experimental studies, is well known. Under the above conditions, drag has been found to be a function of Reynolds number alone. The plot of the sphere drag coefficient versus Reynolds number variation is called the "standard drag curve" as shown in Figure 1.

This Section describes the variation of flow characteristics around a sphere with increasing Reynolds number.

(i) $Re \lesssim 24$:

For $Re \lesssim 0.1$, the flow near the sphere is essentially symmetrical as shown in Figure 2(a) [Lamb, 1945]. For $0.1 \lesssim Re \lesssim 24$, inertial effects increase in importance near the sphere and the streamline pattern is no longer symmetrical [Jenson, 1959], as shown in Figure 2(b). It can be seen from the standard logarithmic C_D-Re curve in Figure 1 [Torobin & Gauvin, 1959] that in this range of very low Reynolds number, the drag coefficient of a sphere is given by Stokes' Law,

$$C_D = \frac{24}{Re} \tag{1}$$

The curve shows a linear trend and the drag coefficient of a sphere decreases logarithmically with increasing Reynolds number.

(ii) $24 \lesssim Re \lesssim 270$:

At $Re \approx 24$, Taneda [1956] reported the appearance of a small closed region of separated flow downstream of the rear stagnation point and Baki et al. [2006] mentioned that it results in the generation of axis symmetric rings. Differences in freestream turbulence and the method used for flow visualization can cause some variation in the Reynolds number where flow separation is first observed. As the Reynolds number increases, a vortex recirculation grows within the separation bubble and its stability decreases; see Figure 2(c).

At Re ≈ 130, the downstream part of the separated region begins to oscillate [Taneda, 1956]. This oscillation becomes stronger as Re increases up to about 210, but the laminar wake downstream of the wake stagnation point remains stable. For $210 \lesssim Re \lesssim 270$, an asymmetrical separation bubble with a laminar wake has been observed [Magarvey & Maclatchy, 1964]. Lemmin et al. [1985] shows that for $Re \cong 100$, the sphere drag coefficient C_D varies as a function $U^{-1/2}$, where U is the mean flow velocity.

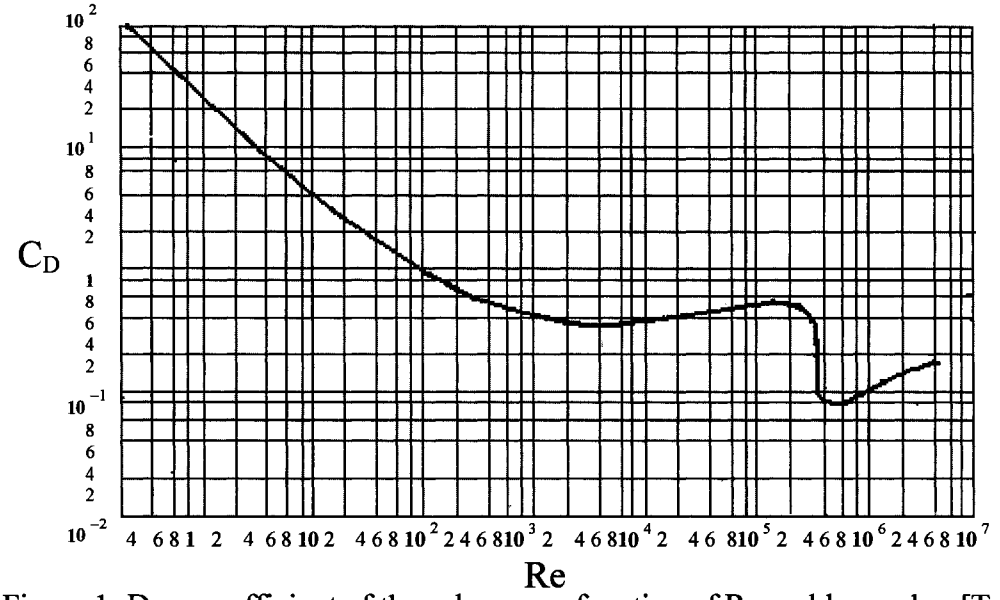

Figure 1: Drag coefficient of the sphere as a function of Reynolds number [Torobin & Gauvin, 1959]

(iii) $270 \lesssim Re \lesssim 1000$

Discrete vortex loops are shed periodically for $290 \lesssim Re \lesssim 700$, [Sivier & Nicholls, 1969]. Sivier and Nicholls [1969] noted that an increase in the level of freestream turbulence can cause the occurrence of vortex shedding at Re as low as 150. When the Reynolds number is further increased to around 800, the vortex loops diffuse very rapidly, and the wake flow becomes turbulent. The resultant shape of the vortex structure in the wake of the sphere is shown in Figure 2(d). As may be inferred from the figure, horse-shoe shaped vortex loops are formed [Magarvey & Maclatchy, 1964; Achenbach, 1974*a*; Ormieres & Provansal, 1999]. These loops are rapidly

detached from the near-wake region and form a series of vortices that are shed periodically into the far wake. As shown in Figure 1, the logarithmic C_D-Re curve is roughly linear in this range, too. But, for Re≳700, the logarithmic scale trend of C_D-Re curve is no longer linear. The relationship in this range can be described as [Bakic & Peric, 2005]:

$$C_D = \frac{24}{Re}\left(1+\frac{Re^{2/3}}{6}\right)^2 \qquad (2)$$

Lemmin et al. [1985] have shown that the drag coefficient drops from about 1 at Re ≈ 100 to 0.5 at Re ≈ 500, and to 0.44 at Re ≈ 1,000.

(iv) $10^3 \lesssim Re \lesssim 3\times10^5$:

In this range, the vortex loop shedding becomes nearly a continuous process. Fluctuation corresponding to the shedding of vorticity still occurs [Lamb, 1945]. Visualization experiments [Bakic & Peric, 2005] have shown that the far wake region continues to grow in size and produces a wave-like motion. The near wake structure in this flow regime is depicted in Figure 2(e). Willmarth and Enlow [1969], Achenbach [1974*a*], and Taneda [1978] have suggested that the circulation is caused by the asymmetric shedding of large turbulent eddies into the wake, which produces an unsteady bound vorticity vector whose cross-product with the mean stream velocity determines the fluctuating force. It is responsible, for example, for the erratic path of a rising weather balloon [Scoggins, 1967] and for the unpredictable trajectory of a baseball thrown at medium speed with very little spin (a `knuckle ball') or of a cricket ball whose seam is at zero angle of incidence to its direction of motion [Barton 1982]. But as found out by Howe et al. [2001], most effects are on lift force and the effects on drag force are negligible. Figure 1 shows that the value of C_D virtually remains constant in this regime. Lemmin et al. [1985] found that when Re≳2000, C_D reaches a value of 0.39 and for 2,000≲Re≲10,000, the drag coefficient varies with U^2.

(v) $Re \gtrsim 3 \times 10^5$:

Around $Re \approx 3 \times 10^5$, transition to turbulence occurs in the boundary layer, leading to increased momentum near the boundary resulting in a delayed separation, Figure 2(f), corresponding to a smaller wake and lower drag, referred to as drag crisis [Schlichting, 1955]. It has been observed in previous studies [Achenbach, 1972, Taneda, 1978] and also can be seen in Figure 1 that as the flow undergoes transition from subcritical to supercritical flow, the drag coefficient shows a rapid drop. The minimum value of drag coefficient is reached at the critical Reynolds number, Re_{cr}. With further increase of Reynolds number, C_D slowly increases again. In the supercritical regime, time histories of the forces and frequency spectra of the drag show that the supercritical solutions are chaotic and unsteady [Constantinescu & Squires, 2004].

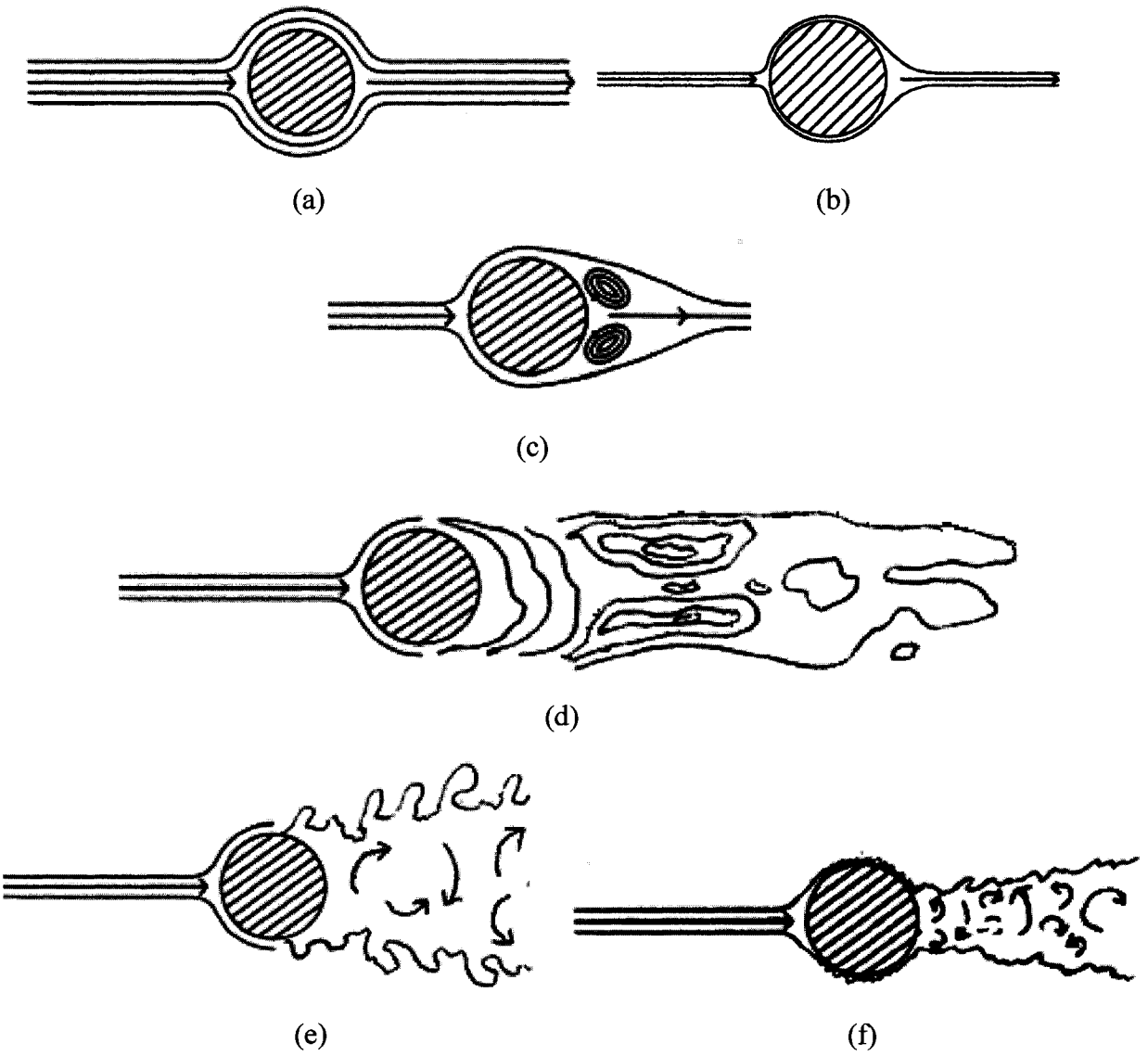

Figure 2: Schematic of flow past a sphere at (a) $Re \lesssim 0.1$ (b) $0.1 \lesssim Re \lesssim 24$, (c) $24 \lesssim Re \lesssim 270$, (d) $270 \lesssim Re \lesssim 10^3$, (e) $10^3 \lesssim Re \lesssim 3 \times 10^5$ and (f) $Re \gtrsim 3 \times 10^5$

2.2 FREESTREAM TURBULENCE AND ITS EFFECT ON DRAG FORCE OF A SPHERE

Since most applications of sphere-fluid interaction occuring in practice involve turbulence freestream, in order to advance our understanding of the aerodynamics of a sphere, it is imperative to have a proper knowledge of the role of freestream turbulence. A priori to understanding the aerodynamics of a sphere in complex turbulent flow encountered in engineering practice is a good comprehension of smooth sphere

aerodynamics in simple turbulent freestream. The flow downstream of an orificed perforated plate provides such a clean, simple, and quasi-isotropic freestream turbulence [Liu & Ting, 2007].

As mentioned earlier, the C_D-Re behavior for the 'smooth flow' situation is well known. Freestream turbulence may strongly influence this C_D-Re behavior. Many wind tunnel studies, [Ahlborn, 1931; Anderson, 1975; Bearman, 1971; Becker & Brown, 1974; Brownlee, 1960; Anderson & Uhlherr, 1977] have found that increasing fluid turbulence reduces the value of critical Reynolds number Re_{cr} for boundary layer flow transition, to occur. Below the critical Reynolds number, it has been observed that flow turbulence can cause a moderate increase in the drag coefficient as compared to that found in the smooth flow [Zarin, 1970]. Near the standard (smooth flow) critical Reynolds number, by perturbing the flow, the separation point shifts downstream along the sphere surface affecting the vorticity transfer and dissipation in the wake and, hence, the form drag [Kendall, 1964; Winny, 1932].

In some experimental studies, researchers used the C_D-Re curve to indicate when flow status changes to turbulent. This method to find the critical Reynolds number, was originally proposed by Prandtl [1914]. At low Reynolds numbers, C_D is approximately constant and equals to about 0.5. At critical Reynolds number which value depends on the turbulence of the air stream, C_D decreases rapidly to values in the neighborhood of 0.1. This drop shows that the flow completely changes to a turbulent one and the different values of critical Reynolds number are associated with different turbulence levels. Prandtl [1914] suggested that observation of such resistance curves for spheres gave a means of comparing the air streams of different systems of laboratories, with respect to their lesser or greater turbulence. The decrease of C_D occurs at higher Reynolds numbers, around Re $\approx 10^3$ in streams of lower turbulence. Also, Balachandar et al. [2004] explained this phenomenon. The mean wake in a turbulent flow shows reduced velocity deficit and a flatter profile than wake in laminar flow. However, the mean wake in a turbulent flow behaves like a self–preserving laminar wake. At low Reynolds numbers, the wake in a turbulent flow oscillates strongly without any vortex shedding, but at higher Reynolds numbers, vortex shedding starts. The nature of the vortices is very different from that in a uniform flow which causes reduction in C_D. Increasing the freestream turbulence intensity

suppresses the process of vortex shedding, and only marginally increases the wake oscillation.

By using stationary spheres in a wind tunnel of known turbulence characteristics, Dryden et al. [1937] have found that for flow over a sphere, the turbulent parameter that affects Re_{cr} the most is turbulence intensity. The critical Reynolds number Re_{cr} decreases monotonically with the increase of turbulence intensity up to 4.5%. Their data correlates more closely when Re_{cr} is plotted against $[(u/U)(d/L)^{1/2}]$, where u is the instantaneous fluctuating velocity, U is the mean flow speed, d is the sphere diameter, and L is the Eulerian scale of turbulence. This parameter is derived by Taylor [1937] who suggested that the fluctuating pressure gradients which accompany freestream turbulence were responsible for transition to turbulence.

Torobin and Gauvin [1960 & 1961] and subsequently Clamen and Gauvin [1969] used a grid system to generate turbulence in a wind tunnel and injected spherical particles of different size into the wind tunnel. The particles were injected upstream at velocities close to that of the oncoming air stream. Their results are shown in Figure 3. The drag coefficient, after its sharp drop due to transition, rises steeply to a maximum and then dropped off again gradually. The C_D-Re curves corresponding to different turbulence intensity levels have similar shapes but the maximum C_D occurs at different Reynolds numbers. The maximum C_D increases with the increase of turbulence intensity, while the Reynolds numbers at which the maximum C_D occurs decreases with the increasing intensity; see Figure 3. After reaching their maximum, the C_D-Re curves corresponding to different turbulence levels tend to converge at higher Reynolds number. Clamen and Gauvin [1969] suggested that the increase of the maximum values of C_D with the turbulence intensity observed in the supercritical flow regime might be associated with the increased vorticity in the wake due to the presence of freestream turbulence. The vorticity reduces the extent of the near wake by hastening the spatial return to freestream conditions behind the sphere. With the shortening of the near wake, the main flow is required to close more sharply behind the sphere. A greater lateral pressure gradient is then needed to produce the increased curvature of the streamlines. Since the ambient free-stream pressure is fixed, there must be a decrease in the pressure at the rear of the sphere (particle) and, hence, an increased drag. Also, the similarity of the C_D-Re curves in Figure

3 at different turbulence levels indicates the lack of dependence of turbulent skin friction on turbulence intensity. They saw a large decrease in C_D from 1.5 to 0.5 with the change in Reynolds number but very small decrease in the skin friction. It is worth mentioning that Λ/d varied from 2 to 6.25 within the Reynolds number range of 500 to 2100 in Torobin and Gauvin's [1961] experiments. However, they did not examine the role of Λ/d closely. In Torobin and Gauvin's [1960] and Clamen and Gauvin's [1969] researches, the only turbulent parameter considered was turbulence intensity. There was no mention of Λ/d, even though it was varied presumably over a significant extent.

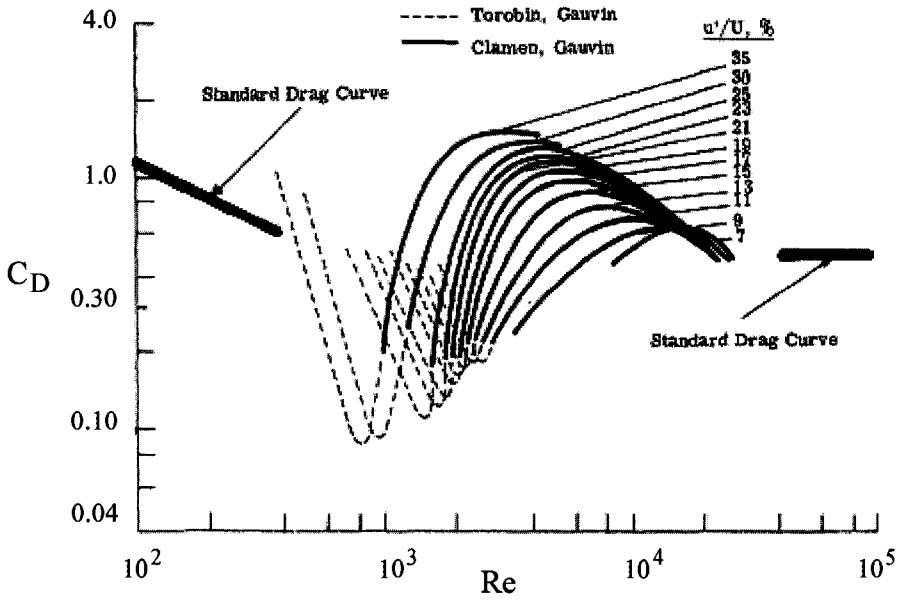

Figure 3: Effect of turbulence on drag of freely moving multiple spheres [Torobin & Gauvin, 1960; Clamen & Gauvin, 1969]

The effect of turbulence on drag below the critical range of Reynolds number was investigated by Sivier and Nicholls [1969], Uhlherr and Sinclair [1970] and Anderson and Uhlherr [1977] by using freely moving sphere in experiments. For example, Uhlherr and Sinclair [1970] and Anderson and Uhlherr [1977] used spheres and spherical particles entrained in turbulent liquid system.

In the subcritical range of Reynolds numbers, Sivier and Nicholls [1969] reported that moderate freestream turbulence intensities (Tu $\leq$ 8%) produce a definite increase in

C_D for Re > 200. The increase is growing with increasing Re. Compared to the C_D's measured at lower turbulence intensities (Tu ~ 1%), at Re < 200, they have observed little or no change in C_D. Their measurements did not include the scale or spectra of the turbulence and turbulence intensity was not varied over a very wide range.

Uhlherr and Sinclair [1970] found that, at low levels of turbulence, Tu ≤ 0.05, the effect of length scale on drag can be correlated with the one-fifth power of scale and at high levels of turbulence, a scale effect on drag to be completely absent. Also, they found higher turbulence intensity causes higher drag coefficient in Re < 1000; see Figure 4(a) and (b). As shown in Figure 5, Uhlherr and Sinclair [1970] showed that the drag coefficient for a given Reynolds number and low turbulence intensity first decreases below the zero-turbulence drag curve, and then by increasing turbulence intensity, increases again. Although there is little duplication between the results of Torobin and Gauvin [1960] and those reported here, the two sets of data are contiguous in significant effects of Tu on C_D.

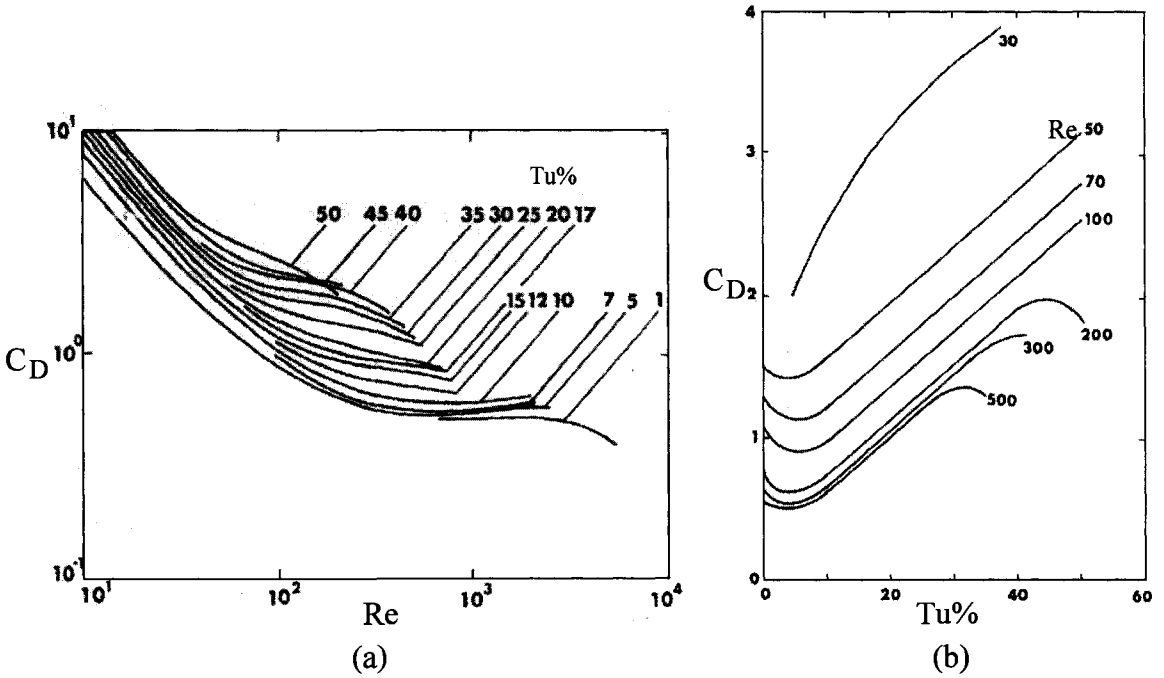

Figure 4: Effect of relative turbulence intensity on the drag coefficient of freely moving multiple spheres [Uhlherr & Sinclair, 1970]

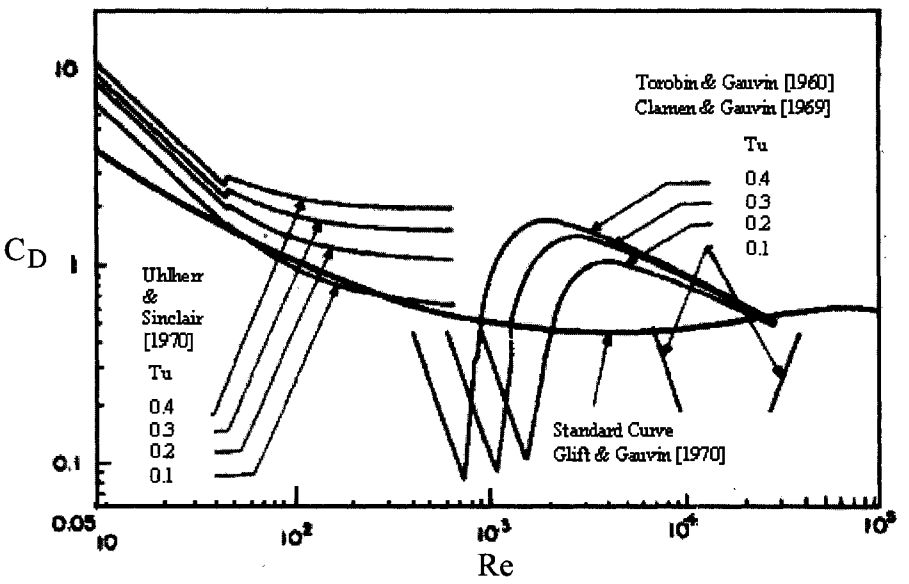

Figure 5: Correlations for the effect of turbulence on drag of freely moving multiple spheres [Clift & Gauvin, 1971]

In low Reynolds number (Re < 100) and Reynolds number less than the critical one, for particles convected upward in a pipe with turbulent flow, Anderson and Uhlherr [1977] showed that the effects of turbulence were not as large as those which were found previously.

Also, the effect of turbulence on drag below the critical range of Reynolds number has been considered by Zarin [1970] and Zarin and Nicholls [1971]. They used the experimental setup with fixed sphere. For example, Zarin [1970] used metal spheres held in a turbulent gas stream by a magnetic suspension system. Generally, their results concurred with previous ones using either fixed or freely moving spheres which shows increasing turbulence intensity decreases the critical Reynolds number, such as Dryden et al. [1937] and Torobin and Gauvin [1960]. It looks like the results of moving spheres show more significant effect of Tu on the critical Reynolds number.

For low Reynolds number, 200 < Re < 800, Zarin and Nicholls [1971] and Zarin [1970] showed that turbulence levels of 0.4% to 3.3% produced significant drag increases. The scale of the turbulence which is obtained by this method is of the order of, or greater than the diameter of the spheres tested. The percentage of drag rise due to turbulence decreases with decreasing Re. The increase of C_D approaches zero for Re $\leq$ 100 and Tu $\leq$ 3%. One reason for the decreasing influence of turbulence with decreasing

Re is the smaller and more stable separated region on which the turbulence can act. They also reported that C_D increased monotonically with inverse sphere diameter in $600 \leq Re \leq 5000$. In this series of experiments the integral scale was generally less than the sphere diameter ($0.16 \leq \Lambda/D \leq 1$).

At $5\times10^3 < Re < 10^5$ and $Tu < 25\%$, Neve [1986] and Neve and Shansonga [1989] discovered the effects of turbulence on the drag of solid spheres. A complex effect of turbulence intensity and spatial integral scale on drag coefficient of a sphere is reported [Neve & Shansonga, 1989]. Their experiment was done in an open wind tunnel (0.405 m $\times$ 0.240 m) with a fixed 37.7 mm sphere. They didn't get the same conclusion from their results for different Reynolds number. But, in particular, for special values of turbulence intensity and spatial integral scale, the drag coefficient of solid spheres is reduced to its value in Re_{cr}.

Petrak [1976], Lee [1987] and Warnica et al. [1995] reported that drag coefficients of particles in a turbulent field were much less than those in a quiescent field although the intensities of turbulence were quite low.

Clift and Gauvin [1970], like Dryden et al. [1937] and Torobin and Gauvin [1961], found that flow with higher turbulence intensity had smaller critical Reynolds number by numerical simulation of moving particle. They defined an equation to predict the value of critical Reynolds number in flow with different turbulence intensities from their result shown in Figure 6.

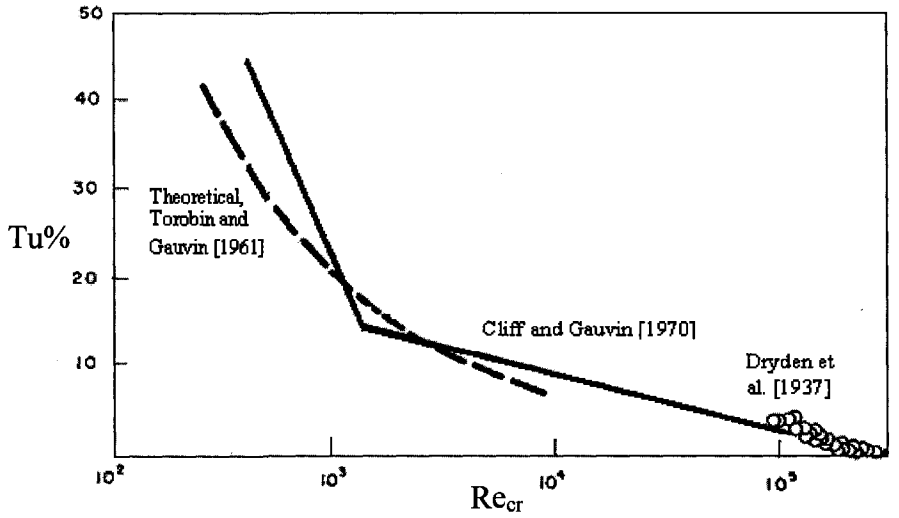

Figure 6: Critical Reynolds number of spheres as a function of the relative intensity of turbulence [Clift & Gauvin, 1970]

The measurements by Sankagiri and Ruff [1997] covered the sub-critical, critical, and super-critical Reynolds number region. In the sub-critical range, the drag with enhanced Tu is greater than the standard drag, and decreases gradually into the critical range. The behavior at the critical and super-critical Reynolds numbers agrees fairly well with previous data obtained by Clift and Gauvin [1971].

More recently, Bagchi and Balachandar [2003] and Birouk and Abou Al-Sood [2007] conducted a direct numerical simulation to determine the effect of turbulence on the drag of a particle for $10 < Re < 250$ and $0\% < Tu\% < 60\%$. Their results confirmed Warnica et al.'s [1995] suggestion. They believed the freestream turbulence intensity does not affect significantly the drag coefficient of a particle or sphere in this flow condition.

The drag of non-evaporating, spherical, deformable liquid droplets was measured in turbulent flow fields characterized by the droplet Reynolds number, and the intensity and spatial scales of turbulence by Warnica et al. [1995]. The range of Reynolds numbers investigated was 10-100, and that of the relative intensities of turbulence was 20-65 percent, in terms of the mean relative speed. The ratio between the spatial integral scale and the droplet diameter was in the range of 11-38. Experimental data showed that the drag in turbulent fields under these conditions was not significantly different from that of solid spheres in a quiescent field at the same Reynolds number and it was higher than the values for standard situation. In general, these relationships indicated that the drag coefficient increased with increasing relative intensity. The numerical study by Yusof [1996] also illustrated a drag increase of nearly 40% in a freestream turbulence intensity of 20% in Reynolds number less than 1000.

Brucato et al., [1998] did the experiment with novel technique. The technique is suitable for obtaining data with particles smaller than those needed by most of the other techniques such as direct numerical simulation, etc. This system with glass and silica particles in water, shows that particle drag in the $Re < 100$ and $Tu = 5\%$ is either unaffected or increased by freestream turbulence, depending on particle size and turbulence intensity. For the largest particle an increase of more than forty folds was observed. Lee [2000] yielded the similar conclusion from his results in $Tu = 20\%$ and $Re < 100$.

2.3 EFFECT OF BLOCKAGE ON DRAG FORCE OF A SPHERE

In wind tunnel tests, blockage ratio is defined as the ratio between the cross-sectional area of a sphere and that of the test section. It can have some effects on drag coefficient of a sphere in turbulent and smooth flow.

Zarin and Nicholls [1971] considered the blockage ratio effect on C_D in $600 \leq Re \leq 5000$ on a fixed sphere in wind tunnel with 2 in diameter. They found that C_D increases monotonically with inverse sphere diameter as shown in Figure 7. But, by using the numerical methods, Blackburn [2002] found that higher blockages contribute to the slightly higher values of C_D.

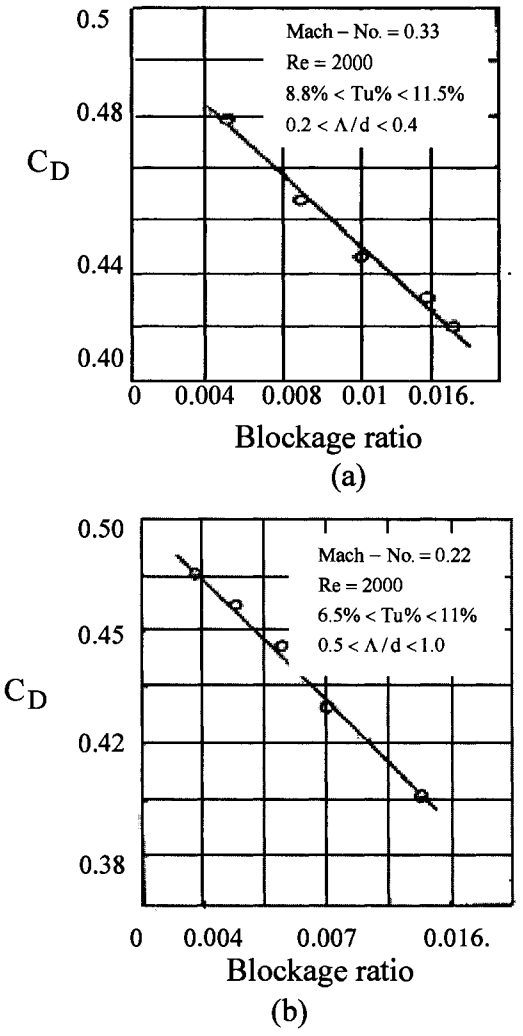

Figure 7: Effect of sphere diameter on drag coefficient [Zarin & Nicholls, 1971]

Sample data points from Phoreman et al. [2007] are given in Figure 8. Three spheres of diameters 87.5, 137.5 and 225 mm were tested at the UC Davis Aeronautical wind tunnel where the turbulence intensity is less than 0.1%. The test section was 840 mm high and 1200 mm wide. It was found that once the blockage ratio was beyond 0.02, for Reynolds number less than the critical value ($Re < Re_{cr} \approx 3\times10^5$), the drag coefficient of the sphere was increased, and for $Re \geq Re_{cr}$, the drag coefficient of the sphere was decreased; see Figure 8.

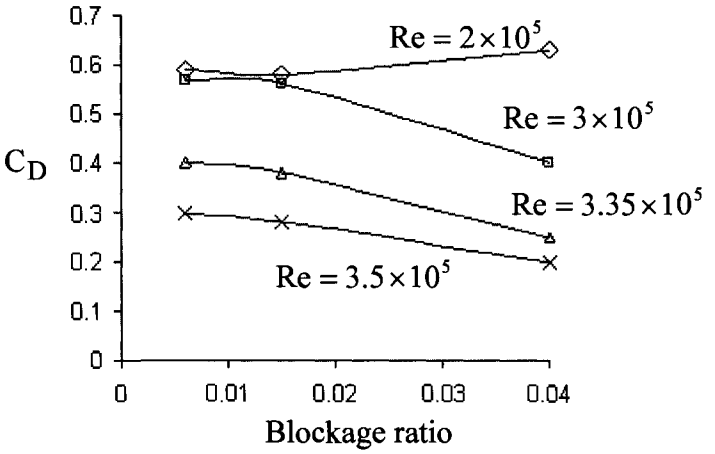

Figure 8: Blockage effect on the drag coefficient of a sphere in Phoreman et al.'s results [2007]

2.4 EFFECT OF SURFACE ROUGHNESS ON DRAG FORCE OF A SPHERE

Perturbing the boundary layer via surface roughness is one method to make turbulent flow. This technique is used for body shapes such as sphere and for applications wider than just in aeronautics.

White [1966] found that roughening the sphere surface shifted the wake separation point downstream, reducing drag. Also, wind tunnel measurements for spheres [Achenbach, 1974*b*; Lyotard et al., 2007] indicated that the drag crisis was shifted to lower Re when the surface is roughened. Golf balls are made with surface dimples in order to reduce drag by a very similar mechanism [Choi et al., 2006]. Dimples cause local flow separation and trigger the shear layer instability along the separating shear layer, resulting in the generation of large turbulence intensity. With this increased turbulence,

the flow reattaches to the sphere surface with a high momentum near the wall and overcomes a strong adverse pressure gradient formed in the rear sphere surface. As a result, dimples delay the main separation and reduce drag significantly.

Figure 9 shows the results by different researchers regarding the effect of surface roughness on C_D-Re relation of a sphere which are fixed or moving in experimental wind tunnel. It can be clearly seen that drag coefficient was decreased and critical Reynolds number was increased by decreasing surface roughness. Also, at Re > Re_{cr}, the drag coefficient increases more drastically at larger roughness and approaches 0.4.

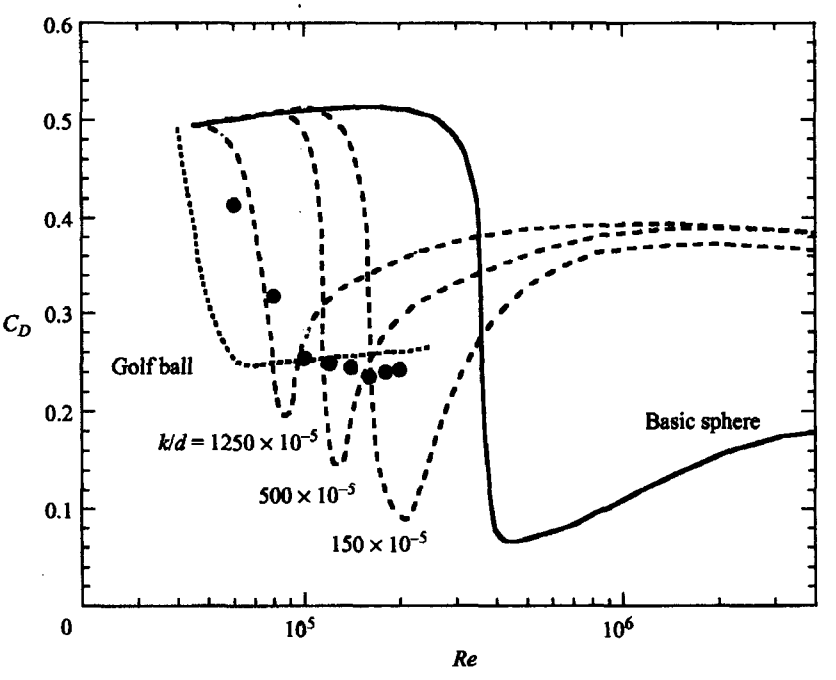

Figure 9: Variation of the drag coefficient owing to active and passive controls as of the Reynolds number: • Jeon et al. [2004]; ··· dimples (golf ball) by Bearman and Harvey [1976]; ---, roughness (k/d) by Achenbach [1974*b*]; ——, Choi et al. [2006]

CHAPTER 3: EXPERIMENTAL DETAILS

3.1 WIND TUNNEL SETUP

The experiments were conducted in a closed-loop wind tunnel with a 4 m long test section. The test section is 0.75 m (width) × 0.75 m (height) at the inlet. To accommodate for boundary layer built up, it expands to 0.765 m × 0.765 m at the end. Figure 10 shows the overall view of the wind tunnel. The maximum attainable freestream velocity is around 20m/s and the background turbulence level is less than 0.3%.

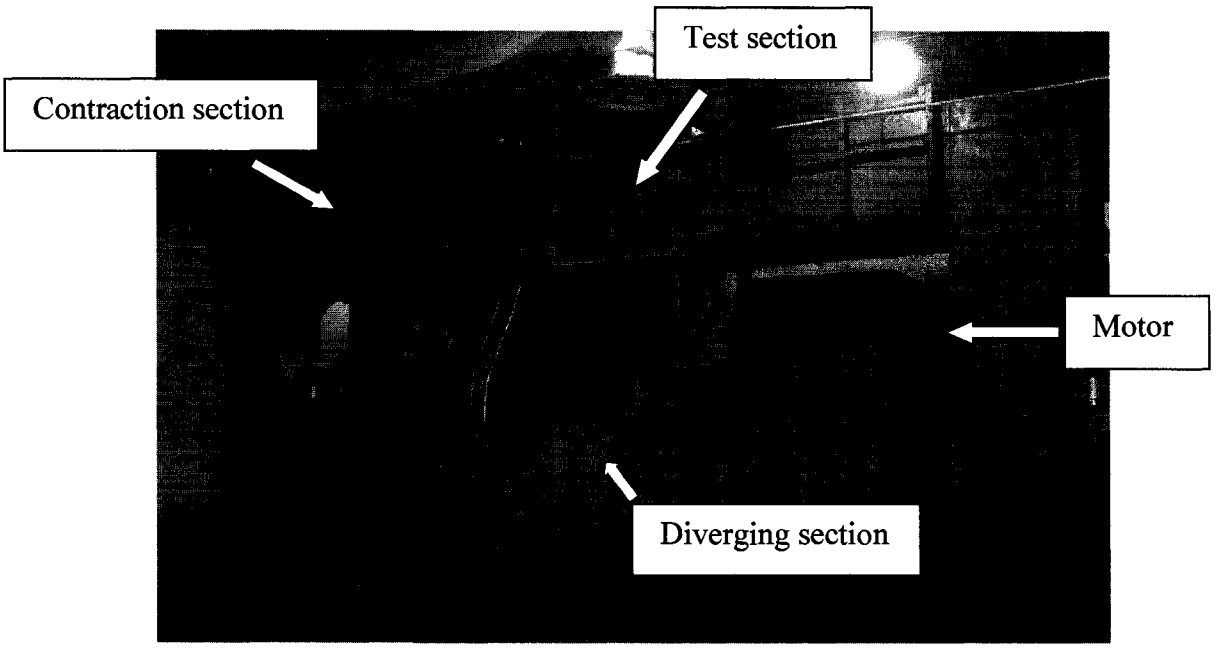

Figure 10: Closed-loop wind tunnel used for the experiment

The turbulence was generated by placing one of the three orificed perforated plates in the wind tunnel. These are 6 mm thick aluminum plates with hole diameter D of 25, 37.5, and 50 mm, respectively, as shown in Figure 11. The solidity ratio of the plate was fixed at 43%. To minimize the influence of the plate thickness on the turbulent flow field generated, each hole was machined into an orifice with a 41° angle as illustrated in Figure 12. Study by Liu and Ting [2007] showed that an orificed perforated plate of 6 mm thickness, 41° orifice angle, and 43% solidity ratio was appropriate for generating quasi-isotropic turbulence.

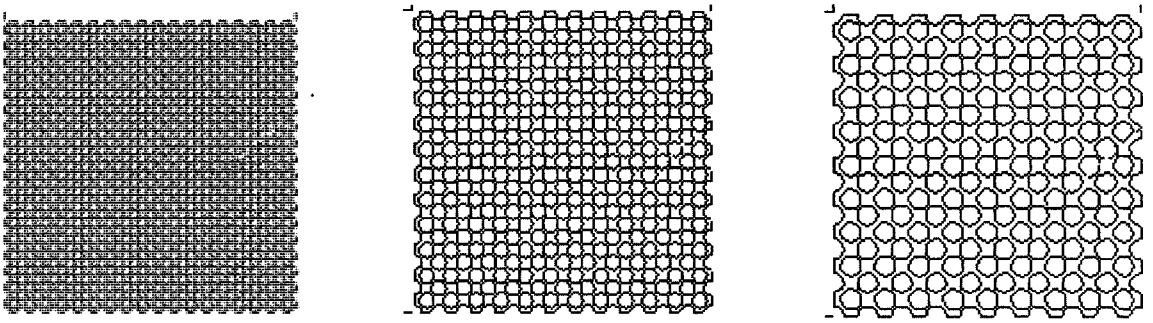

(a) D = 25 mm (b) D = 37.5 mm (c) D = 50 mm

Figure 11: Schematic of the orificed perforated plates (a) Plate D-25, (b) Plate D-37.5, and (c) Plate D-50.

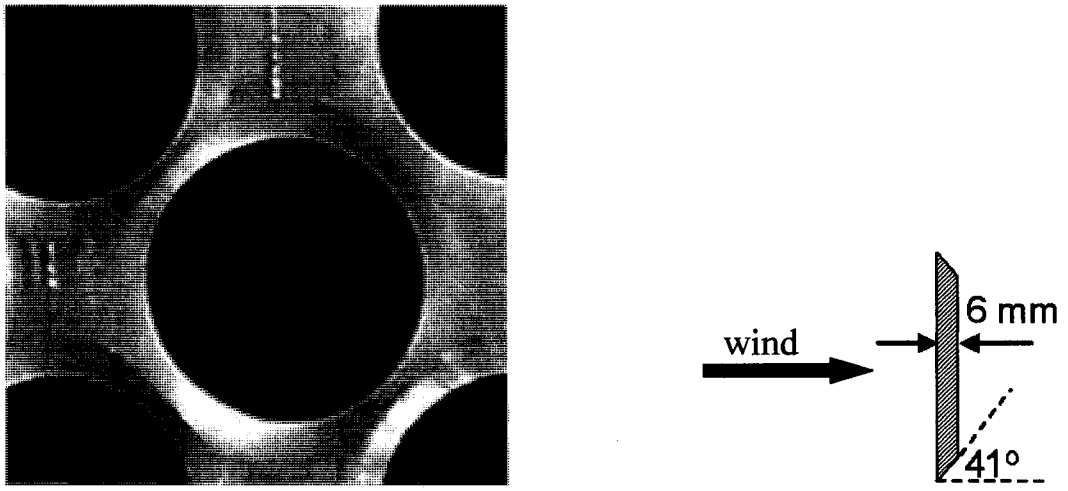

(a) Looking upstream to the plate (b) Cross section of the plate

Figure 12: The orificed perforated plate

The proper combination of orificed perforated plate hole diameter, sphere size, and sphere location enabled the independent alterations of turbulence intensity and relative integral length scale (Λ/d) from 1.9% to 10% and from 0.04 to 3.25, respectively at each studied Reynolds number from 2.2×10^4 to 8×10^4.

3.2 CHARACTERISTICS OF THE TURBULENT FLOW MEASUREMENT IN WIND TUNNEL

To quantify the flow velocities and the associated turbulence parameters, a hot-wire system composed of a hot-wire probe, a temperature probe, a Dantec Streamline hot-wire anemometer (CTA) modules, an A/D converter, a light-duty 2-D traversing system, and a computer were utilized as shown in Figure 13. In Experiment I with PVC spheres, a single normal wire of DISA type 55P11 with Dantec Streamline 55C90 hot-wire anemometer (CTA) module were used. In Experiment II with wooden spheres, hot-wire measurement system included an X-type hot-wire probe of Dantec type 55P61 with two Dantec Streamline 55C90 hot-wire anemometer (CTA) modules.

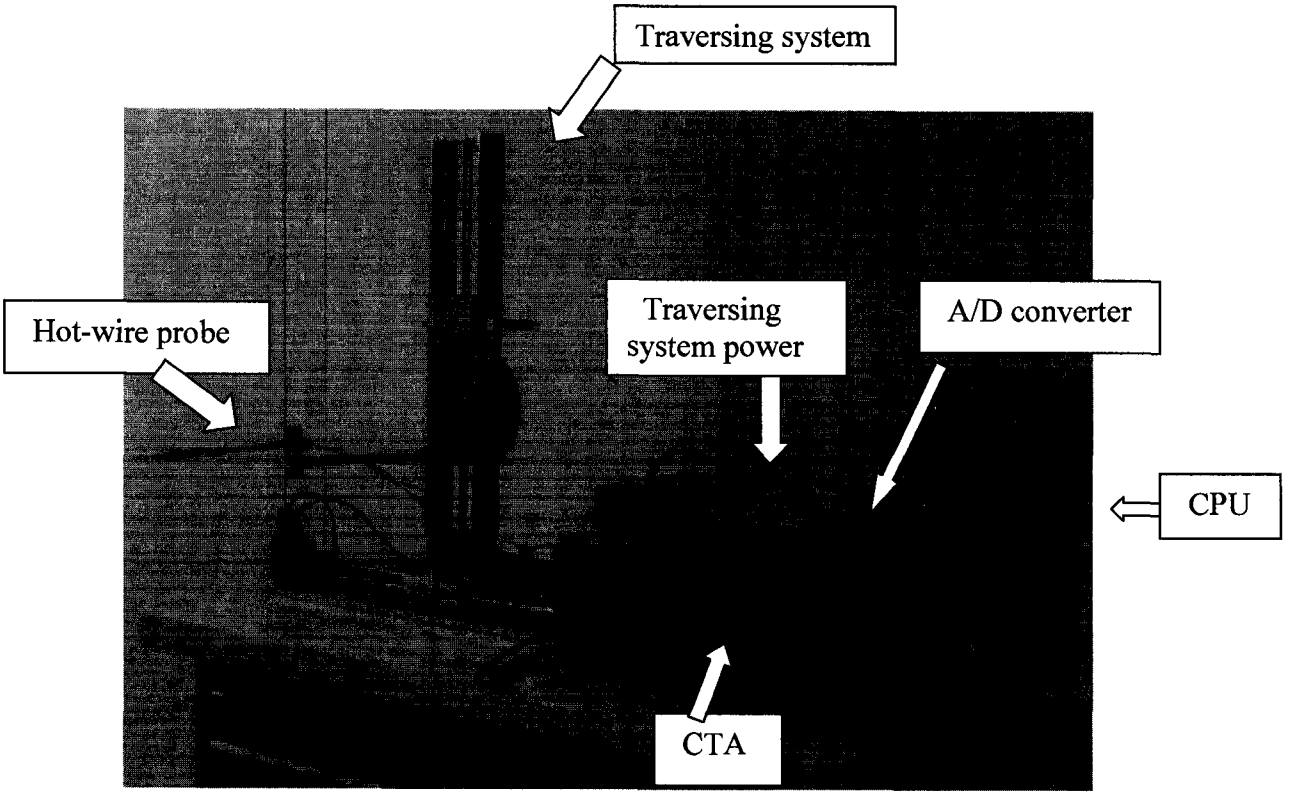

Figure 13: Hot-wire system

3.2.1 MEASUREMENT VELOCITY

In Experiment I, velocity measurement was conducted by using a single normal hot-wire of DISA type 55P11 at the desired location downstream of the orificed perforated plate. The hot-wire anemometer used in this experiment was a Dantec Streamline 55C90 CTA module installed within a Dantec 90N10 frame. In Experiment II, velocity measurement was conducted by using an X- probe of Dantec type 55P61. In this case,

two anemometer modules in the 90N10 frame were used. The 90N10 frame consisted of three major parts: a power supply, a controller and a temperature transducer. The power supply provided all the power needed for the operation of the StreamLine® system. The controller acted as a gateway between the computer and the StreamLine® system.

The traverse system was mounted at the desired location downstream of the orificed perforated plate for supporting the hot-wire probe and the temperature probe. Liu and Ting [2007] have shown that the turbulence generated by the orificed perforated plate remains non-isotropic until a distance of 10D downstream of the plate. Thus, all hot-wire data in the current study were collected within a range of 10D to 50D distance downstream of the orificed perforated plate. The instantaneous flow velocity in the streamwise direction was measured using either a single normal wire or a X-probe. A sampling frequency of 80 kHz was used over a sampling time of 125 s, resulting in 10,000,000 samples at each measurement location. The collected data were low-pass filtered at 30 kHz before further analysis. The process of selecting the sampling frequency and sampling number is explained in Appendix A. A Pitot-static tube was employed when adjusting the power supply to provide the desirable wind speed. It was removed during hot-wire and drag measurement.

3.2.2 CALIBRATION OF HOT-WIRE PROBES

The hot-wire probe was calibrated before each test to establish the relationship between the voltage output from the hot-wire anemometer and the flow velocity. The calibration system consists of a calibration module to be placed in the frame and a separate flow unit connected to the calibration module via cable. The system operates from a pressurized air supply and creates a free jet, where the probes are placed during calibration. There are two calibration systems.

The old calibration system used in Experiment I, as shown in Figure 14, includes a filter to take particles and oil, a nozzle of low turbulence level [Liu et al., 2004], of which the velocity of air flow can be varied from 0 to 30 m/s, a Pitot-static tube and a Dwyer® 475 Mark III digital-manometer with the resolution of ±0.1 Pa for velocity measurement reference. There is a temperature probe placed beside the hot-wire probe at the exit of the nozzle to obtain the value of air temperature in order to make temperature compensation

to the hot-wire output. To ensure the flow velocity to be close to the required value, a Pitot-static tube was used to adjust the reference velocity. From this, the flow velocity at the core of the jet was deduced.

The Dantec model Streamline 90H02 calibration system used in Experiment II, as shown in Figure 15, includes a filter to take particles and oil, four different nozzles of low turbulence level, of which the velocity of air flow can be varied from 0.02 m/s to 343 m/s (Mach 1), an elliptical contour to keep the boundary layer development small and ensure a flat jet profile.

The calibration process consists of two steps: i) A velocity calibration to establish the relationship between the hot-wire voltage output and the given flow velocity; and ii) A yaw angle calibration to identify the dependence of the hot-wire voltage output on the relative position of the hot-wire sensor to the instantaneous flow vector. Because a 1D probe was utilized, no yaw angle calibration was needed in Experiment I. However, it is required in Experiment II where the X-probe is used. The details are given in Appendix B.

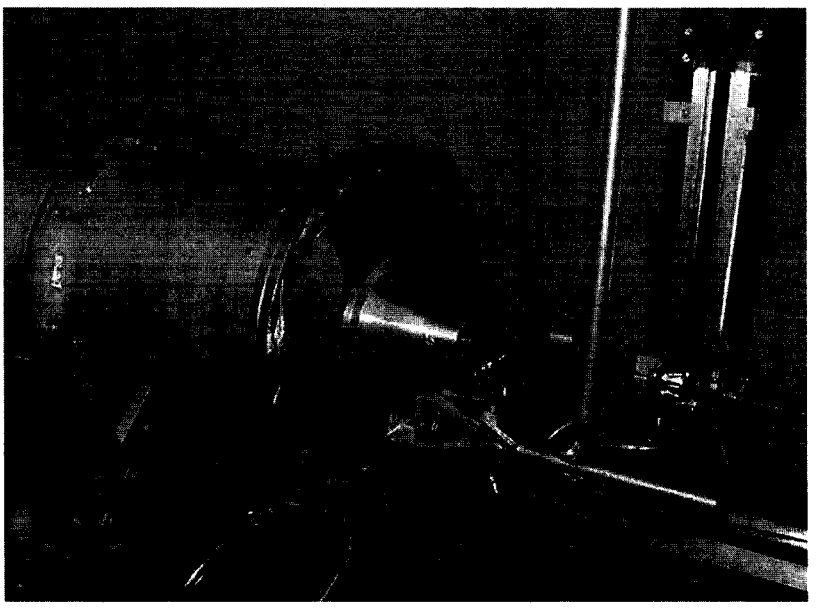

Figure 14: Old hot-wire calibration system

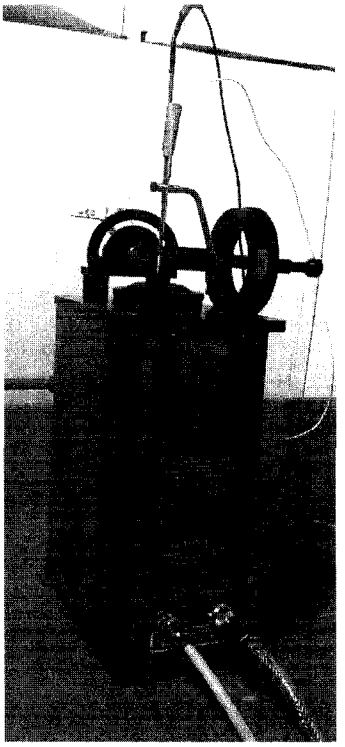

Figure 15: Dantec Model streamline 90H02 hot-wire calibration system

3.2.3 HOT-WIRE DATA ANALYSIS

In Section 3.2.1, it was explained that at each sampling location, 1×10^7 samples were taken at a sampling frequency of f_s = 80 kHz, and low-pass filtered at 30 kHz. The minimum sampling number, N, associated with f_s was determined by sensitivity analysis of time-averaged velocity ($\overline{U}$), instantaneous fluctuating velocity (u) and integral length scale (Λ) as a function of sampling number. Details are given in Appendix A, which concludes that sampling number greater than 7×10^6 and 6×10^6 will provide satisfactory accuracy for $\overline{U}$, u and Λ for 1D probe and X-probe hot-wire measurement, respectively.

Flow velocities were found from the data collected by the hot-wire anemometer in terms of voltage values and the calibration data. The procedure was done via a MATLAB program as detailed in Appendix C. The program can convert each of the input voltage value to the instantaneous velocity as output.

a) 1D-probe hot-wire data analysis

The time averaged velocity ($\overline{U}$) of the flow was simply the average of all the samples acquired at any specific measurement location.

$$\overline{U} = \frac{\sum_{i=1}^{N} U_i}{N} \tag{3}$$

where

$$U_i = C_0 + C_1 E_c + C_2 E_c^2 + C_3 E_c^3 + C_4 E_c^4 \tag{4}$$

where E_c is the voltage data given by the hot-wire system and C_0, C_1, C_2, C_3, and C_4 are the coefficients achieved from calibration.

By taking the difference between the time averaged velocity and the instantaneous velocity (U_i), the instantaneous fluctuating velocity (u) was obtained. The root mean square velocity is deduced from:

$$u_{rms} = \sqrt{\sum_{i=1}^{N} \frac{(U_i - \overline{U})^2}{N-1}} \tag{5}$$

where N is the sampling number ($N = 10^7$). The turbulence intensity (Tu) was simply obtained from:

$$Tu = 100 \times \frac{u_{rms}}{\overline{U}} \tag{6}$$

The integral length scale (Λ)

$$\tau_\Lambda = \int_0^\infty \varsigma(\tau) d\tau \tag{7}$$

was deduced via

$$\tau_\Lambda = \left(\sum_{i=1}^{N-1} \varsigma(i\Delta t) \right) \Delta t \tag{8}$$

where the autocorrelation factor (ς) for discrete samples was calculated from

$$\varsigma(m\Delta t) = \frac{\frac{1}{N-m} \sum_{i=1}^{N-m} (u_i u_{i+m})}{\frac{1}{N} \sum_{i}^{N} u_i^2} \tag{9}$$

where m was varied from 0 to N-1.

Invoking the Taylor's frozen hypothesis [Taylor, 1938], the integral length scale is then multiplied by the time averaged velocity at each location to obtain the corresponding integral length scale:

$$\Lambda = \overline{U} \cdot \tau_{\Lambda} \tag{10}$$

Validity of this hypothesis holds for maximum turbulence intensity less than 15% [Batchelor, 1967]. The maximum turbulence intensity in this study was 10%, hence the Taylor's frozen hypothesis is expected to be valid.

b) X-probe hot-wire data analysis

The time averaged velocities $(\overline{U})$ and $(\overline{V})$, as in Figure 16, of the flow were simply the average of all the samples acquired by considering the yaw angle at any specific measurement location.

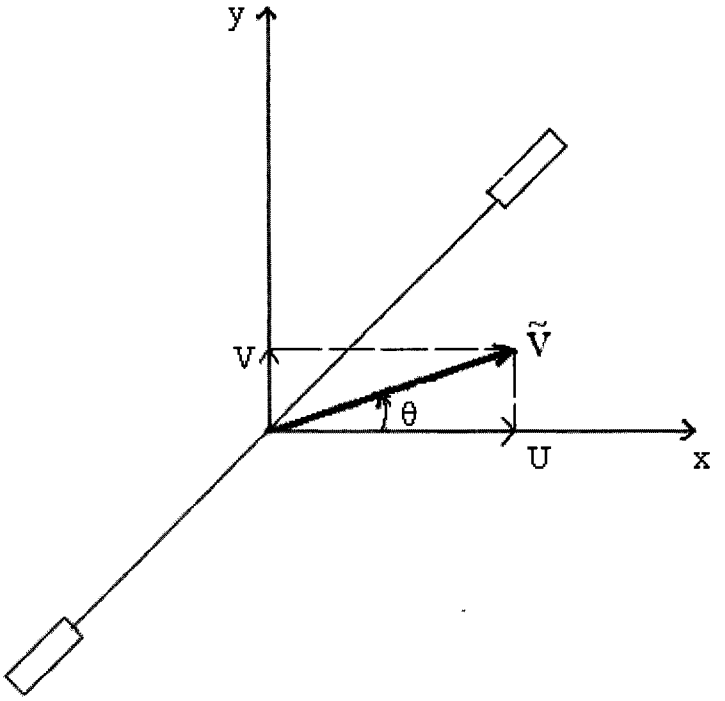

Figure 16: Schematic of flow velocity and hot-wire

If

$$U_{eff} = C_{01} + C_{11}E_{1c} + C_{21}E_{1c}^2 + C_{31}E_{1c}^3 + C_{41}E_{1c}^4 \tag{11}$$

$$V_{eff} = C_{02} + C_{12}E_{2c} + C_{22}E_{2c}^2 + C_{32}E_{2c}^3 + C_{42}E_{2c}^4 \tag{12}$$

where E_{1c} and E_{2c} are the voltages data given by the X-probe hot-wire and C_{01}, C_{11}, C_{21}, C_{31}, C_{41}, C_{02}, C_{12}, C_{22}, C_{32}, C_{42} are the coefficients achieved from calibration.

Then,

$$\tan(\beta) = (U_{eff} - V_{eff}) / [U_{eff} \times \tan(\alpha_2) + V_{eff} \times \tan(\alpha_1)] \tag{13}$$

where α_1 and α_2 are the yaw angles of two wires in the X-probe. The MATLAB program in Appendix C explains more details about this calculation.

Finally, the time averaged velocities were found by,

$$\overline{U} = \frac{\sum_{i=1}^{N} U_i}{N} \tag{3}$$

$$\overline{V} = \frac{\sum_{i=1}^{N} V_i}{N} \tag{14}$$

where

$$U_i = (U_{eff} - V_{eff}) / [2 + \tan(\beta) \times (\tan(\alpha_1) - \tan(\alpha_2))] \tag{15}$$

$$V_i = U_i \times \tan(\beta) \tag{16}$$

It is clear that $\overline{V} \approx 0$ in this experiment. By taking the difference between the time averaged velocities and the instantaneous velocities U_i and V_i, the instantaneous fluctuating velocities u and v were obtained. The root mean square velocities were deduced from:

$$u_{rms} = \sqrt{\frac{\sum_{i=1}^{N} (U_i - \overline{U})^2}{N-1}} \tag{5}$$

$$v_{rms} = \sqrt{\frac{\sum_{i=1}^{N} (V_i - \overline{V})^2}{N-1}} \tag{17}$$

where N is the sampling number ($N = 10^7$). The turbulence intensity (Tu) and the integral length scale (Λ) in the flow direction were simply obtained from Equations (6) and (10). It is clear that the difference between X-probe data analysis and 1D-probe data analysis is the effects of yaw angle in X-probe data analysis.

3.3 SPHERE SETUP

3.3.1 PVC SPHERES

Three different sizes of spheres (d = 20, 51, 102 mm) were used in Experiment I to cover a Reynolds number range of 2.2×10^4 to 8×10^4, and to enable independent control of Λ/d from 0.1 to 2.6. All spheres were made of PVC and polished by light grade Scotch® hand-pad. The mean surface roughness was 0.9677 μm. The maximum relative roughness (mean surface roughness / sphere diameter) was less than 0.4839×10^{-4}. Thus, the spheres can be considered to be mechanically smooth and hydraulically nearly smooth [Westerman & Sharcos, 1966; Hunt & Vaughan, 1996]; see Appendix E.

High strength polymer strings of 0.5 mm diameter (SF24G-150 model of the FUSION® brand) with maximum tensile load capacity of 10.9 kg were used to support the sphere. Each sphere was drilled with two threaded holes, both 9 mm in diameter and 20 mm in depth, instead of the hole of the smallest sphere, d = 20mm which had two hole of 5 mm in diameter and 9 mm in depth, for fastening the strings to the sphere via two screws, as shown in Figure 17.

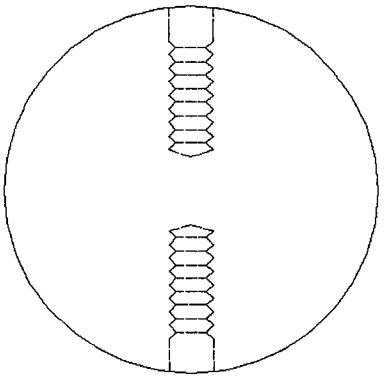

Figure 17: Schematic of threaded hole in the 65 mm sphere

After the screws were tightly secured to the sphere, the holes were filled with LEPAGE (5 MINUTE EPOXY). A total of eight strings were used, four of which were fastened to the top hole and another four to the bottom one, as shown in Figure 18. The other end of the top strings were fastened firmly and laid symmetrically to the two side walls of the wind tunnel, with each making an angle of $\alpha \pm 0.3°$ (= $40.4° \pm 0.3°$) with respect to the test section wall and $\beta \pm 0.3°$ (= $63.5° \pm 0.3°$) to the streamwise direction of

the wind tunnel. In the case of the bottom strings, the other ends were secured firmly to the floor of the wind tunnel making an angle of $\alpha' \pm 0.3°$ (= $44.8° \pm 0.3°$) with respect to the test section wall and $\beta' \pm 0.3°$ (= $59.7° \pm 0.3°$) to the streamwise direction of the wind tunnel.

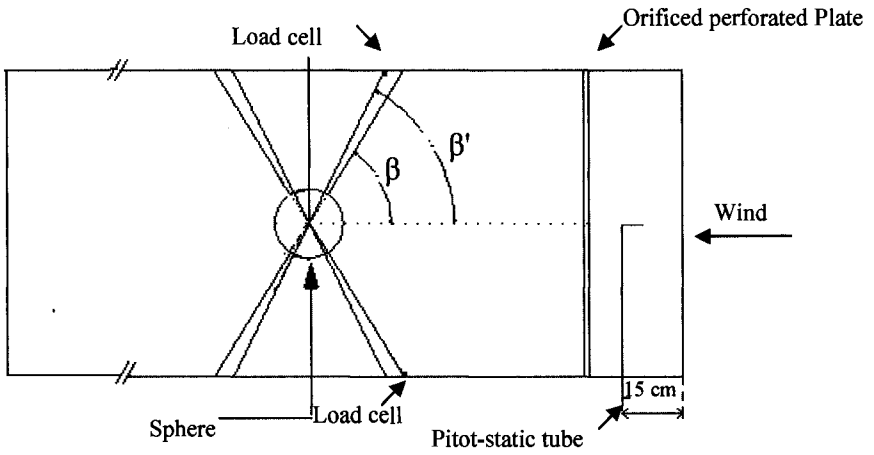

Figure18: Schematic of experiment layout

3.3.2 WOODEN SPHERES

Six different sizes of spheres (d = 20, 51, 65, 102, 140, 210 mm) were used in Experiment II to cover a Reynolds number range of 2.2×10^4 to 8×10^4, and to enable independent control of Λ/d from 0.04 to 3.25. All spheres were made of wood and polished and waxed. The mean surface roughness was 16.99 μm. The maximum relative roughness (mean surface roughness / sphere diameter) was less than 8.495×10^{-4}. Thus, the spheres can be considered to be mechanically and hydraulically close to smooth [Westerman & Sharcos, 1966, Hunt & Vaughan, 1996]; see Appendix E.

The polymer strings via two screws were used to support the sphere from top and bottom. Two holes of 5 mm in diameter and 20 mm in depth were threaded into each sphere, to allow the fastening of the supporting strings via two screws. An exception to this is that the smallest sphere which had two holes of 5 mm in diameter and 9 mm in depth. The setup is similar to setup of PVC spheres in Experiment I, as shown in Figure 18, except that in Experiment II the values of α , α', β and β' are not fixed. The calculation of these angles is explained in Appendix D.

3.4 DRAG MEASURMENT

3.4.1 LOAD CELL SPECIFICATIONS

To measure the drag force of the sphere, a model ELG-V-1N-L03M ENTRAN load cell as shown in Figure 19 was utilized to quantify the tensile force in the strings. It has a full scale reading of 1 N, and an over-range limit of 10 N. It was connected to a model MROJHHSG Electro-Numerics Amplifier which provides a 10 V excitation to the load cell.

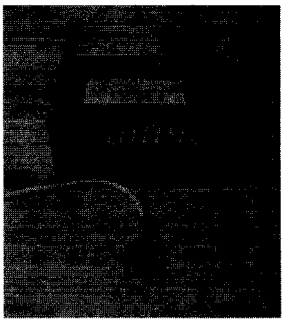

Figure 19: Load cell

3.4.2 LOAD CELL SETUP

For a supporting mechanism as portrayed in Figure 20, when the sphere is subjected to the wind, only the four upstream strings, two at the top and two at the bottom, would resist the drag force on the sphere. In a typical testing case with specified wind velocity and turbulence level, the load cell was attached to one of the top upstream strings and one of the bottom upstream strings to quantify the net load within these two strings. Due to the symmetric layout of the strings, the drag of the sphere was therefore determined by the summation of the horizontal streamwise components of the net loads in these two strings multiplied by two. The following equations were used to calculate the drag force from the collected load cell data; see Figure 21:

Streamwise net component in one top string:

$$F_{D_Top} = \sin(\alpha)\cos(\beta) \times F_{top} \tag{18}$$

Streamwise net component in one bottom string:

$$F_{D_Bottom} = \sin(\alpha')\cos(\beta') \times F_{bottom} \tag{19}$$

Total drag force on the sphere:

$$F_D = 2F_{D_Top} + 2F_{D_Bottom} \quad (20$$

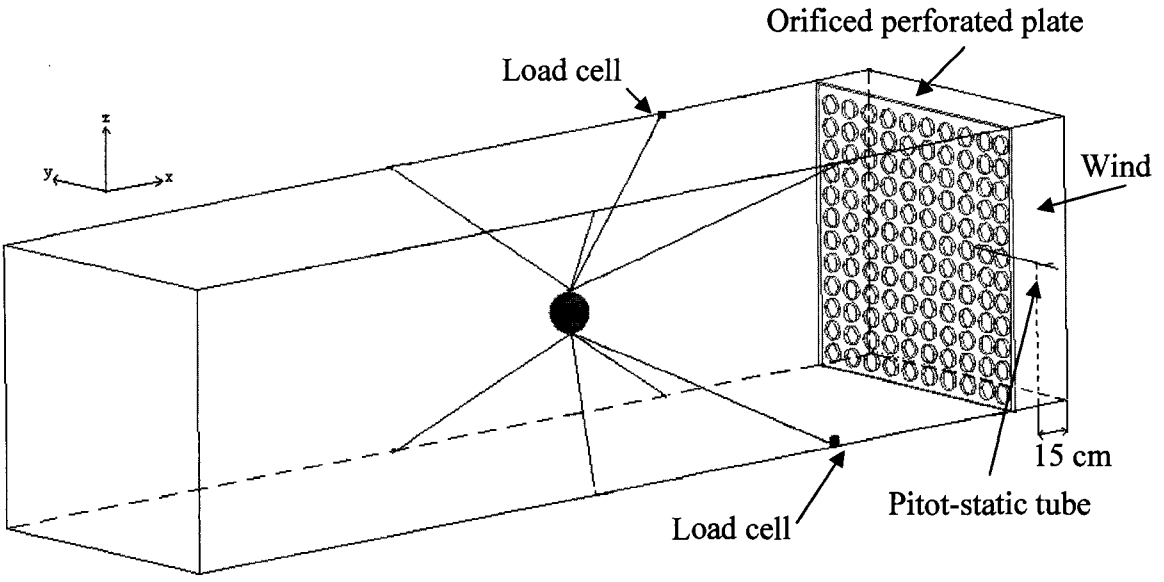

Figure 20: Schematic of the load cell setup with the sphere supported by strings

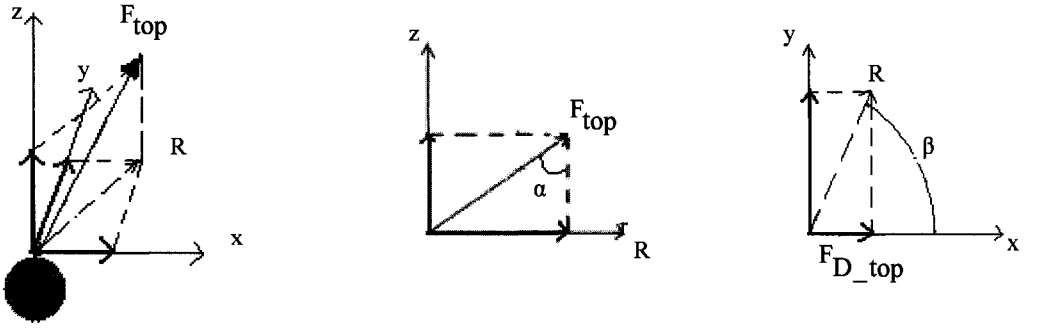

(a) Top strings

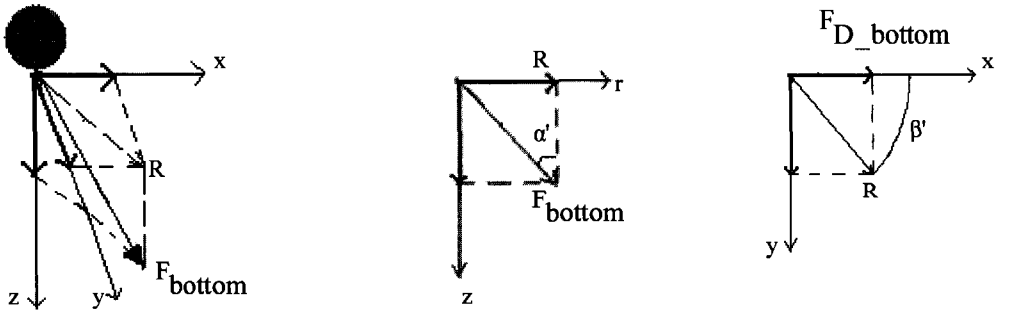

(b) Bottom strings

Figure 21: Geometric condition strings

3.4.3 LOAD CELL ADJUSTMENT

The upper and lower limits of the load cell were adjusted every time before measurement to maximize the sensitivity. To adjust the load cell, the sphere was installed with the load cell connected to it. As illustrated in Figure 22, a sample pulley system was designed. A string went over the pulley, with one end attached to the sphere, and the other attached to a weight. The main procedures are:

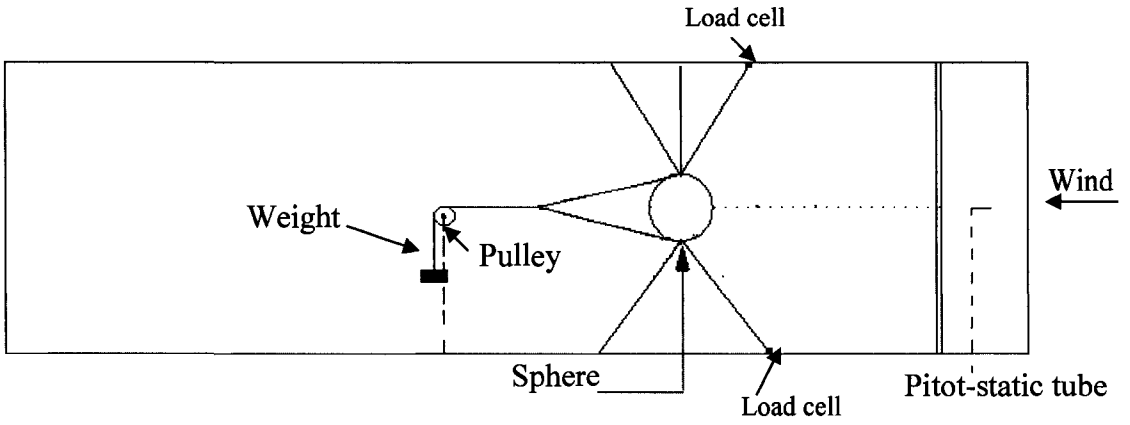

Figure 22: Load cell adjustment setup

1) Setup "LOW IN" menu in amplifier by adjusting 0 (N) for the lowest force in sphere setup;

2) Setup "HIGH IN" menu in amplifier by adjusting around 1 (N) for the highest range of the force in sphere setup

In all calculations the original equation was used. But the following steps were done to merely check that the equation, F (N) = 0.615 $F_{load\ cell}$ (mV) [StrainSense Ltd., 2007], is still valid.

3) Connect different weights to system and register the values in millivoltage (at least for 2 weights) (to check the calibration equation)

4) Compare the calibration equation of the load cell with the found data curve which showed the relation between the net force in the string and the load cell data which was delivered in mili-voltage from the amplifier.

CHAPTER 4: RESULTS AND DISCUSSION

Within the limit posted by the three available orificed perforated plates, the range of freestream velocity the wind tunnel can provide, and the length of the test section (over which the turbulence is nearly isotropic), attempt was made to pinpoint conditions (plate, wind speed, downstream location of the plate) which would provide at least three data points on the independent effect of Tu, Re, Λ and/or Λ/d. To compare with 'no turbulence' freestream flow scenario, measurements were also taken in the absence of the orificed perforated plate. It was found that in the smooth flow case, the freestream turbulence intensity was less than 0.3 %.

The main source of uncertainty in the 1D hot-wire measurement came from its calibration, which included three parts, i.e. the velocity measurement, the curve fitting and the digitized hot-wire anemometer output. The relative velocity uncertainty due primarily to Pitot-static tube in the calibration was 2.1%. The relative curve fitting uncertainty was 0.5%. The uncertainty in the digitized hot-wire anemometer output for the 12 bits A/D with an input range set as 0 to 10V was $(0.5\times10)/2^{12} = 0.0012V$ [Dantec dynamics, 2000]. Thus, the average uncertainties in $\overline{U}$ and u_{rms} were estimated to be 2.2% and 3%, respectively. For turbulence intensity, the average uncertainty was 3.7%, while that for integral length scale measurement was 6.5%. Details are explained in Appendix E.

In the X-Probe hot-wire measurement, the calibration was done automatically. Thus, the errors were reduced; see Appendix E. Therefore, in the X-Probe measurement, the average uncertainties in $\overline{U}$ and u_{rms} were estimated to be 1.1% and 1.7%, respectively. For turbulence intensity, the average uncertainty was 2%, while that for integral length scale measurement was 3.6%.

In the second part of the experiments, drag force measurement was performed using a load cell to achieve drag coefficient on the three spheres. The uncertainty in the drag measurement came from four different sources, i.e. the sphere diameter measurement, the velocity measurement, the air density calculation, and the load cell measurement. The diameter of the sphere was measured with a dial-caliper. The caliper has a resolution of 0.0254 mm and an accuracy of ±0.0127 mm. On the other hand, repeated measurements

showed a repeatability uncertainty of ±0.8 mm. Thus, the total uncertainty of sphere diameter was 1.8%. The uncertainty in the mean velocity measurement was 2.2% and 1.1% in Experiment I and Experiment II, respectively. The uncertainty in the calculation of the air density was negligible in comparison with others. Finally, since the drag coefficient C_D was calculated as $C_D = F_D / \left[0.5\rho U^2 \left(\pi d^2/4\right)\right]$, the maximum and nominal uncertainties of drag coefficient were almost 10.5% and 7.8% in this study.

4.1 CHARACTERISTICS OF FLOW DOWNSTREAM OF THE ORIFICED PERFORATED PLATES

Flow velocity was measured by 1D and 2D hot-wires from 10D to 50D downstream of the orificed perforated plates and from 0.25 m to 2.5 m downstream the inlet of the wind tunnel for the 'smooth flow' case in Experiments I and II. Root mean square velocity, relative turbulence intensity, integral length scale and/or relative integral length scale were deduced from hot-wire data via the equations given in Section 3 with the help of the appropriate MATLAB programs (Appendix C).

4.1.1 ROOT MEAN SQUARE VELOCITY AND RELATIVE TURBULENCE INTENSITY

Figure 23 shows the variation of the rms velocity along wind tunnel at different mean velocities in a center point of the test section at different distance of inlet of the wind tunnel. It is clear that the rms velocity decreases with the increase of downstream distance from the orificed perforated plate due to the decay in flow turbulence. In 1D hot-wire experiment with manual calibration system, the maximum and average uncertainties in u_{rms} are 3.7% and 3%, respectively. As shown in Appendix F, the results of X-probe confirm the same variation of the rms velocity along wind tunnel. In 2D hot-wire experiment with automatic Dantec Model streamline 90H02 hot-wire calibration system, the maximum and average uncertainties in u_{rms} are 2% and 1.7%, respectively; see Appendix E. Higher uncertainty is for smaller distance from the hotwire in all Reynolds numbers which are about maximum uncertainty shown in one point as an example.

Figure 24 shows the turbulence intensity along wind tunnel at different mean velocities in a center point of the test section at different distance of inlet of the wind

tunnel. By comparing the plots in Figure 24, the effect of downstream location on flow turbulence intensity can be observed to be similar to rms velocity changes. In 1D hot-wire experiment with manual calibration system, the maximum and average uncertainties in Tu are 4.3% and 3.7%, respectively. Also, the results of X-probe shown in Appendix F give the same conclusion about the changes of turbulence intensity along wind tunnel at different mean velocities. In 2D hot-wire experiment with automatic calibration system, the maximum and average uncertainties in Tu are 2.4% and 2%, respectively; see Appendix E.

Another observation is that the difference in the magnitude of rms velocity (and also turbulence intensity) between the 10D and 20D downstream locations is much larger as compared to these between the 30D and 50D. This can likely be explained by the effects of the exponential decay law, according to which the turbulence dies down exponentially with the distance traveled.

As shown in Figure 23, at higher mean velocity, the effective rms velocity is higher. This is because that the energy dissipation rate is much higher when closer to plates as compared to those farther downstream, which agrees with the exponential decay law. Figure 24 shows nearly fixed values for the relative turbulence intensity except for Figure 24(a) data. In Figure 24(a), the relative turbulence intensity has decreased slightly by increasing the mean velocity. This may be due to increase of average and root mean square velocity which increase the decay rate of $u_{rms} / \overline{U}$. The X-probe results concur with all the above explanation, too (Appendix F).

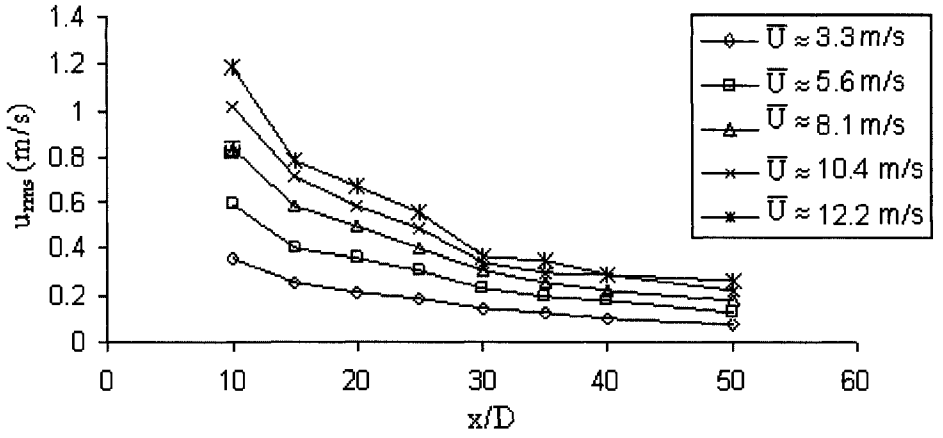

(a) Plate D = 25 mm

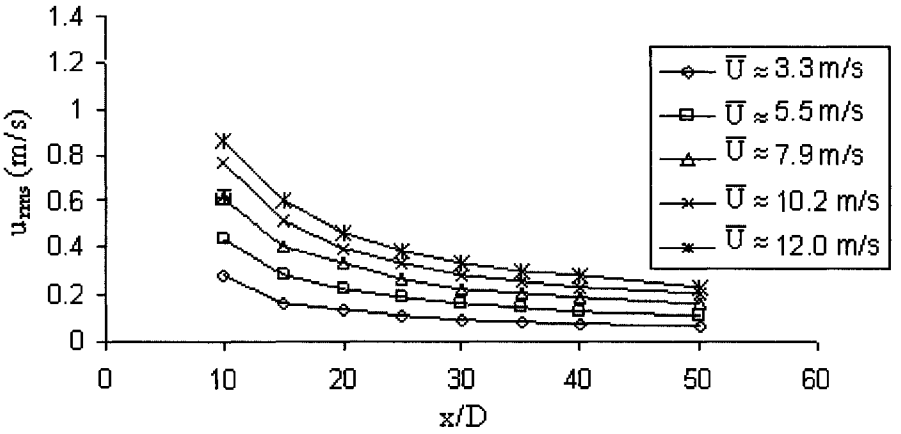

(b) Plate D = 37.5 mm

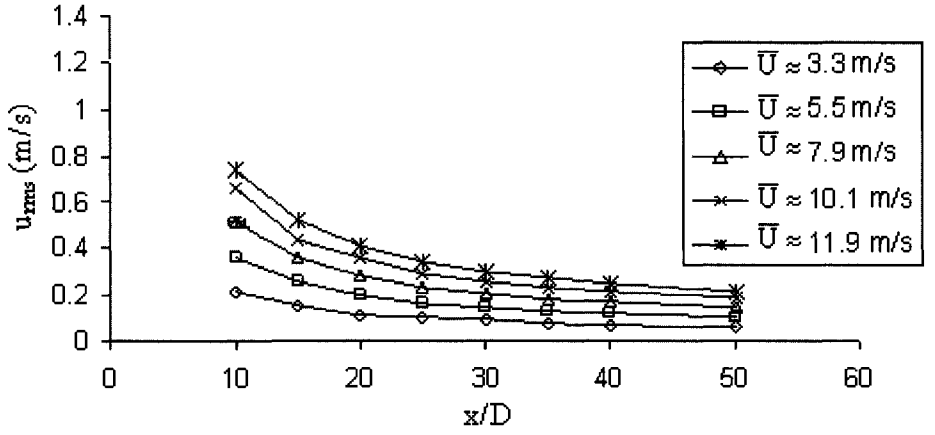

(c) Plate D = 50 mm

Figure 23: Variation of rms velocity (m/s) with respect to (x/D) in 1D hot-wire measurement: (a) with perforated plate D-25 (b) with perforated plate D-37.5 and (c) with perforated plate D-50 Tu%

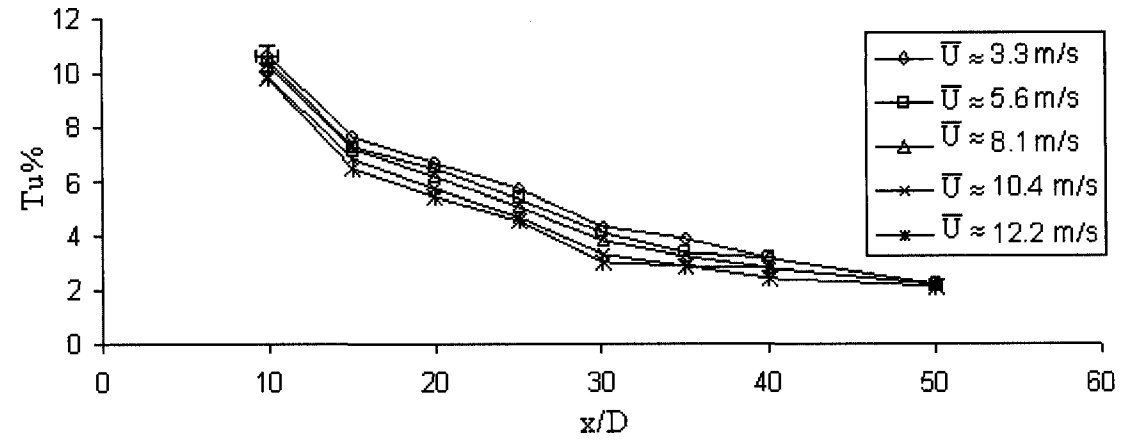

(a) Plate D = 25 mm

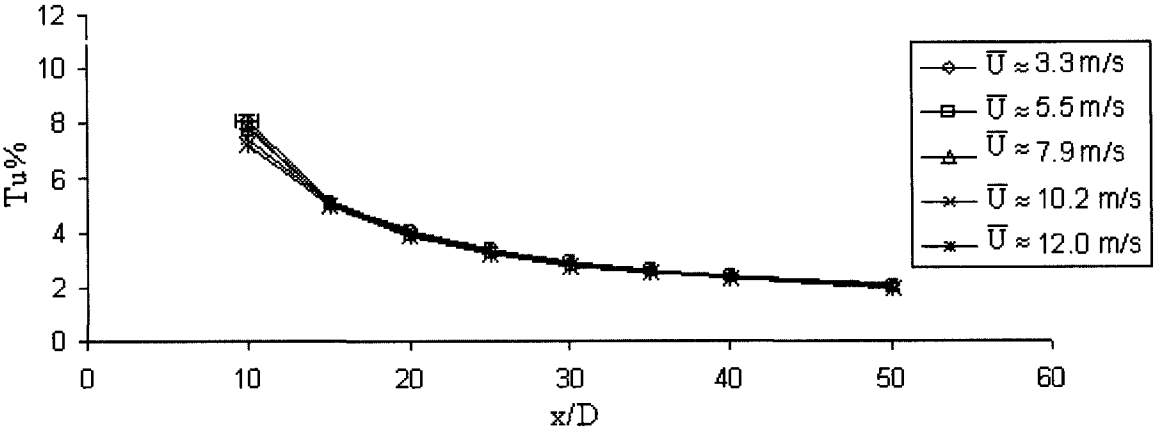

(b) Plate D = 37.5 mm

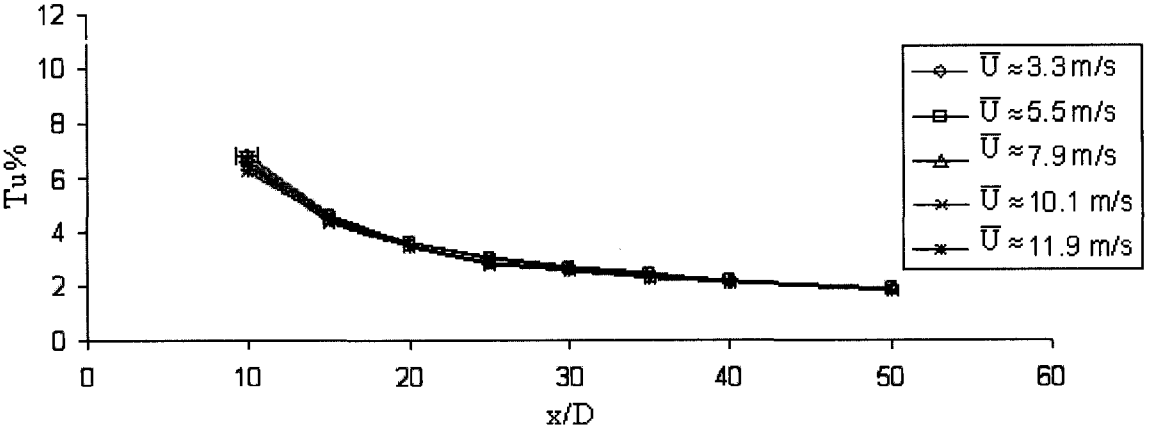

(c) Plate D = 50 mm

Figure 24: Variation of relative turbulence intensity with respect to (x/D) in 1D hot-wire measurement: (a) with perforated plate D-25 (b) with perforated plate D-37.5 and (c) with perforated plate D-50

4.1.2 INTEGRAL LENGTH SCALE

Integral length scale represents the scale of the energy containing eddies. The magnitude of integral length scale is largely dependent on the dimensions of the size of the holes and the spacing between them. In this study, the three orificed perforated plates described in Section 3.1 have the same solidity ratio by choosing suitable number of holes in each plate and the spacing between them have been carefully chosen to ensure that quasi-isotropic turbulence is generated [Liu et al., 2007]. The integral length scales corresponding to turbulent flow generated by different plates at different mean velocities are shown in Figure 25. Figure 25 shows that integral length scale is higher for larger mean velocity. Also, Λ is increased with increasing x/D as expected. In 1D hot-wire experiment with manual calibration system, the maximum and average uncertainties of the integral length scale are estimated to be approximately 7.8% and 6.5%. The results of X-probe measurement in Appendix F show the similar results, too. And, in 2D hot-wire experiment with automatic calibration system, the maximum and average uncertainties in Λ are 4.2% and 3.6%, respectively; see Appendix E.

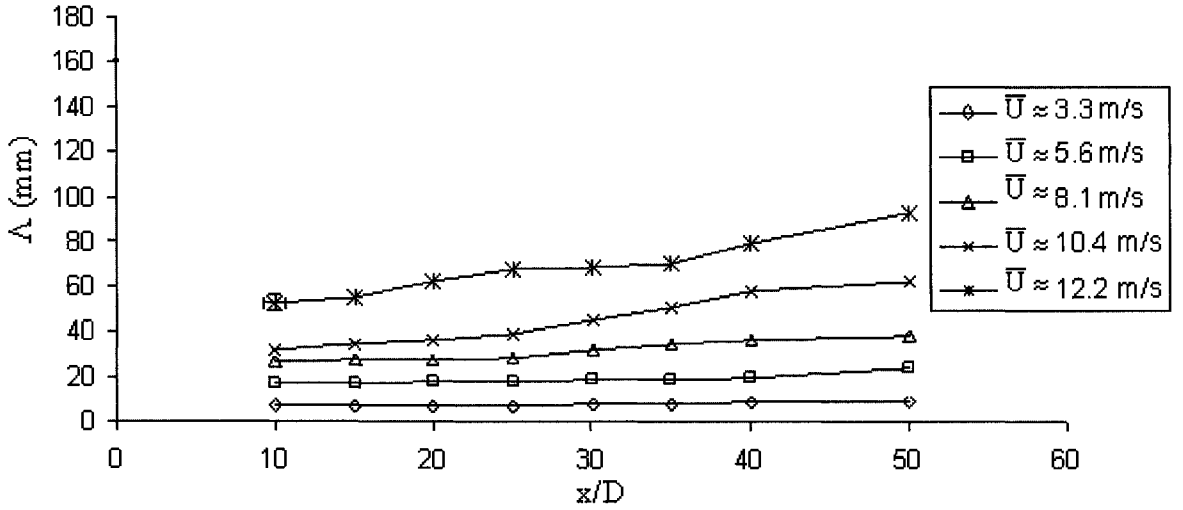

(a) Plate D = 25 mm

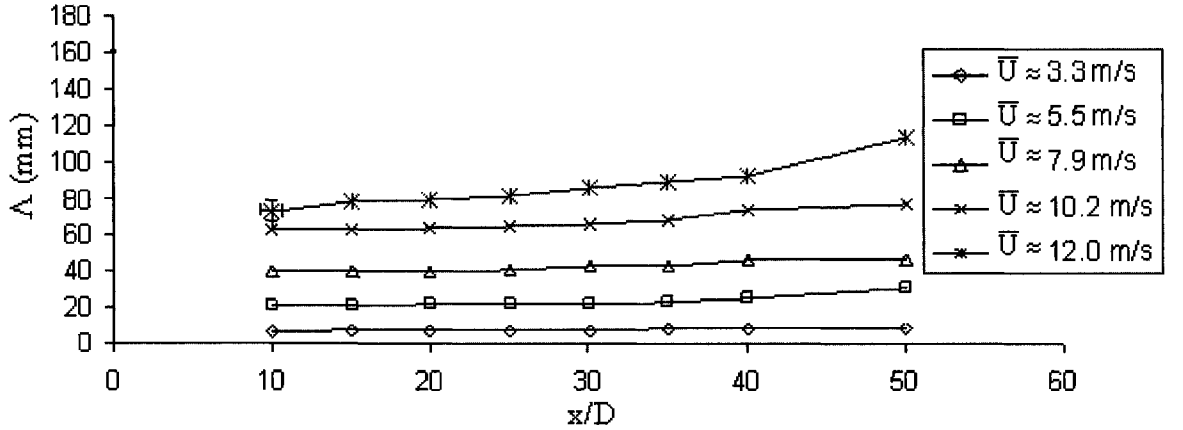

(b) Plate D = 37.5 mm

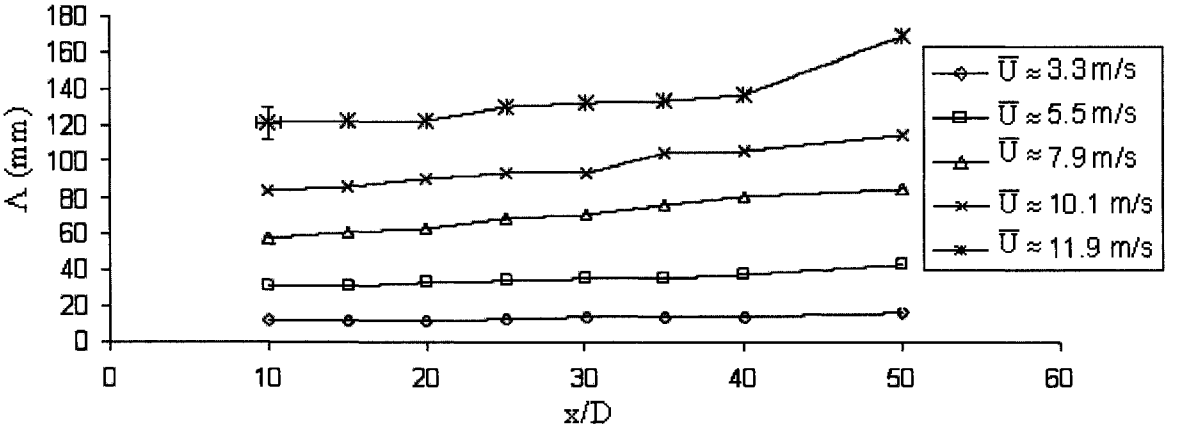

(c) Plate D = 50 mm

Figure 25: Variation of integral length scale with respect to (x/D) in 1D hot-wire measurement: (a) with perforated plate D-25 (b) with perforated plate D-37.5 and (c) with perforated plate D-50

4.2 DRAG RESULTS

To find out whether the effect of blockage is negligible or not, in the following sections, blockage effect on the drag coefficient of the sphere in "smooth flow" is studied. Then, the effects of integral length scale, relative integral length scale, turbulence intensity and Reynolds number on the drag coefficient of a sphere are investigated.

4.2.1 BLOCKAGE EFFECT ON DRAG COEFFICIENT

In wind tunnel tests, blockage ratio is defined as the ratio between the cross-sectional area of a sphere and that of the test section. To ensure that blockage ratio is not an issue in Experiment I, C_D of PVC spheres is plotted versus blockage ratio in Figure 26. Also, to make the blockage effect clear in Experiment II, C_D of wooden spheres is plotted versus blockage ratio in Figure 27. The sample data points from Phoreman et al. [2007] were given in Figure 8. Phoreman et al. [2007] found that once the blockage ratio was beyond 0.02, for Reynolds number less than the critical value ($Re < Re_{cr} \approx 3\times10^5$), the drag coefficient of the sphere was increased, and for $Re \geq Re_{cr}$, the drag coefficient of the sphere was decreased; see Figure 8. As shown in Figure 26, the maximum blockage ratio of 0.015 encountered in Experiment I has a negligible influence on the C_D value. But, as shown in Figure 27, in Experiment II, the blockage ratio is changed from 0.0005 to 0.0615. In "smooth flow" situation, similar to Phoreman et al. [2007] results, for $Re < Re_{cr}$, the drag coefficient of the sphere was increased once the blockage ratio was beyond 0.02. The effect of blockage, nevertheless, is small even at a blockage ratio of 0.027. This is especially true at higher Reynolds numbers. The increase of C_D in lower Reynolds number is clear for blockage ratio of 0.0615. In this study, the couple of data points with a blockage ratio of 0.0615 are only for in $Re = 8\times10^4$ in which the blockage ratio of 0.0615 has a relatively small effect.

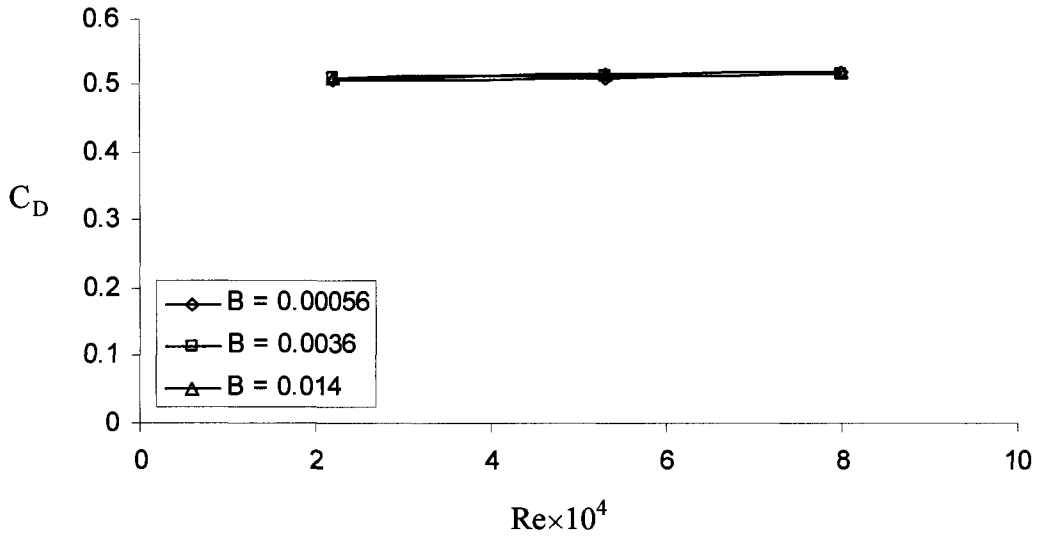

Figure 26: Blockage effect on the drag coefficient of PVC spheres in "smooth flow"

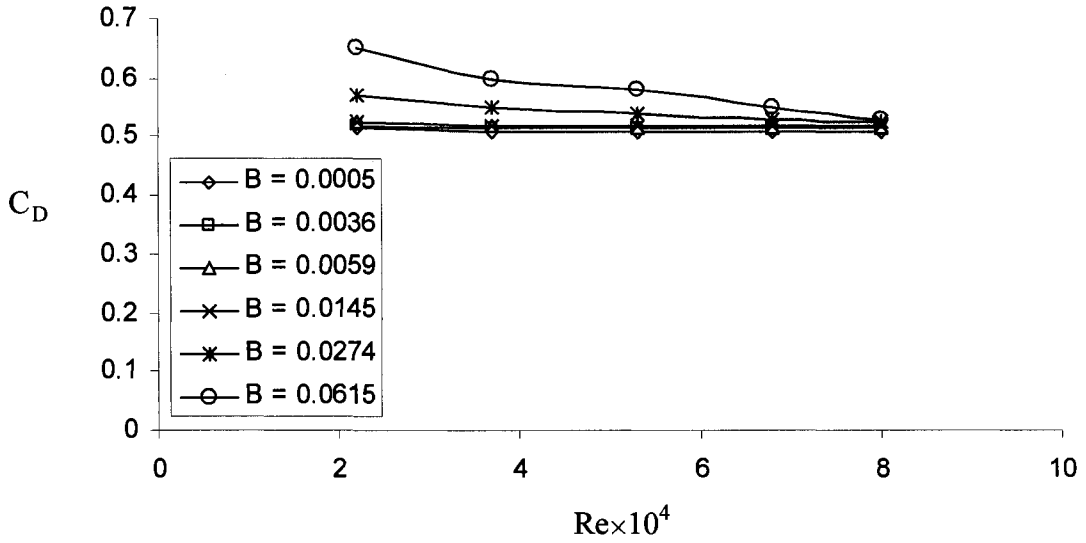

Figure 27: Blockage effect on the drag coefficient of wooden spheres in "smooth flow"

4.2.2 DRAG OF SPHERE UNDER "SMOOTH FLOW" CONDITION (Tu < 0.3%)

In the absence of the orificed perforated plate, the turbulence intensity Tu in the wind tunnel was measured to be less than 0.3%. Thus, the measured drag is expected to be close to the standard data in Figure 1. Figures 26 and 27 portray a comparison between the C_D-Re relation achieved in this study and the standard curves. The values of drag

coefficients obtained in this study are within the estimated nominal 7.8%~7.6% uncertainty ranges in Experiments I and II.

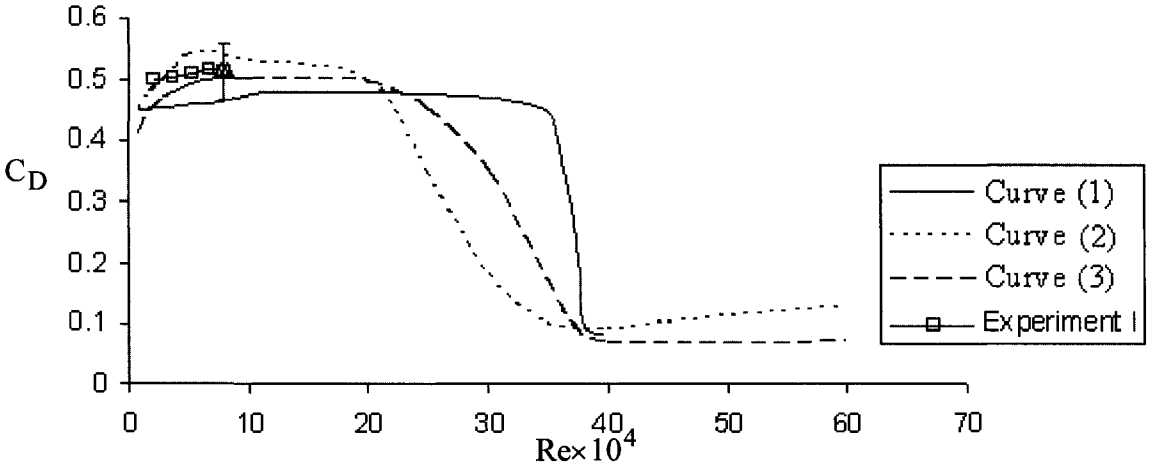

(a) Experiment I (PVC Spheres)

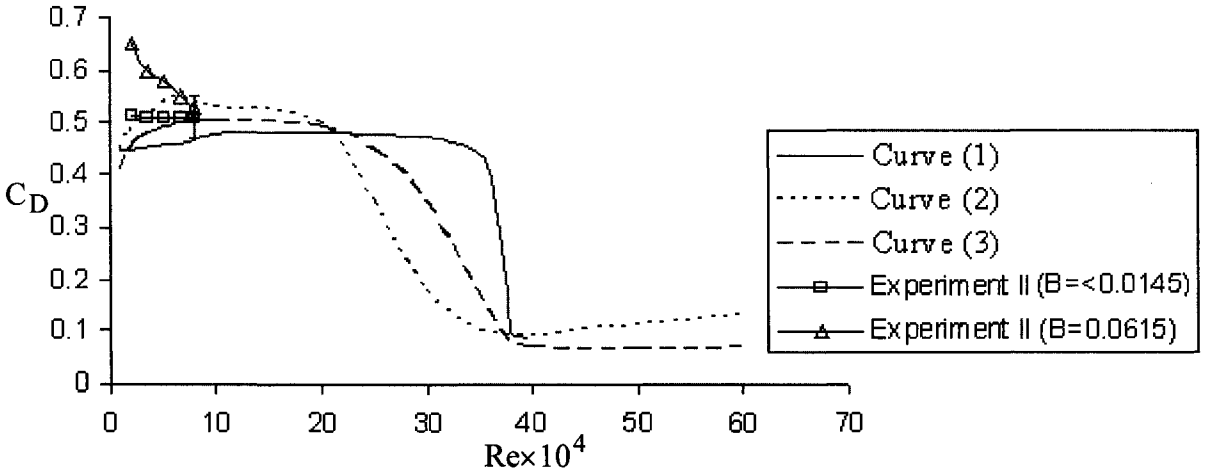

(b) Experiment II (Wooden Spheres)

Figure 28: Drag coefficient versus Reynolds number in the absence of orificed perforated plate in comparison with other standard curves, (Curve (1): Schlichting [1979] and Lee [1987], Curve (2): Lapple and Shepherd, [1940] and Clift and Gauvin [1970 & 1971], Curve (3): Achenbach [1972])

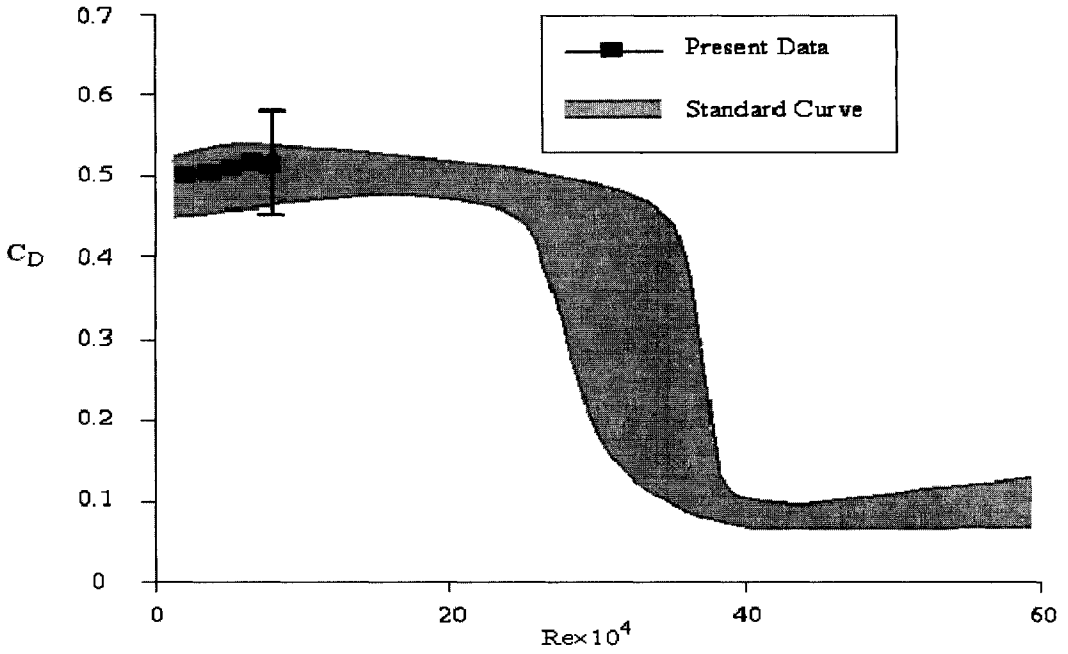

(a) Experiment I (PVC Spheres) $B \approx 0.062$ $B \approx 0.027$ $B < 0.015$

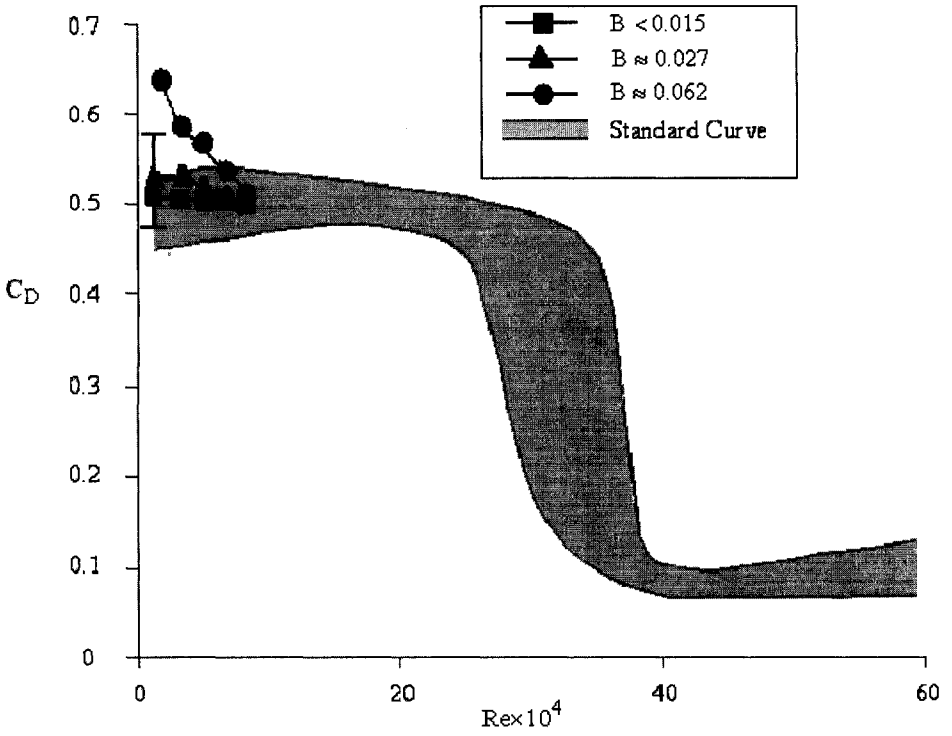

(b) Experiment II (wooden Spheres)

Figure 29: Drag coefficient versus Reynolds number in the absence of orificed perforated plate in comparison with Standard band

4.2.3 EFFECT OF TURBULENCE INTENSITY

When the boundary layer is changed from laminar to turbulent in the critical Reynolds number, the wake size becomes narrower. Previous results [Tyagi et al., 2006] show that at higher turbulence level, the size of the sphere wake becomes smaller at $Re < 3.5\times10^5$; recall that $Re_{cr} = 3.5\times10^5$ for smooth flow across a sphere [Torobin & Gauvin, 1959]. This appears to indicate that the critical Reynolds number is decreased for flow with higher turbulence intensity as discussed in previous subsection. In other words, higher turbulence intensity would decrease the critical Reynolds number and as a result, a significant drop in the drag coefficient of the sphere occurs at lower Reynolds number [Dryden et al., 1937; Bacon & Reid, 1924].

Figures 28 and 29 show the impact of turbulence intensity on the sphere drag while holding the relative integral length scale Λ/d fixed. The small extent on the y axis corresponds to the 'no turbulence' scenario obtained in the absence of an orificed perforated plate.

As shown in Figure 30, at $Re \approx 2.2\times10^4$, increasing the turbulence intensity only leads to marginal decrease in the drag coefficient. A typical case with $(\Lambda/d) \approx 0.6\sim0.9$ is shown in Figure 30; at a higher Reynolds number of 6.8×10^4, the turbulence intensity has a dramatically larger effect on the drag coefficient. In $Re = 8\times10^4$ and $\Lambda/d \approx 1$, ; the turbulence intensity effective on the drag coefficient decreases. This phenomenon will be further considered in Section 4.2.4. Larger still is the effect of Tu in decreasing C_D at $Re \approx 8\times10^4$ as portrayed in Figure 30. As shown in Figure 30, the drag coefficient drops below 0.1 when the turbulence intensity is 10%, for the relative integral length scale around 0.9.

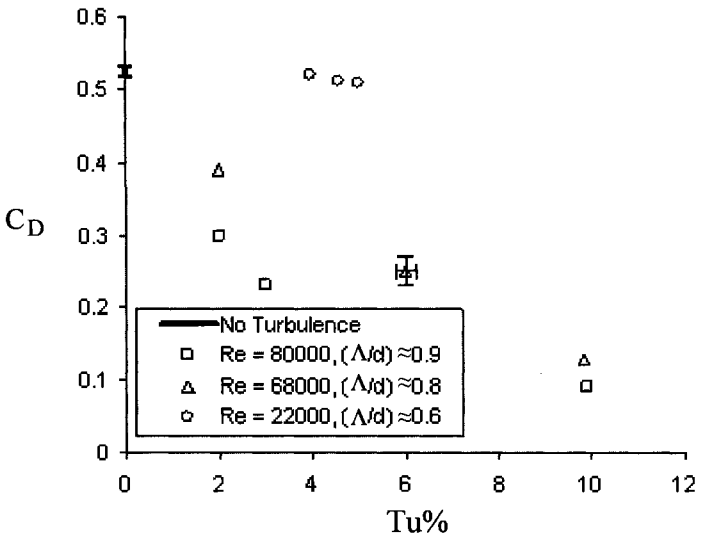

Figure 30: Impact of turbulence intensity on PVC sphere drag

As shown in Figure 31(a), at Re ≈ 3.7×10^4, increasing the turbulence intensity only leads to marginal decrease in the drag coefficient. At higher Reynolds numbers, Figures 29(b), (c), and (d), the turbulence intensity has a dramatically larger effect on the drag coefficient, especially for (Λ/d) ≈ 0.65. This phenomenon will be discussed in Section 4.2.4. Increasing the relative integral length scale above 0.65 can decrease the turbulence intensity effect on the drag coefficient; see Figure 31 for (Λ/d) ≈ 1.2. Larger still is the effect of Tu in decreasing C_D at Re ≈ 8×10^4 as portrayed in Figure 31. As shown in Figure 31(d), the drag coefficient drops below 0.1 when the turbulence intensity is around 6.3%, for the relative integral length scale 0.65. It is worth stressing that variation of the relative integral length scale, (Λ/d), to less and more than 0.65 achievable from the range of Λ/d in this study, appears to have a relatively more and lesser influence on lessening the reduction of the drag coefficient, C_D, by the turbulence intensity, Tu.

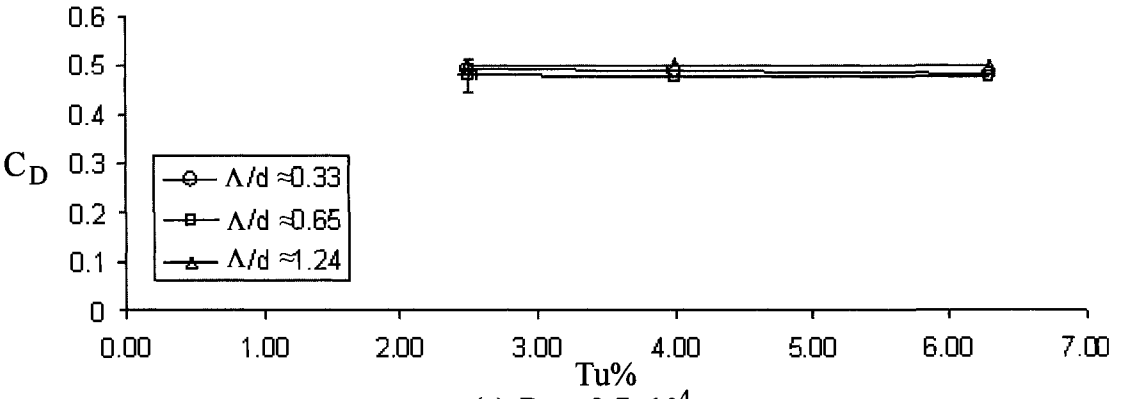

(a) Re = 3.7×10^4

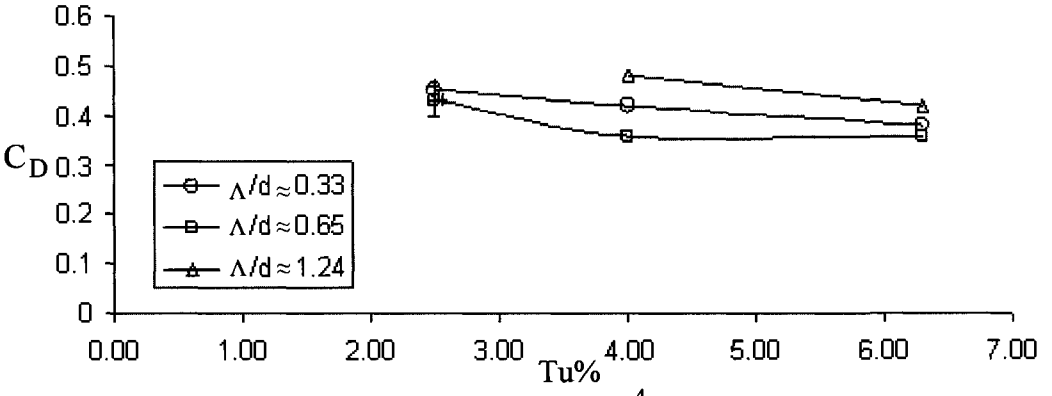

(b) Re = 5.3×10^4

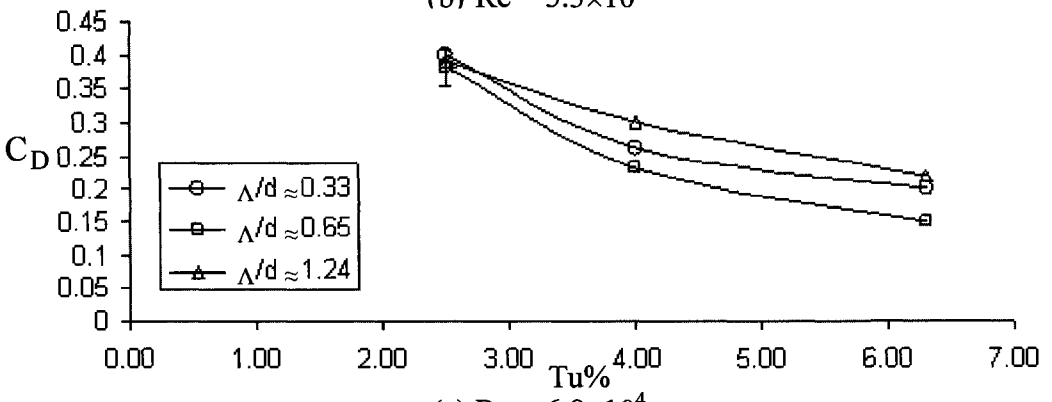

(c) Re = 6.8×10^4

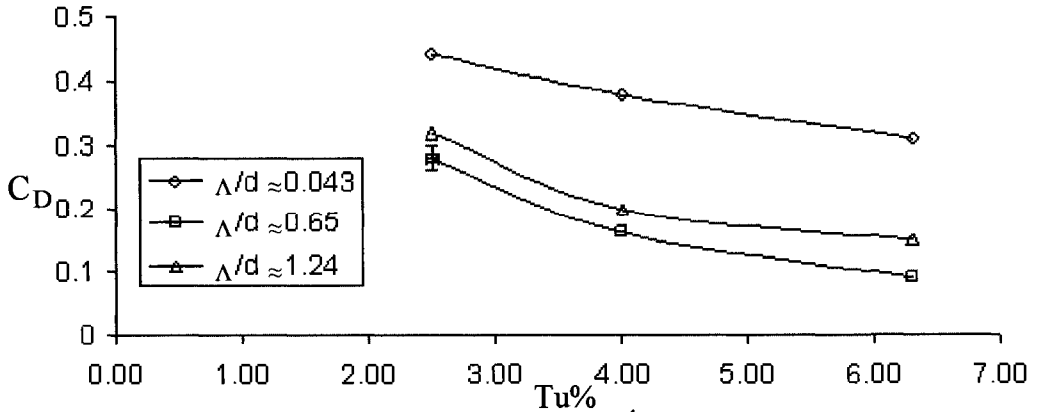

(d) Re = 8×10^4

Figure 31: Impact of turbulence intensity on wooden sphere drag

4.2.4 EFFECT OF RELATIVE INTEGRAL LENGTH SCALE

In Experiment I with PVC spheres, Figure 32 shows the impact of relative integral length scale Λ/d on the sphere drag while holding the turbulence intensity approximately fixed. In general, for all the relative integral length scale and the three turbulence intensity cases studied, the drag coefficient is observed to decrease with the increase of Reynolds number, which is in contrary to the 'no turbulence' case in Figure 28 (a). In each plot in Figure 32, between any two respective Reynolds numbers, in any specific relative integral length scale, there is higher drag coefficient for the lower Reynolds number. Also, it can be observed that particularly for $Re > 5.3 \times 10^4$, by increasing the relative integral length scale to range of 0.8~1.5, the drag coefficient of the sphere generally decreases and beyond that the drag coefficient of the sphere generally increases.

The increase of C_D with increasing Λ/d to more than 1~1.3, becomes significantly more obvious at higher turbulence intensity and Reynolds numbers. For example, at $Re = 6.8\times10^4$ and Tu = 6.3%, the drag coefficient increases more than 100%, from 0.13 to 0.28 when the relative integral length scale is increased from 0.7 to 1.7; see Figure 32(c). But, as shown in Figures 30(a), (b) and (c), the decrease of C_D with decreasing Λ/d up to around 0.8~1.5, is increased at lower turbulence intensity and Reynolds number.

As Figure 32(a) shows, for Λ/d up to 0.8~1.5 in different Reynolds number, the decrease of drag coefficient is significant. For example, as can be seen, at Tu = 2.5% and $Re \approx 5.3\times10^4$, drag coefficient decreases from 0.46 to 0.35 with increasing Λ/d from 0.55 to 0.75. But, by increasing Tu to 4% in Figure 32(b), the decrease of C_D by increasing Λ/d to 0.75~1.3 is lessened and as shown in Figure 32(c), for Tu = 6.3%, it is completely marginal.

If critical Reynolds number is defined as the Reynolds number at which the drag coefficient drops to around 0.1 [Torobin & Gauvin, 1959], then, we see, for example, this occurs in Figure 32(c) for $Re = 8\times10^4$ and $(\Lambda/d) \approx 1$. Thus, under this set of physical combination, Re_{cr} is reduced from $Re_{cr} = 3.5\times10^5$ in standard situation to approximately 8×10^4. The details about the size of the sphere used in results shown in Figure 32 are explained in Appendix G.

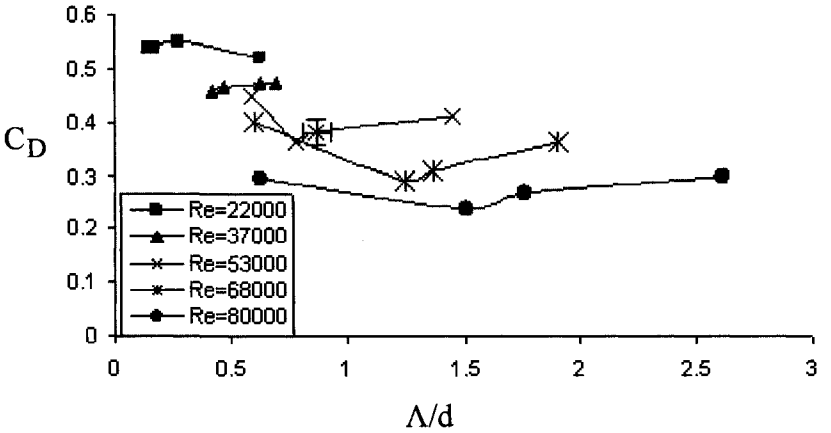

(a) Tu = 2.5%

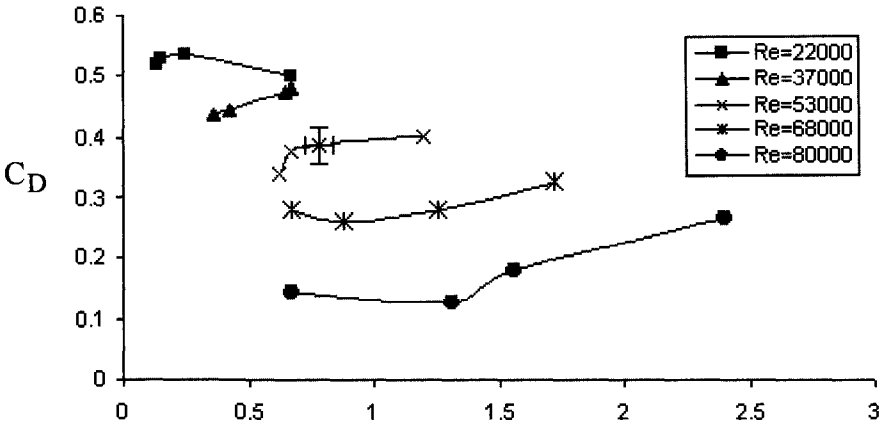

(b) Tu = 4%

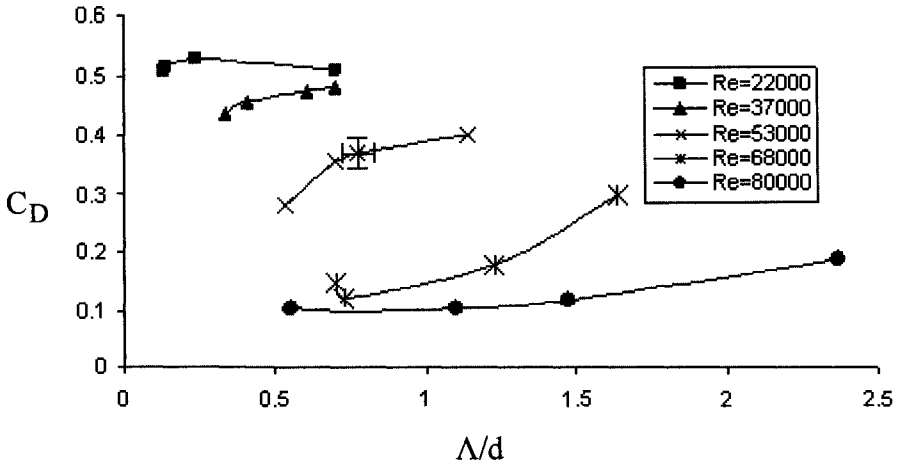

(c) Tu = 6.3%

Figure 32: Impact of relative integral length scale on PVC sphere drag when (a) Tu = 2.5% (b) Tu = 4% (c) Tu = 6.3%

In Experiment II with wooden spheres, Figure 33 show the impact of relative integral length scale Λ/d on the sphere drag while holding the turbulence intensity fixed. In general, similar to Figure 32, for all the relative integral length scale and the three turbulence intensity cases studied, the drag coefficient is observed to decrease with the increase of Reynolds number. In each plot in Figure 33, in any specific relative integral length scale, there is higher drag coefficient for the lower turbulence intensity. Also, it can be observed that by increasing the relative integral length scale to around $\Lambda/d \approx 0.65$, the drag coefficient of the sphere generally decreases but for beyond that the drag coefficient of the sphere increases, for any Reynolds number particularly $Re > 5.3\times10^4$.

In each plot of Figure 33, the magnitude of drag coefficient with changes of the integral length is not the same for different Reynolds numbers. For $Re < 5.3\times10^4$, this change rate is marginal. At higher Reynolds numbers, the decrease and subsequent increase of C_D with increasing Λ/d becomes more obvious. At $Re = 8\times10^4$, for $Tu \approx 6.3\%$, Figure 33 (e), for example, the drag coefficient decreases from 0.3 to 0.1 when the relative integral length scale is increased from 0.04 to 0.62. Also, as shown in Figure 33 (e), the drag coefficient increases more than 70%, from 0.1 to 0.17 when the relative integral length scale is increased from 0.62 to 1.22.

As shown in Figure 33(e) for $Tu = 6.3\%$ and $\Lambda/d \approx 0.62$, the drag coefficient reduces to less than 0.1 at $Re = 8\times10^4$. Thus, as defined by Torobin and Gauvin [1959], if critical Reynolds number is the Reynolds number at which the drag coefficient drops to around 0.1, in this experiment, Re_{cr} reduced from $Re_{cr} = 3.5\times10^4$ in standard situation to $Re_{cr} \approx 8\times10^4$. The details about which sphere size used in results shown in Figure 33 are explained in Appendix G.

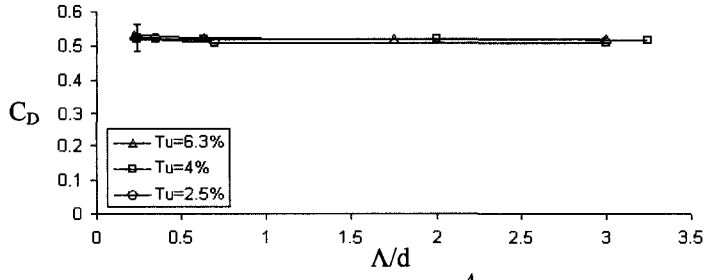

(a) Re = 2.2×10^4

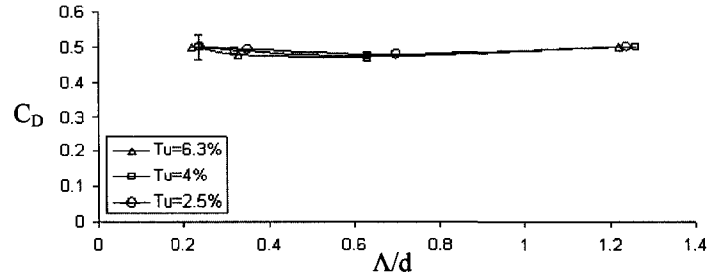

(b) Re = 3.7×10^4

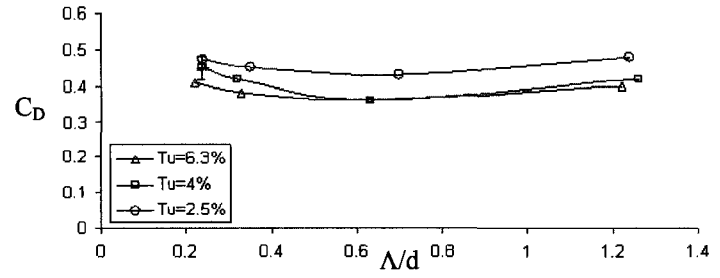

(c) Re = 5.3×10^4

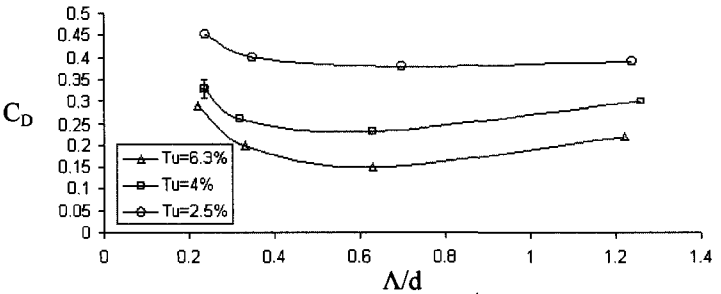

(d) Re = 6.8×10^4

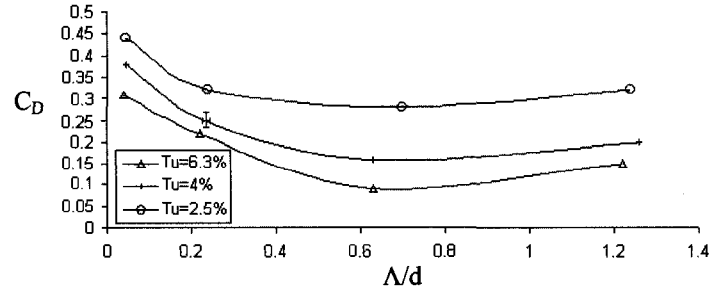

(e) Re = 8×10^4

Figure 33: Impact of relative integral length scale on wooden sphere drag when (a) Tu = 2.5% (b) Tu = 4% (c) Tu = 6.3%

4.2.5 EFFECT OF INTEGRAL LENGTH SCALE

In considering Λ/d effects on C_D, the effect of sphere size is eliminated. And, there should be no difference between the variation of C_D of the PVC sphere in different Λ/d and Λ. To confirm that the differences in the boundary layer thickness and wake size due to different sphere size do not affect C_D of the PVC spheres, all measurements were done for C_D-Λ in fixed turbulence intensities for different Reynolds numbers; see Figure 34.

Figure 34 shows the impact of integral length scale on the drag of PVC spheres while holding the turbulence intensity fixed. As can be observed from the figure, the effect of integral length scale on drag coefficient is similar to that of the relative integral length scale.

Increasing the integral length scale up to around 65 mm ($\Lambda/d \lesssim 1$) decreases the drag coefficient of the sphere and for $\Lambda \gtrsim 65$ mm ($\Lambda/d \gtrsim 1$) increases C_D. For example, in Figure 34(c), a turbulence intensity of 6.3% is able to advance Re_{cr} from 3.5×10^5 in "smooth flow" case to 8×10^4, provided $\Lambda \approx 65$ mm. The details about which sphere size used to get data of Figure 34 are given in Appendix G.

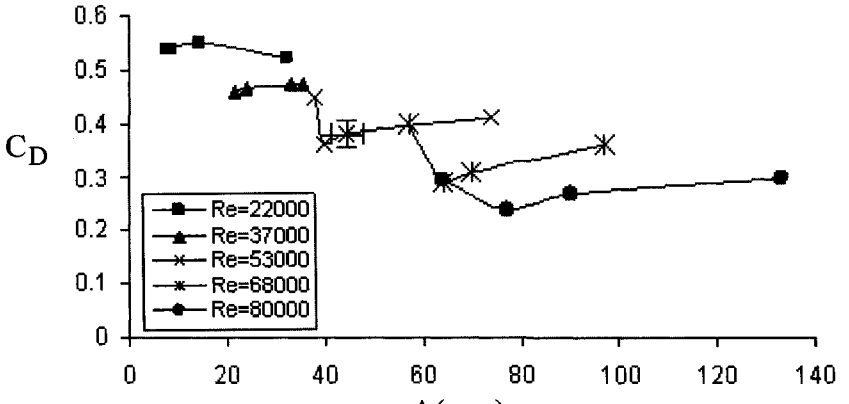

(a) Tu = 2.5%

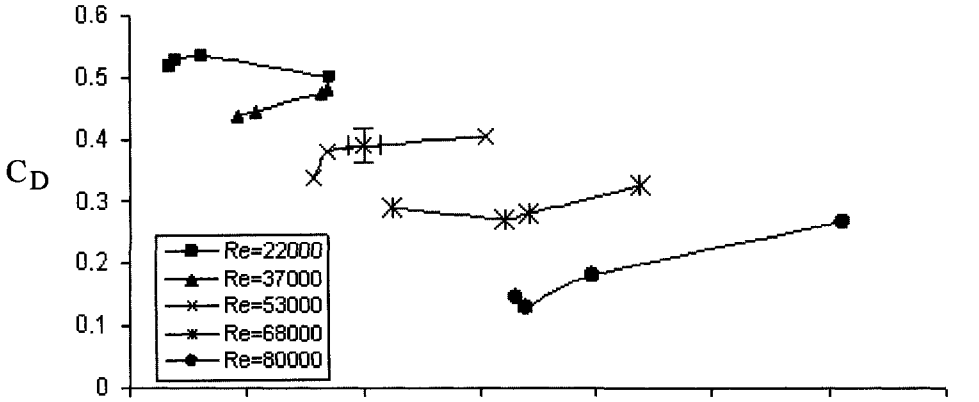

(b) Tu = 4%

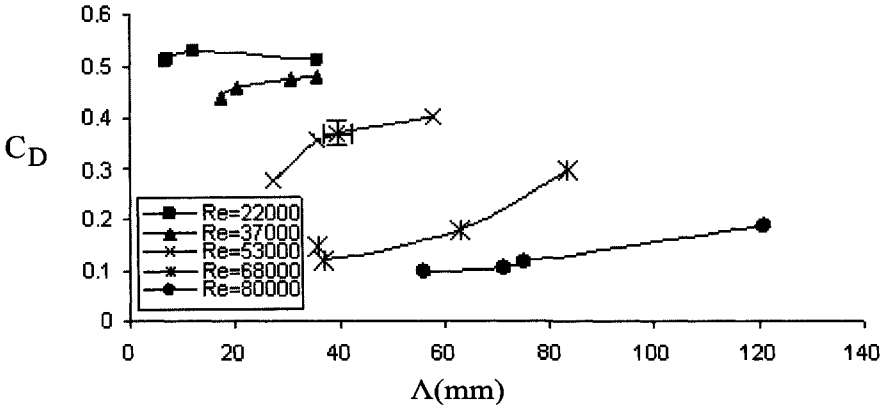

(c) Tu=6.3%

Figure 34: Impact of integral length scale on PVC sphere drag when (a) Tu = 2.5% (b) Tu = 4% (c) Tu = 6.3%

4.2.6 EFFECT OF REYNOLDS NUMBER

As illustrated in Figure 28, the variation of drag coefficient of a sphere versus Reynolds number in the standard curve over the range $1\times10^4 \leq Re \leq 3.5\times10^5$ is nearly constant. At the critical Reynolds number, $Re_{cr} = 3.5\times10^5$, C_D drops suddenly as a laminar boundary layer changes to a turbulent one, in the "smooth flow" case. Previous studies [Ahlborn, 1931; Brownlee, 1960; Torobin & Gauvin, 1960; Clamen & Gauvin, 1969; Bearman, 1971; Becker & Brown, 1974; Anderson, 1975; Anderson & Uhlherr, 1977] have shown that the value of the critical Reynolds number can be reduced with increasing freestream turbulence. It is known that higher turbulent level always leads to a lower critical Reynolds number [Dryden et al., 1937; Torobin & Gauvin, 1960; Clamen & Gauvin, 1969; Uhlherr & Sinclair, 1970].

Figure 35 portrays the C_D-Re relationships with fixed (Λ/d) and Tu for Experiment I (PVC spheres). The data correspond to a relative integral length scale of 0.7 (roughly medium value over the $0.1 \leq (\Lambda/d) \leq 2.6$ range considered in this study) clearly depicts that the decrease in the drag coefficient, with increasing Reynolds number, becomes progressively more significant as the turbulence intensity is augmented. Figure 36 shows the C_D-Re relationships with fixed (Λ/d) and Tu for Experiment II (wooden spheres). The data correspond to different relative integral length scales, 0.21~1.35. Similar to Figure 35, Figure 36 shows the decrease in the drag coefficient, with increasing Reynolds number. This decrease becomes progressively more significant at $(\Lambda/d) \approx 0.65$ and higher turbulence intensity.

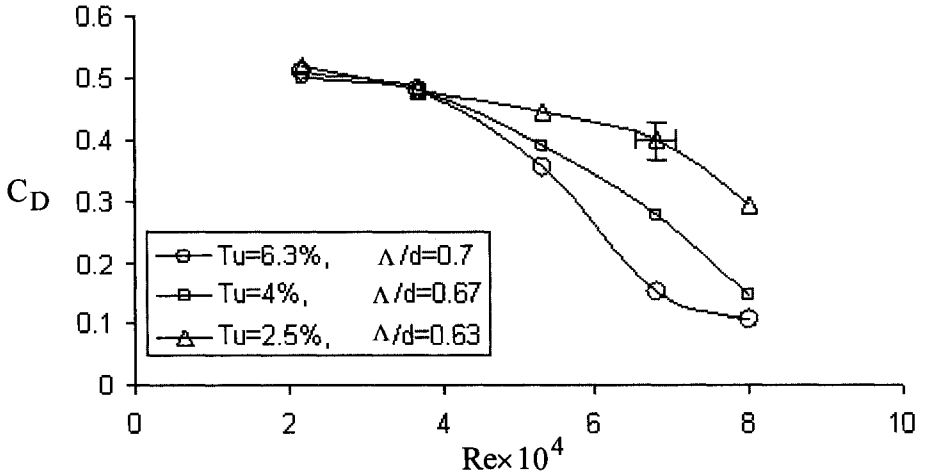

Figure 35: Impact of Reynolds number on PVC sphere drag

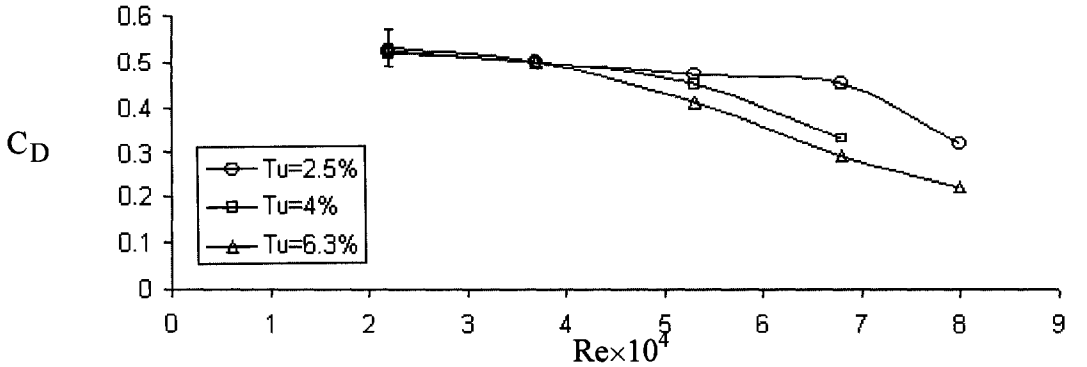

(a) $\Lambda/d \approx 0.22$ ($\Lambda/d = 0.21 \sim 0.26$)

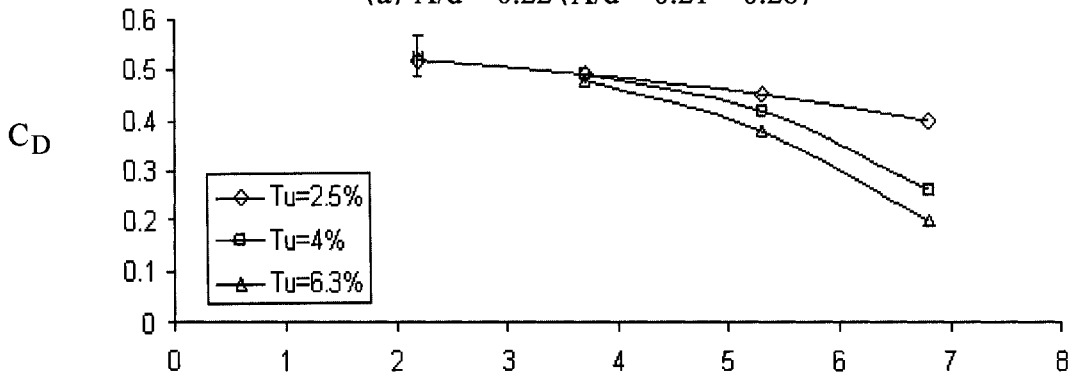

(b) $\Lambda/d \approx 0.33$ ($\Lambda/d = 0.3 \sim 0.35$)

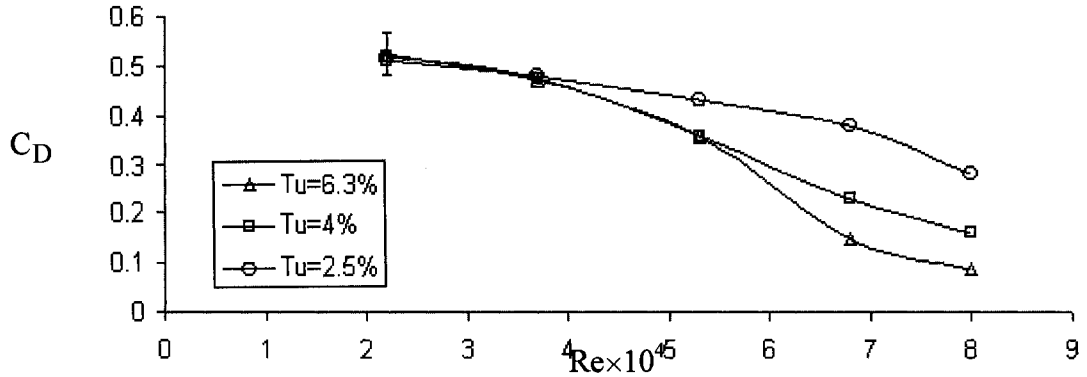

(c) $\Lambda/d \approx 0.65$ ($\Lambda/d = 0.6 \sim 0.7$)

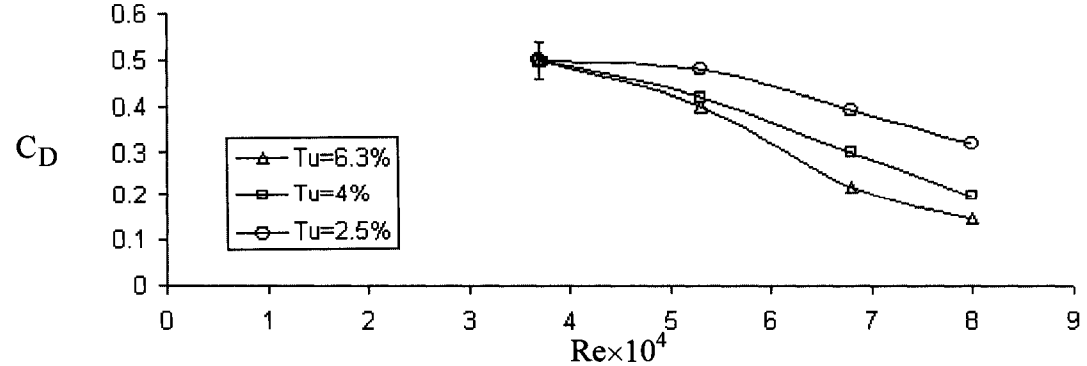

(d) $\Lambda/d \approx 1.2$ ($\Lambda/d = 1.12 \sim 1.35$)

Figure 36: Impact of Reynolds number on wooden sphere drag

CHAPTER 5: CONCLUSIONS AND RECOMMENDATIONS

The effects of turbulence intensity and integral length scale on the drag coefficient of a sphere were experimentally investigated in a closed circuit wind tunnel. The Reynolds number, $Re = Ud/\nu$, was varied from 2.2×10^4 to 8×10^4. The proper combination of orifice perforated plate hole diameter, sphere size, and sphere location enabled the independent alterations of turbulence intensity and relative integral length scale (Λ/d) for Experiment I, from 1.9% to 10% and from 0.1 to 2.6, respectively, and for Experiment II, from 2.5% to 6.3% and from 0.04 to 3.25, respectively at each studied Reynolds number.

5.1 CONCLUSIONS

In both experiments, current results have confirmed that the drag coefficient is decreased with increasing turbulence intensity, and the value of Re_{cr} at which C_D drops below 0.1 can be advanced when the freestream turbulence is intense. More interestingly, the unique role of the relative integral length scale is revealed. As showed in Experiment I, the drag can be reduced significantly by decreasing the integral length to around unity. This is particularly true when the level of turbulence is high. Also, as conclusion of the results of Experiment II, the drag coefficient of a sphere lessened by reducing the relative integral length scale until around 0.65 and then, increased by increasing the relative integral length scale above 0.65. In other words, increasing Λ/d up to 0.65 increases the effect of Tu on C_D and for Λ/d above 0.65, decreases this effect.

5.2 RECOMMENDATIONS FOR FUTURE WORKS

The sphere wake measurements by X-Probe, statistical analysis (like ANOVA) on various parameters on C_D and using more than one sphere and repeating the same experiments can be appropriate projects in future.

REFERENCES

Achenbach, E., 1972, "Experiments on the flow past spheres at very high Reynolds numbers," Journal of Fluid Mechanics, v 54, pp. 565-575.

Achenbach, E., 1974*a*, "Vortex shedding from spheres," Journal of Fluid Mechanics, v 62, pp. 209-221.

Achenbach, E., 1974*b*, "The effect of surface roughness and tunnel blockage on the flow past spheres," Journal of Fluid Mechanics, v 65, pp. 113–125.

Ahlborn, F., 1931, "Turbulence and mechanism of resistance on spheres and cylinders," Technical Physics, v 12, pp. 482-488.

Anderson, T., J., 1975, "Turbulence and drag," Thesis (Ph.D.), Monash University.

Anderson, T. J., Uhlherr, P. H. T., 1977, "The influence of stream turbulence on the drag of freely entrained spheres," *6th Australasian Hydraulics and Fluid Mechanics Conference Adelaide*, Australia.

Bacon, D. L., Reid, E. G., 1924, "The resistance of spheres in wind tunnels and in air," Report No. 185, National Advisory Committee for Aeronautics, United States National Advisory Committee for Aeronautics, 21p.

Bagchi, P., Balachandar, S., 2003, "Effect of turbulence on the drag and lift of a particle," Physics of Fluids, v 15, n 11, pp. 3496-3513.

Baki, V., Schmid, M., Stankovi, B., 2006, "Experimental investigation of turbulent structures of flow around a sphere," Thermal science, v 10, n 2, pp. 97-112.

Bakic, V., Peric, M., 2005, "Visualization of flow around sphere for Reynolds numbers between 22000 and 400000," Thermo physics and Aeromechanics, v 12, n 3, pp. 307-315.

Balachandar S., Bagchi, P., Wakaba, L., Zeng, L., 2004, "Particle turbulence interaction," XXI International Congress of Theoretical and Applied Mechanics, Warsaw, Poland.

Barton, N. G., 1982, "On the swing of a cricket ball in flight," Proceeding of the Royal Society of London A, v 379, pp. 109-131.

Batchelor, G. K., 1967, *An introduction to fluid dynamics*, Cambridge: Cambridge University Press, pp. 353-363.

Bearman, P. W., 1971, "An investigation of the forces on flat plates normal to a turbulent flow," Journal Fluid Mechanics, v 46, pp. 177-198.

Bearman, P. W., Harvey, J. K., 1976, "Golf ball aerodynamics," Aeronautical Quarterly, v 27, p 112.

Becker, H. A., Brown, A. P. G., 1974, "Response of pitot probes in turbulent streams," Journal Fluid Mechanics, v 62, pp. 85-114.

Birouk, M., Abou Al-Sood, M. M., 2007, "Numerical study of sphere drag coefficient in turbulent flow at low Reynolds number," Numerical Heat Transfer Part A, v 15, pp. 39-57.

Blackburn, H. M., 2002, "Mass and momentum transport from a sphere in steady and oscillatory flows," Physics of Fluids, v 14, p 3997.

Brownlee, K. A., 1960, *Statistical theory and methodology in science and engineering*, 2nd ed., John Wiley & Sons, New York.

Brucato, A., Grisafi, F., Montante, G., 1998, "Particle drag coefficients in turbulent fluids," Chemical Engineering Science, v 53, p 3295.

Choi, J., Jeon, W.-P., Choi, H., 2006, "Mechanism of drag reduction by dimples on a sphere," Physics of Fluids, v 18, n 4, pp. 41702-41714.

Chomaz, J. M., Bonneton, P., Hopfinger, E. J., 1993, "The structure of the near wake of a sphere moving horizontally in a stratified fluid," Journal of Fluid Mechanics, v 254, pp. 1-21.

Clamen, A., Gauvin, W. H., 1969, "Effects of turbulence on the drag coefficients of spheres in a supercritical flow regime," American Institute of Chemical Engineers (AIChE) Journal, v 15, pp. 184-189.

Clift, R., Gauvin, W. H., 1970, "The motion of particles in turbulent gas streams," *In: Chemeca 70: A conference convened by the Australian National Committee of the Institution of Chemical Engineers and the Australian Academy of Science. Chatswood,* Australia: Butterworths of Australia and the Institution of Chemical Engineers, pp. 14-28.

Clift, R., Gauvin, W. H., 1971, "Motion of entrained particles in gas streams," Canadian Journal of Chemical Engineering, v 49, pp. 439-448.

Constantinescu, G., Squires, K., 2004, "Numerical investigations of flow over a sphere in the subcritical and supercritical regimes," Physics of Fluids, v 16, n 5, pp. 1449-1466.

Dantec dynamics, "Streamline_streamware installation and users guide," Denmark, 2000.

Dryden, H. L., Schubauer, G. B., Mock, Jr. W. C., Skramstad H. K., 1937, "Measurements of intensity and scale of wind-tunnel turbulence and their relation to the critical Reynolds number of spheres," National Advisory Committee for Aeronautics – Reports 581, pp. 109-140.

Fage, A., 1937, "Experiments on a sphere at critical Reynolds numbers," Great Britain, Aeronautical Research Council, Reports and Memoranda, n 1766.

Howe, M. S., Lauchle, G. C., Wang, J., 2001, "Aerodynamic lift and drag fluctuations of a sphere," Journal Fluid Mechanics, v 436, pp. 41-57.

Hunt, T. M., Vaughan, N., 1996, *Hydraulic Handbook*, 9th Edition, Elsevier, p 8-A-2.

Kendall, J. M., 1964, "The periodic wake of a sphere," Propulsion Laboratory, California Institute Technology, Space Programs Summary No. 37-25, v. 4, p 251.

Kim, D., Choi, H., 2002, "Laminar flow past a sphere rotating in the streamwise direction," Journal Fluid Mechanics, v 461, pp. 365-386.

Kim, H. J., Durbin, P. A., 1988, "Observations of the frequencies in a sphere wake and of drag increase by acoustic excitation," Physics of Fluids, v 31, n 11, pp. 3260-3265.

Jenson, V. G., 1959, "Viscous flow around a sphere at low Reynolds numbers (< 40)," Proceedings Royal Society of London A, v 249, pp. 346-366.

Jeon, S., Choi, J., Jeon, W.-P., Choi, H., Park, J., 2004, "Active control of flow over a sphere for drag reduction at a sub-critical Reynolds number," Journal Fluid Mechanics, v 517, p 113-129.

Lamb, H., 1945, *Hydrodynamics*, 6th ed., Dover Publications, New York, p 609.

Lapple, C. E., Shepherd, C. B., 1940, "Flow pattern and pressure drop in cyclone dust collectors," Journal of Industrial and Engineering Chemistry, v 32, pp. 1246-1248.

Lee, S. L., 1987, "Particle drag in a dilute turbulent two-phase suspension flow," International Journal Multiphase Flow, v 13, pp. 247-256.

Lee, S., 2000, "A numerical study of the unsteady wake behind a sphere in a uniform flow at moderate Reynolds numbers," Computers & Fluids, v 29, pp. 639-667.

Lemmin, U., Schurter, M., Imboden, D. M., Joller, Th., 1985, "An instrument for measuring small currents in lakes," The American Society of Limnology and Oceanography, pp. 1116-1122.

Liu, R., Ting, D. S-K., Rankin, G. W., 2004, "On the generation of turbulence with a perforated plate," Experimental Thermal Fluid Science, v 28, pp. 307-316.

Liu, R., Ting, D. S-K., Checkel, M. D., 2007, "Constant Reynolds number turbulence downstream of an orificed perforated plate," Experimental Thermal and Fluid Science, v 31, pp. 897-908.

Liu, R., Ting, D. S-K., 2007, "Turbulent flow downstream of a perforated plate: Sharp-Edged orifice versus finite-thickness holes," Journal of Fluids Engineering, v 129, pp. 1164-1171.

Lyotard, N., Shew, W. L., Bocquet, L., Pinton, J.-F., 2007, "Polymer and surface roughness effects on the drag crisis for falling spheres," European Physical Journal B, v 60, n 4, pp. 469-476.

Magarvey, R. H., Maclatchy, C. S., 1964, "Formation and structure of vortex rings," Canadian Journal of Physics, v 42, pp. 678-683.

Mittal, R., 1999, "A Fourier Chebyshev spectral collocation method for simulation flow past spheres and spheroids," International Journal for Numerical Methods in Fluids, v 30, pp. 921-937.

Neve, R. S., 1986, "The importance of turbulence macroscale in determining the drag coefficient of spheres," International Journal of Heat and Fluid Flow, v 7, pp. 28-36

Neve, R. S., Shansonga, T., 1989, "The effects of turbulence characteristics on sphere drag," International Journal of Heat and Fluid Flow, v 10, pp. 318-321.

Ormieres, D., Provansal, M., 1999, "Transition to turbulence in the wake of a sphere," Physical Review Letters, v 83, n 1, pp. 80-83.

Phoreman, J., Saephan, S., Vander Kam, J. C., accessed in 2007, "Determination of turbulence level in the UC Davis Aeronautical Wind Tunnel," http://windtunnel.engr.ucdavis.edu/research/spheres/spherereport.pdf.

Petrak, D., 1976, "Experimental investigation of motion of free non-Stokes particles flow," Zeitschrift fur Angewandte Mathematik und Mechanik, v 56, n 10, pp. 457-461.

Prandtl, L., 1914, "Der Luftmiderstand von Kugeln," Nachr. d. K. Ges. d. Wiesenaoh., Göttingen Mathematisch-Physikalische Klasse, pp. 177-190.

Sakamoto, H., Haniu, H., 1990, "A study on vortex shedding from spheres in a uniform flow," Journal of Fluids Engineering, v 112, n 4, pp. 386-392.

Sankagiri, N., Ruff, G. A., 1997, "Measurement of sphere drag in high turbulent intensity flows," American Society of Mechanical Engineers, Fluids Engineering Division (Publication) FED, ASME_Fluids Engineering Division, v 244, pp. 277-282.

Schlichting, H., 1955, "Simple method for calculation of frictionless incompressible flow through cascade relating to "direct problem" of cascade theory in which aerodynamic parameters and pressure distribution along blade are determined," Verein Deutscher Ingenieure -- VDI Zeitschrift, n 9, pp. 269-270.

Schlichting, H., 1979, *Boundary layer theory*, McGraw-Hill, Antigua, p 17, Chap 1.

Scoggins, J. R., 1967, "Sphere behavior and the measurement of wind profiles," National Aeronautics and Space Administration (NASA-TN-D-3994), 61p.

Sivier, K. R., Nicholls, J. A., 1969, "Subsonic sphere drag measurements at intermediate Reynolds numbers," National Advisory Committee for Aeronautics, Contractor Reports, n 1392, 68p.

StrainSense Ltd., accessed in 2007, http://www.strainsense.co.uk/products/ELG-Ultra-low-force-sensor/172, sales@strainsense.co.uk.

Taneda, S., 1956, "Studies of wake vortices (111), experimental investigation of the wake behind a sphere at low Reynolds numbers," Report. Research Institute of Applied Mechanics of Japan, v 4, pp. 99-105.

Taneda, S., 1978, "Visual observations of the flow past a sphere at Reynolds numbers between 10^4 and 10^6," Journal of Fluid Mechanics, v 85, pp. 187-192.

Taylor, G. I., 1937, "Statistical theory of isotropic turbulence," Journal of the Aeronautical Sciences, v 4, n 8, pp. 311-315.

Taylor, G. I, 1938, "The spectrum of turbulence," Proceedings of the Royal Society London, ser. A164, pp. 476-490.

Torobin, L. B., Gauvin, W. H., 1959, "Fundamental aspects of solids-gas flow, Part II: The sphere wake in steady laminar fluids," Canadian Journal of Chemical Engineering, v 37, pp. 167-176.

Torobin, L. B., Gauvin, W. H., 1960, "Fundamental aspects of solids-gas flow, Part V: The effects of fluid turbulence on the particle drag coefficient," Canadian Journal of Chemical Engineering, v 38, 1960, pp. 189-200.

Torobin, L. B., Gauvin, W. H., 1961, "The drag coefficients of single spheres moving in a steady and accelerated motion in a turbulent fluid," American Institute of Chemical Engineers (AIChE) Journal, v 7, p 615-619.

Tyagi, H., Liu, R., Ting, D., Johnston, C. R., 2006, "Measurement of wake properties of a sphere in freestream turbulence," Experimental Thermal and Fluid Science, v 30, pp. 587-604.

Uhlherr, P. H. T., Sinclair, C. G., 1970, "The effect of free-stream turbulence on the drag coefficient of spheres," Proceedings of CHEMCA' 70, Butterworth of Australia and Institution of Chemical Engineers, Melbourne, Australia, pp. 1-13.

Warnica, W. D., Renksizbulut, M., Strong, A. B., 1995, "Drag coefficients of spherical liquid droplets, Part 2: Turbulent Gaseous Fields," Experiments in Fluids, v 18, pp. 265-276.

Westerman, J., Sharcos, E., 1966, "Din 140 : 1304 standard," pp.160-200.

White, J. E., 1966, "Static friction as source of seismic attenuation," Geophysics, v 31, n 2, pp. 333-339

Willmarth, W. W., Enlow, R. L., 1969, "Aerodynamic lift and moment fluctuations of a sphere," Journal Fluid Mechanics, v 36, pp. 417-432.

Winny, H. F., 1932, "The vortex system generated behind a sphere moving through a viscous fluid," Aeronautical Research Council Reports and Memoranda No. 1531, pp. 183-197.

Yun, G., Choi, H., Kim, D., 2003, "Turbulent flow past a sphere at Re = 3700 and 10^4," Physics of Fluids, v 15, p S6.

Yusof, J., 1996, ''Interaction of massive particles with turbulence,'' Ph.D. thesis, Department of Mechanical Engineering, Cornell University.

Zarin, N. A., 1970, "Measurement of non-Continuum and turbulence effects on subsonic sphere drag," National Aeronautics and Space Administration (NASA), Report, CR-1586, 137p.

Zarin, N. A., Nicholls, J. A., 1971, "Sphere drag in solid rockets—non-Continuum and turbulence effects," Combustion Science and Technology, v 3, n 6, pp. 273-285.

APPENDIX A: SELECTING SAMPLING FREQUENCY AND NUMBER

The minimum required sampling number N associated with sampling frequency f_s is determined by examining the convergence of the flow parameters, i.e. the time-averaged velocity $(\overline{U})$, the turbulence fluctuation velocities (u) and the integral length scale (Λ), as a function of sampling number. Using three different perforated plates generates three turbulent flow conditions in the experiment. The minimum downstream distance from the plates is 10D within which range the flow is much more turbulent [Liu et al., 2007]. Thus, the time-averaged velocity $(\overline{U})$, the turbulence fluctuation velocity (u) and the integral length scale (Λ) are found for different sampling numbers covering the range of 900-10^7, with f_s = 80 kHz at 10D downstream of the orificed perforated plate. MATLAB Programs are developed for this purpose, with code presented in Appendix C.

Figures A.1, A.2 and A.3 show the variations of the time-average flow velocity, turbulent velocity and integral length scale versus sampling number for 1D hot-wire measurement. Results show that once the sampling number is larger than 7×10^6, sufficient accuracy can be achieved. A sampling number of 10^7 was used for the current set of hot-wire measurements.

Figures A.4, A.5 and A.6 show the variations of the time-average flow velocity, turbulent velocity and integral length scale versus sampling number for X-probe hot-wire measurement.

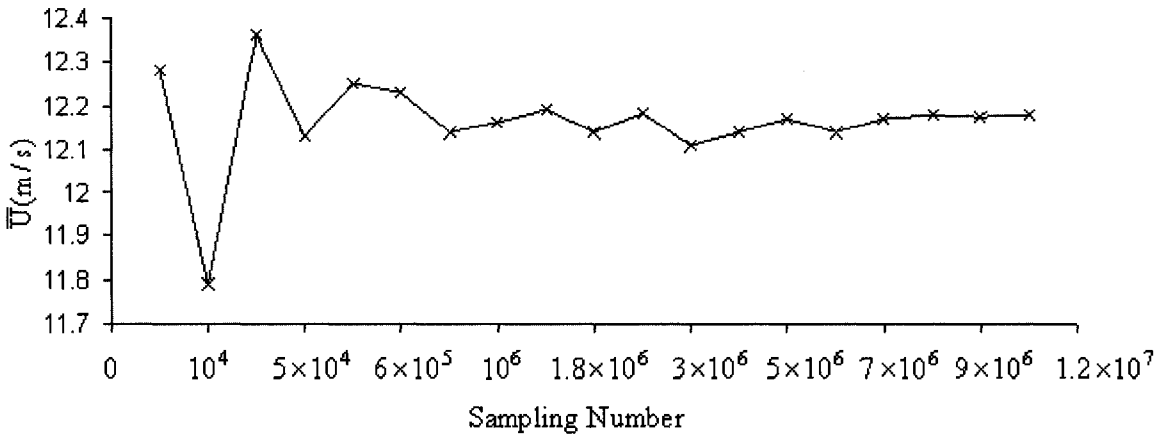

(a) Plate A (D = 25 mm)

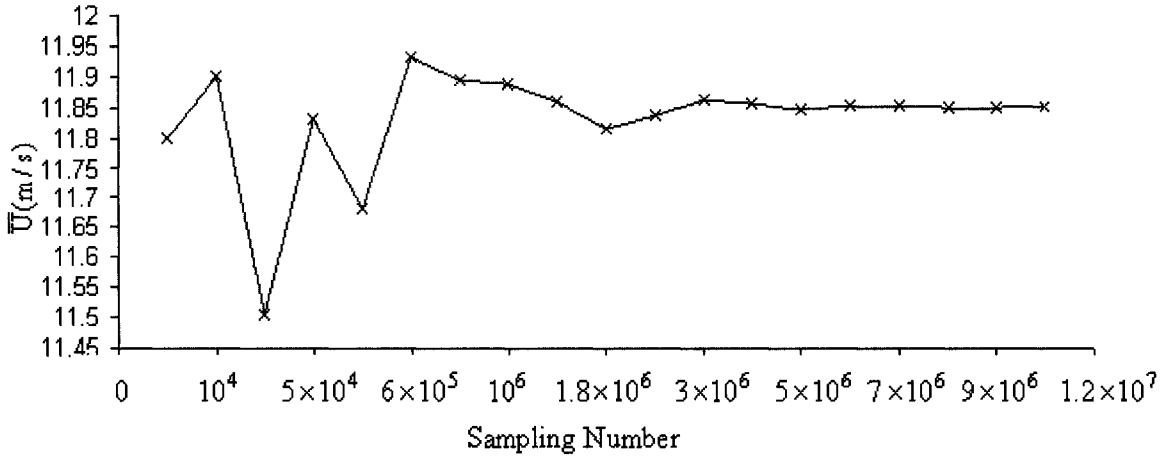

(b) Plate B (D = 37.5 mm)

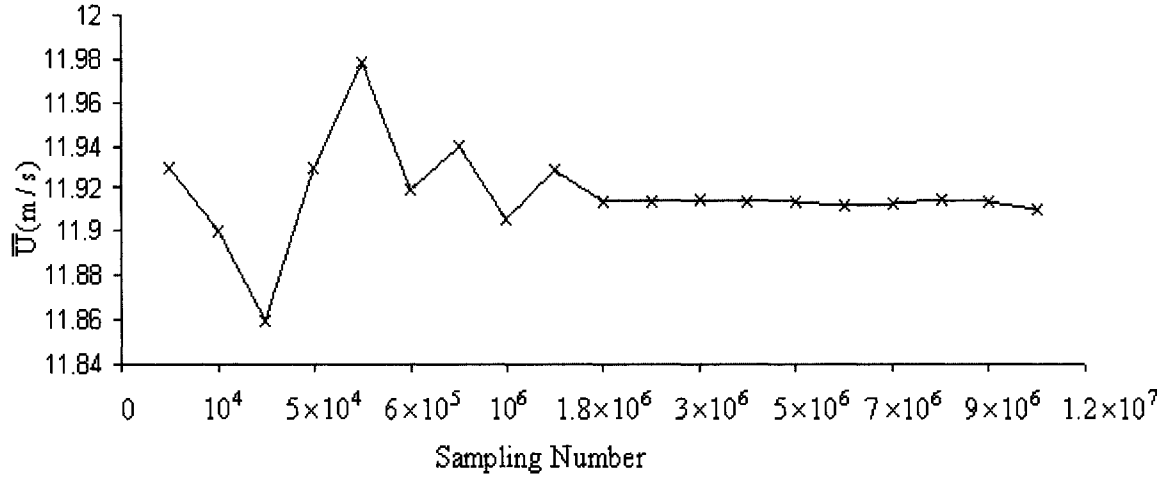

(c) Plate C (D = 50 mm)

Figure A.1: Minimum required sampling number for $\overline{U}$ at U ≈ 12 m/s, f_s = 80 kHz (1D-Probe).

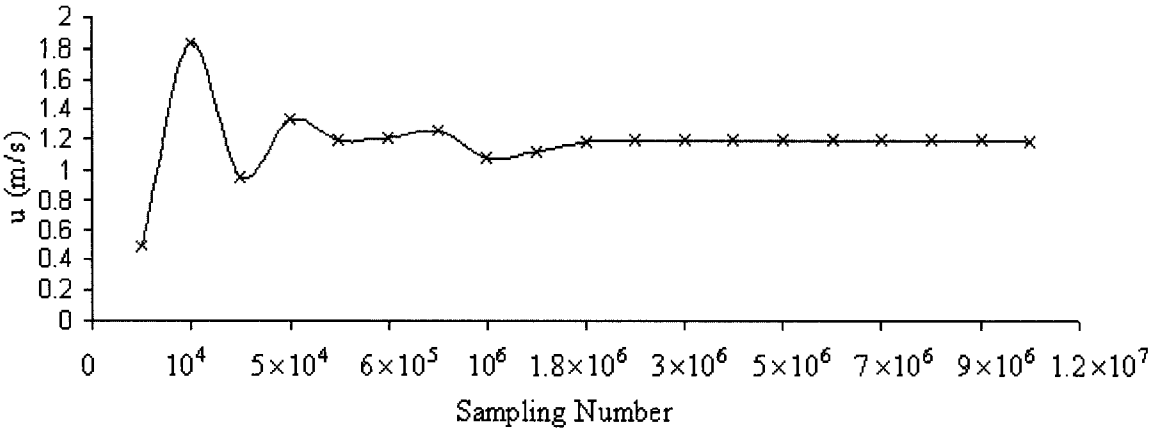

(a) Plate A (D = 25 mm)

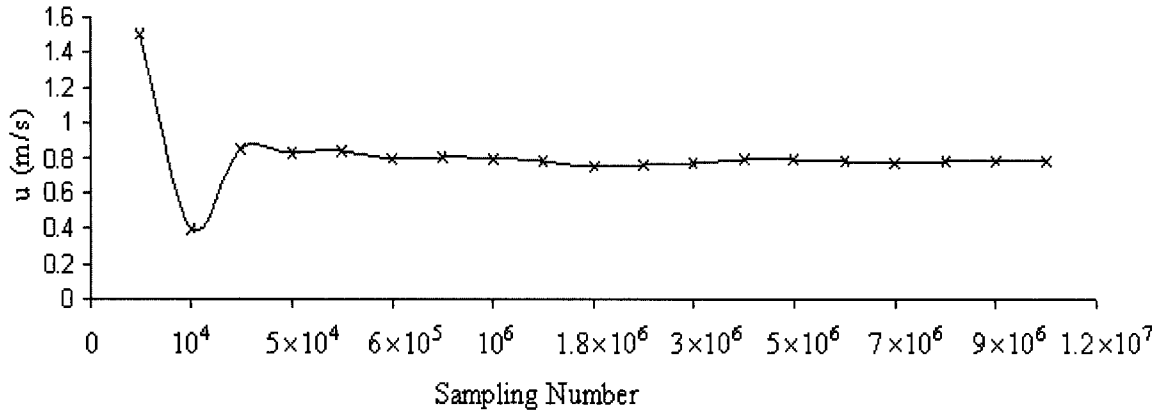

(b) Plate B (D = 37.5 mm)

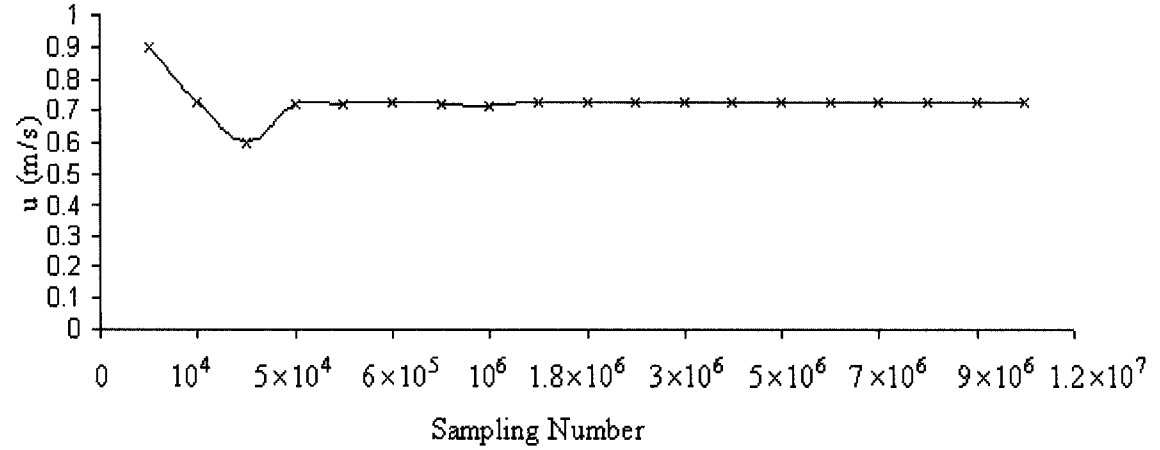

(c) Plate C (D = 50 mm)

Figure A.2: Minimum required sampling number for u at U ≈ 12 m/s, f_s = 80 kHz (1D-Probe).

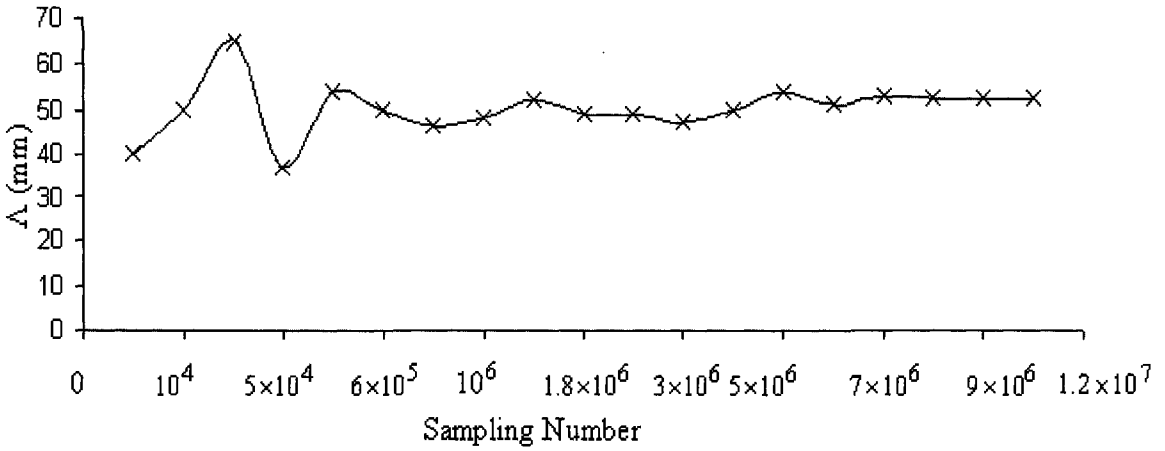

(a) Plate A (D = 25 mm)

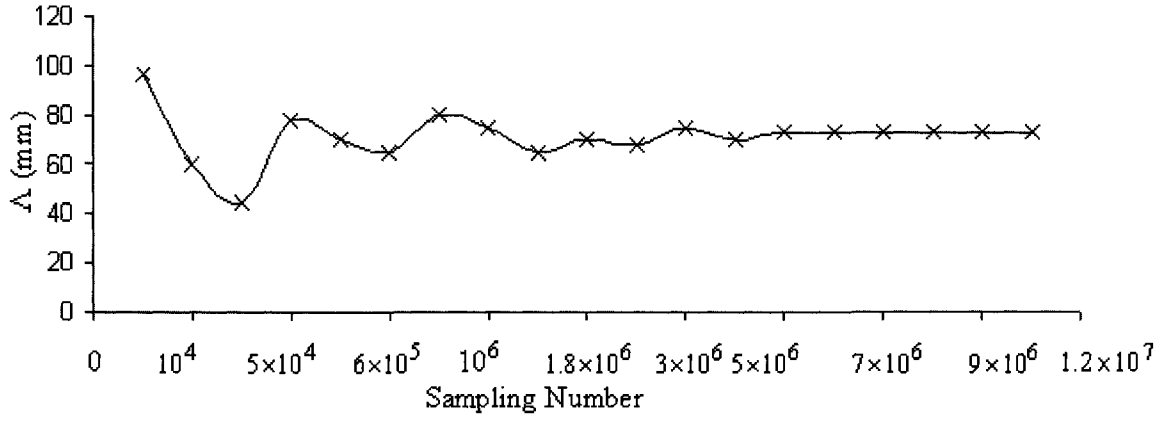

(b) Plate B (D = 37.5 mm)

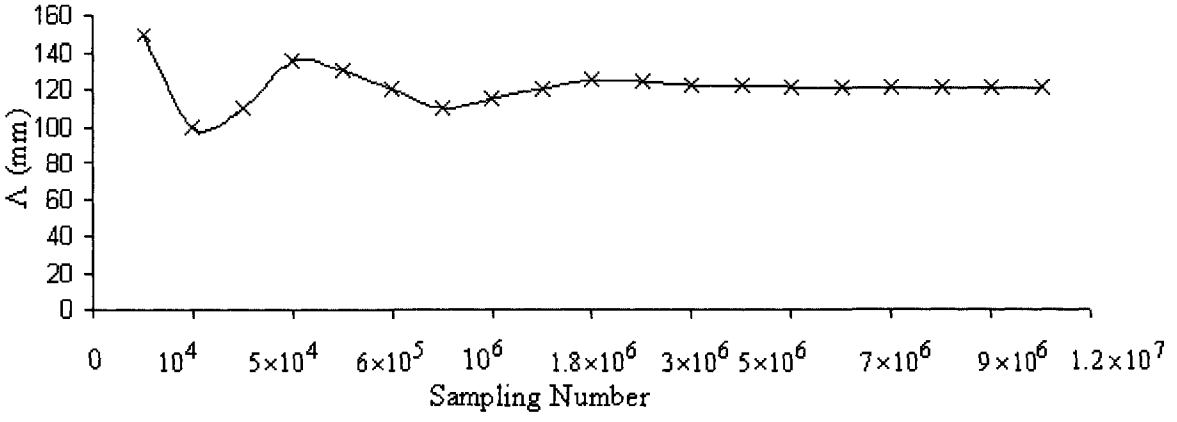

(c) Plate C (D = 50 mm)

Figure A.3: Minimum required sampling number for Λ at U ≈ 12 m/s, f_s = 80 kHz (1D-Probe).

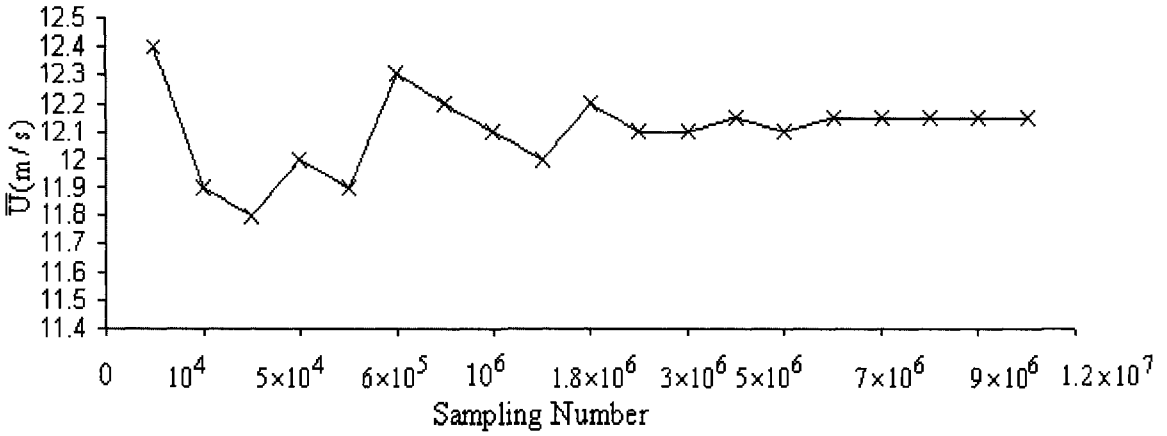

(a) Plate A (D = 25 mm)

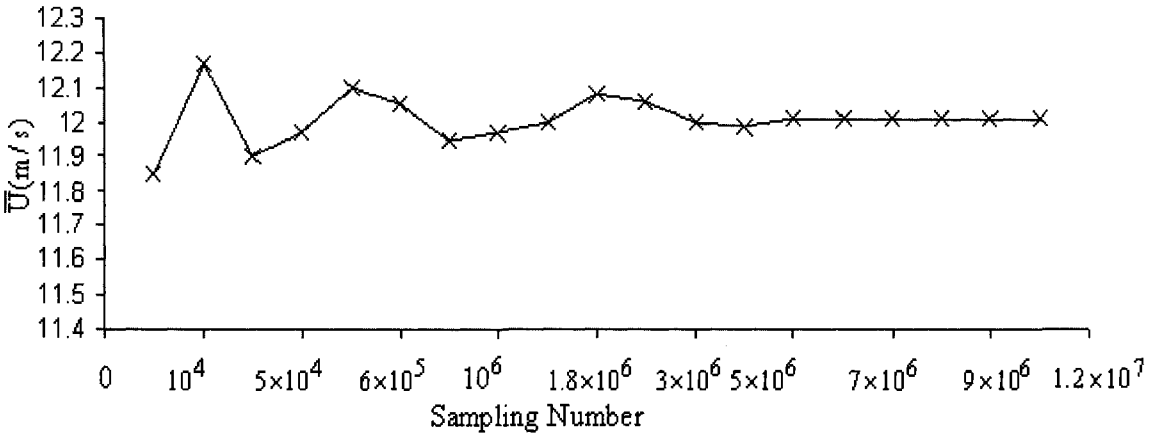

(b) Plate B (D = 37.5 mm)

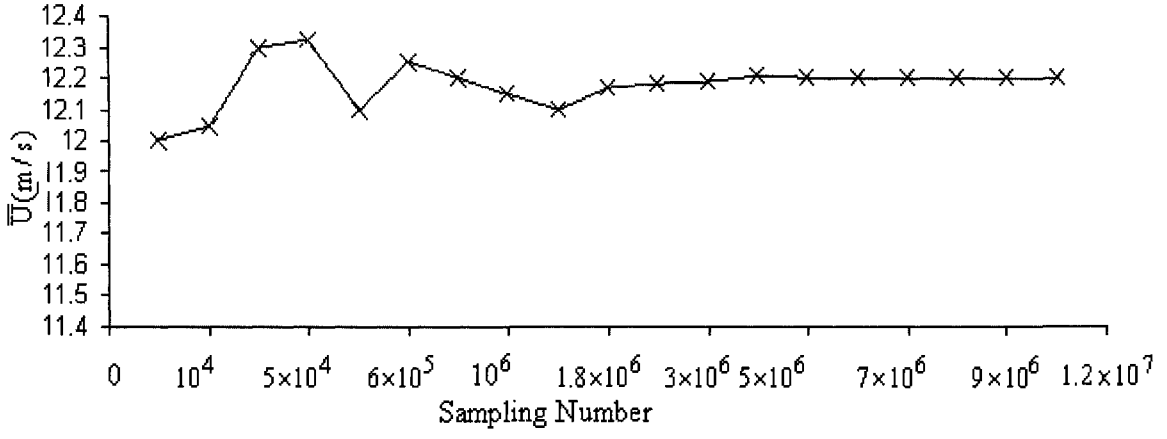

(c) Plate C (D = 50 mm)

Figure A.4: Minimum required sampling number for $\overline{U}$ at $U \approx 12.1$ m/s, $f_s = 80$ kHz (X-Probe).

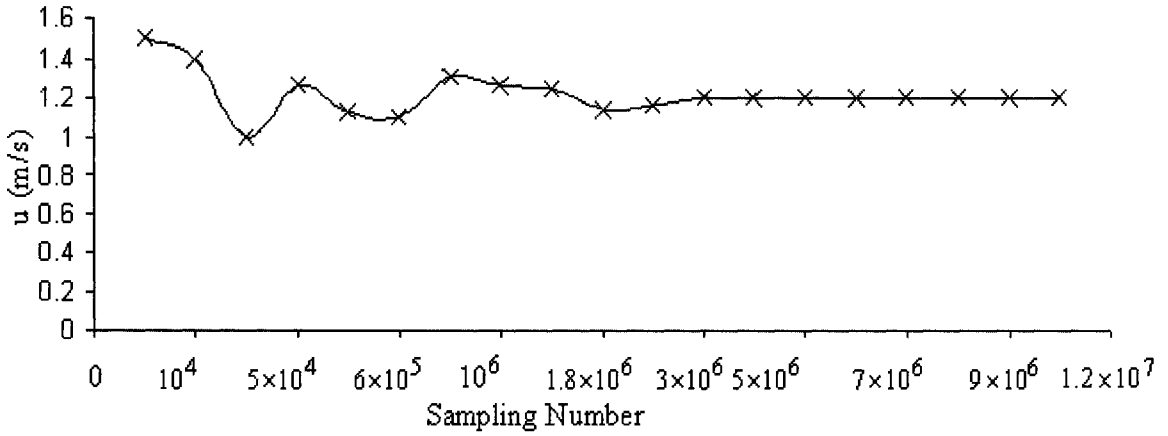

(a) Plate A (D = 25 mm)

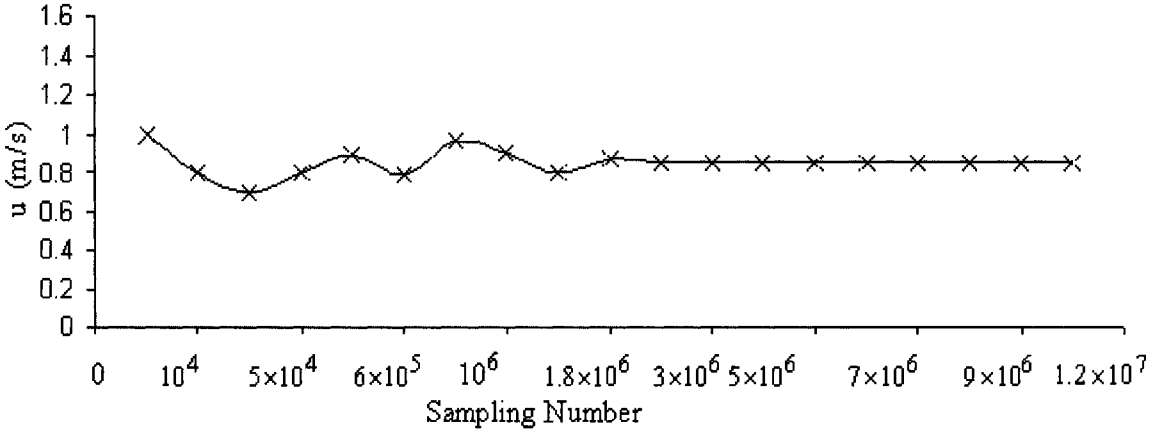

(b) Plate B (D = 37.5 mm)

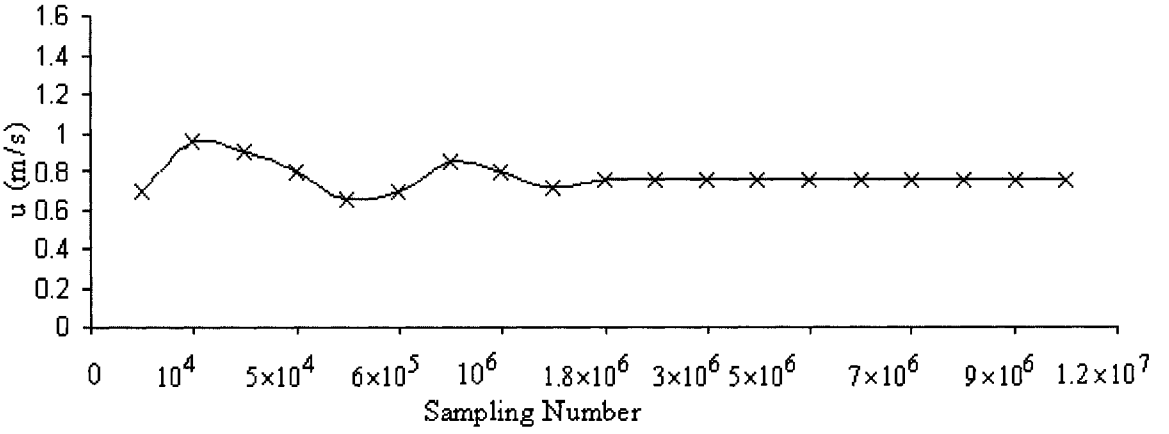

(c) Plate C (D = 50 mm)

Figure A.5: Minimum required sampling number for u at U ≈ 12.1 m/s, f_s = 80 kHz (X-Probe).

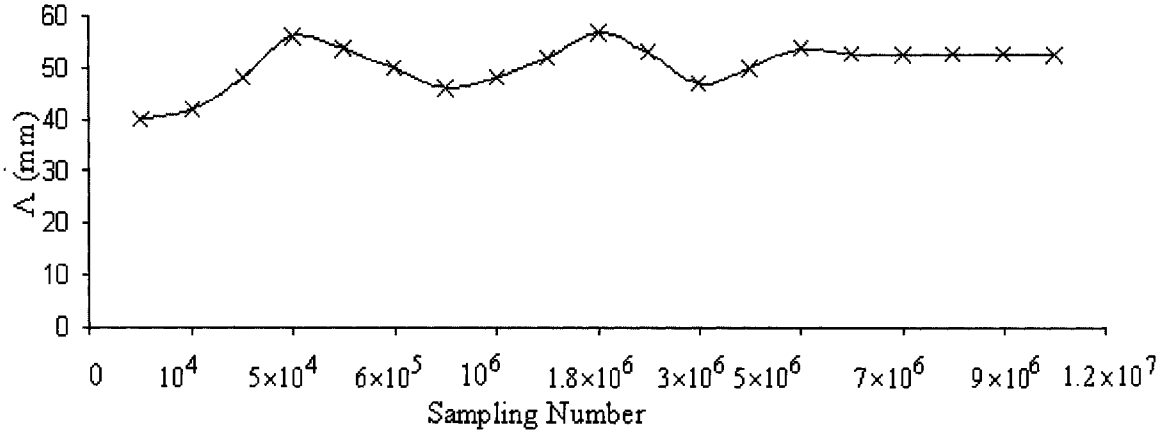

(a) Plate A (D = 25 mm)

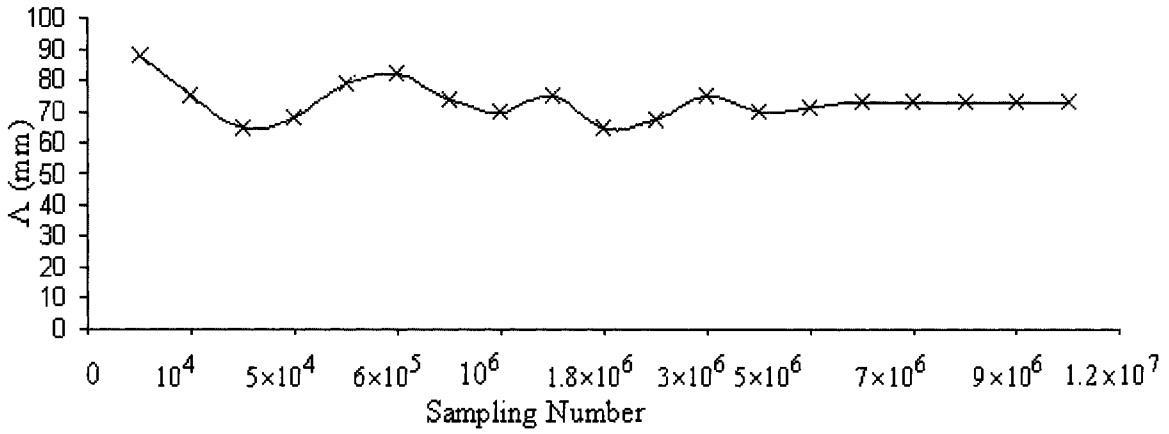

(b) Plate B (D = 37.5 mm)

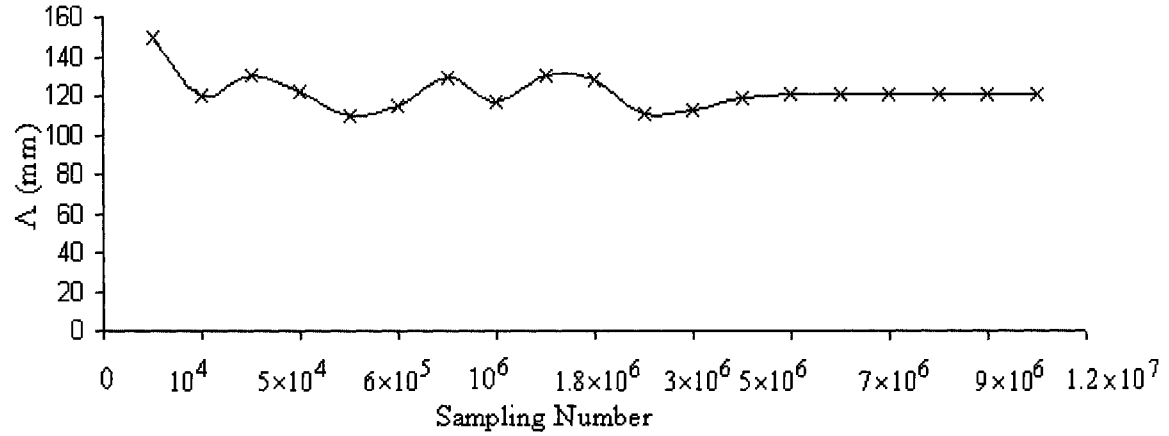

(c) Plate C (D = 50 mm)

Figure A.6: Minimum required sampling number for Λ at U ≈ 12.1 m/s, f_s = 80 kHz (X-Probe).

REFERENCES

Liu, R., Ting, D. S-K., Checkel, M. D., 2007, "Constant Reynolds number turbulence downstream of an orificed perforated plate," Experimental Thermal and Fluid Science, v 31, pp. 897-908.

APPENDIX B: ANALYSIS OF HOT-WIRE DATA

B.1 GENERAL EQUATIONS AND EXPLANATIONS FOR THE ANALYSIS OF HOT-WIRE DATA:

A hot-wire system is used for measuring flow velocity. The mean and turbulent velocities can be found from achieved voltage data by a MATLAB program as presented in Appendix C. Then, all other turbulence parameters, such as turbulence intensity and integral length scale, can be calculated based on them. The calculated data depends on two main parameters, the flow velocity $\tilde{V}$ and flow direction represented by the yaw angle α. The yaw angle is an angle between the flow direction and the perpendicular direction of the wire.

To explain how the mean and turbulent flow velocities are determined from the hot-wire data (voltage), the geometrical relation between the direction of the wire and flow velocity are shown in Figure B.1. Denote the flow velocity as $\tilde{V}$, the velocity components in the directions along and perpendicular to the hot-wire as U_T and U_N, respectively; see Figure B.1(a). Also, the flow can be mentioned and considered by its components in the x, y directions as U and V, which are the most familiar directions; see Figure B.1(b). As shown in the Figure B.1(b), the angle between $\tilde{V}$ and x direction is defined as θ.

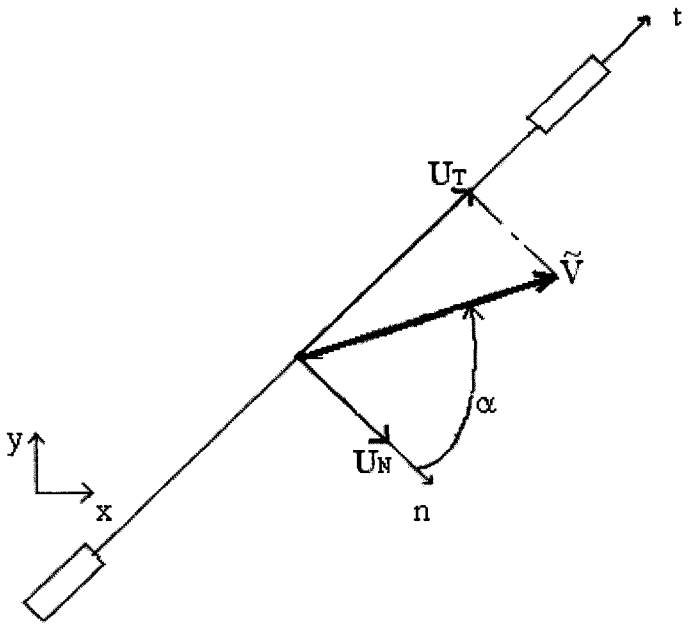

(a) T-N components

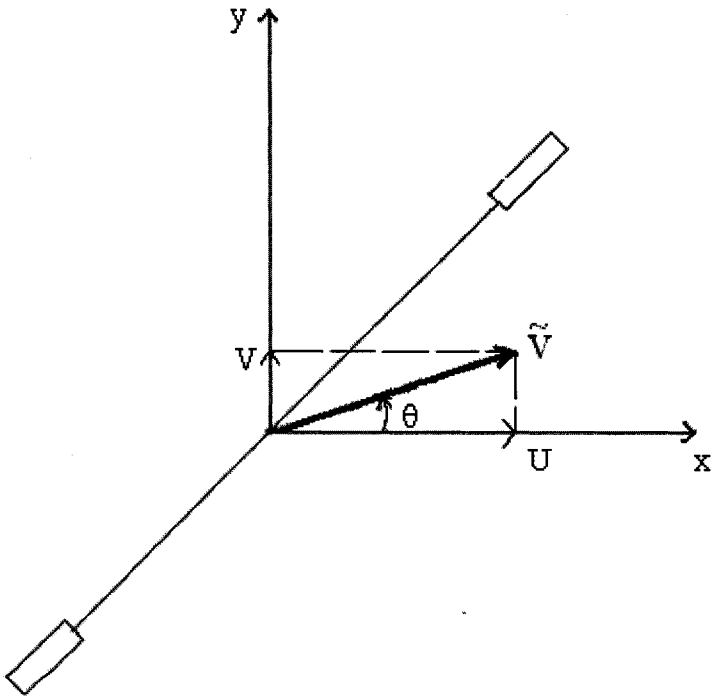

(b) X-Y components

Figure B.1: Schematic of flow velocity and hot-wire

It is clear from the above explanation, the voltage data achieved by hot-wire is a function of the flow velocity and flow direction when the density of flow, ρ, is a constant.

$$E = f(\tilde{V}, \alpha) \tag{B.1}$$

To make considering the voltage data easier, it will be considered as a function of effective velocity V_e where the effective velocity, V_e, is defined by

$$V_e = f(\tilde{V}, \alpha) \tag{B.2}$$

The power law defines the relation between the voltage data and the effective velocity as follows:

$$E^2 = A + BV_e^n \tag{B.3}$$

where A, B and n will be determined from the calibration data.

The effective velocity can be defined based on the normal and tangential components of the flow velocity by

$$V_e^2 = U_N^2 + k^2 U_T^2 \tag{B.4}$$

Where U_N is the normal component of $\tilde{V}$, U_T is the tangential component of $\tilde{V}$, k is a coefficient which is a function of yaw angle α.

Bradshaw [1971] and Bruun [1972] did several experiments to find the relation between k and α. They defined

$$k = f(\alpha) \tag{B.5}$$

where $f(\alpha) = \cos\bar{\alpha}_e$, $\bar{\alpha}_e$ is the effective yaw angle. In fact, each wire in a hot-wire has a particular yaw angle α. All of their effects can be considered as the effect of one 'effective yaw angle', $\bar{\alpha}_e$. In the case of 1D hot-wire used in Experiment I, there is only one wire. Thus, $\bar{\alpha}_e$ equals to α. But, for the 2D hot-wire used in Experiment II, there are two wires and thus a specific relation between $\bar{\alpha}_e$ and α.

On the other hand, Bradshaw [1971] defined the following equation to find the effective angle,

$$\cos\theta - E_\theta = \tan\bar{\alpha}_e(\sin\theta) \tag{B.6}$$

There is only one problem in the above process. In the static calibration, k^2 will be found which can give a positive or negative k, but to recognize when k is the negative, a

dynamic calibration is done which gives the ratio of voltage to velocity ($\frac{E}{U}$ or $\frac{E}{V}$) and it gives k.

B.2 CALIBRATION OF HOT-WIRE

B.2.1 1D-PROBE:

1- To calibrate the 1D hot-wire probe, the probe is installed near the exit of a jet. The hot-wire system gives the voltage data at 15 different velocities. These data will be converted to original values of voltages by considering the input gain and offset values on them. Then, a curve relates the original voltage value and the corresponding velocity can be plotted. An equation is achieved from the data which all velocities give the voltages equal to original one by an error less than 1%. Also, the system gives 5 coefficients, C_0, C_1, C_2, C_3, and C_4 to find the correct voltage values,

$$E = C_0 + C_1E^1 + C_2E^2 + C_3E^3 + C_4E^4 \qquad (B.7)$$

2- For 1D-Probe, no calibration for yaw angle is required. It is always constant and equal to 0°. Equation B.6 shows the maximum value for k ($= \cos\overline{\alpha}_e = \cos\alpha$) is one. Thus, α should be zero.

B.2.2 X-PROBE

1- Calibrating the 2D hot-wire probe was with automatic system. The probe is installed near the exit of a jet. For each wire, the hot-wire system gives the voltage data at 15 different velocities adjusted automatically by the calibrator. The temperature effect and gain and offset values are adjusted automatically, too. Then, a curve relates the original voltage value and the corresponding velocity can be plotted. An equation is achieved which all velocities give the voltages equal to original one by an error less than 1%. In Experiment II, this error was less than 0.4%. The system gives 5 coefficients to find the correct voltage values for each wire, C_{01}, C_{11}, C_{21}, C_{31}, and C_{41} for the first wire and C_{02}, C_{12}, C_{22}, C_{32}, and C_{42} for the second one.

$$E_1 = C_{01} + C_{11}E_1 + C_{21}E_1^{\,2} + C_{31}E_1^{\,3} + C_{41}E_1^{\,4} \quad \text{(B.8)}$$

$$E_2 = C_{02} + C_{12}E_2 + C_{22}E_2^{\,2} + C_{32}E_2^{\,3} + C_{42}E_2^{\,4} \quad \text{(B.9)}$$

2- For yaw angle calibration, the process for wire 1 and wire 2 are the same. For a particular velocity which was selected as 8 m/s in the current calibration, the voltage data will be given by hot-wire system in 11 different angles from -20° to +20°. The effects of temperature and the gain and offset values are automatically considered by the automatic system. Correction coefficients found in the calibration with the original values of voltage give the correct values of voltages in each angle,

$$E'_1 = C_{01} + C_{11}E'_1 + C_{21}E'^{\,2}_1 + C_{31}E'^{\,3}_1 + C_{41}E'^{\,4}_1 \quad \text{(B.10)}$$

$$E'_2 = C_{02} + C_{12}E'_2 + C_{22}E'^{\,2}_2 + C_{32}E'^{\,3}_2 + C_{42}E'^{\,4}_2 \quad \text{(B.11)}$$

Then, the relative values of E'_1/U and E'_2/U are calculated.

Finally, the slope of the plots of $[\cos(\theta) - (E'_1/U)]$ and $[\cos(\theta) - (E'_2/U)]$ versus $\sin(\theta)$ gives the effective yaw angle of the two wires.

B.3 ANALYSIS OF HOT-WIRE:

B.3.1 1D-PROBE DATA:

To find the time averaged velocity, root mean square velocity and other turbulence parameters such as turbulence intensity, integral length scale, etc, a MATLAB program is developed to process the collected data as presented in Appendix C.

a) Temperature of hot-wire:

During the calibration, the ambient temperature of the lab, T_a, will be registered. The experiment should be done right after calibration at the same temperature. The uncertainties included the error of the temperature variation during the experiment.

The ambient temperature of the lab has important effect on the temperature of the hot-wire, which would affect the current and resistant of the wire. The following equation is proposed by Laufer [1954] to find the hot-wire temperature:

$$x_w = x_0[1 + \alpha_0(T_w - T_0) + \beta_0(T_w - T_0)^2] \quad \text{(B.12)}$$

where T_w is the temperature of the wire, T_0 is the temperature of the wire when the ambient temperature is 0°C ($T_0 = T_a = 0°C$), x_w and x_0 are the resistant of wire per unit length and per unit cross-sectional area of the wire at temperature T_w and T_0, respectively, and α_0 and β_0 are temperature coefficients at 0°C.

The hot-wire anemometry book [Bruun, 1996] suggests to use the following equation to find x:

$$R = \frac{xl}{A_w} \tag{B.13}$$

where R is the total resistant, l is the length of the wire, A_w is the cross-sectional area of the wire and x is the resistant of wire per unit length and per unit cross-sectional area of the wire.

Also, Equation (B.12) can be simplified as follows without sacrificing too much accuracy:

$$x_w = x_0[1 + \alpha_0(T_w - T_0)] \tag{B.14}$$

On the other hand,

$$R_w = \int_{-1/2}^{1/2} \frac{x_w}{A_w} dl \tag{B.15}$$

where R_w is the total resistant at the wire temperature, T_w.

By substituting Equation B.13 and B.14 into B.15,

$$R_w = R_0[1 + \alpha_0(T_w - T_0)] \tag{B.16}$$

where R_w and R_0 are the total resistant T_w and T_0, respectively.

But, in the manuals B.1 [Bradshaw, 1971], these data are all corresponding to the temperature of 20°C. Thus,

$$R_w = R_{20}[1 + \alpha_{20}(T_w - T_{20})] \tag{B.17}$$

where

$$\alpha_{20} = \frac{R_0}{R_{20}}\alpha_0 \tag{B.18}$$

In general situation, the temperature coefficient at the reference temperature, α_{ref}, can be defined from Equation B.18 when the ambient temperature is T_a during the calibration:

$$\alpha_{ref} = \frac{R_{20}}{R_a}\alpha_{20} \tag{B.19}$$

By substituting Equations B.17 and B.18 into Equation B.19, the following relation for α_{ref} can be found:

$$\alpha_{ref} = \frac{R_w}{[1+\alpha_{20}(T_w - T_{20})]R_a}\alpha_{20} \tag{B.20}$$

On the other hand, the voltage achieved during the data acquisition should be corrected due temperature variations during the experiment. If the temperature is T_1 at the beginning of the data acquisition and T_{actual} when the data is registered, then, the corrected voltage can found by:

$$\text{volt_corrected} = \text{volt_actual}*((T_w - T_1)/(T_w - T_{actual})).\text{^}(0.5*(1+m)) \tag{B.21}$$

$$[m = -0.2 \text{ for } T_{actual} > T_1 \text{ and } m = 0.2 \text{ for } T_{actual} < T_1]$$

T_{actual} is achieved from the data and temperature probe setup.

b) U_{mean}, u_{rms} and Tu

Each instantaneous flow velocity U_i is determined based on the corrected voltage E_c, and the coefficient C_0, C_1, C_2, C_3 and C_4 obtained from calibration:

$$U_i = C_0 + C_1E_c + C_2E_c^2 + C_3E_c^3 + C_4E_c^4 \tag{B.22}$$

Then, the time averaged velocity $\overline{U}$ can be found from all the instantaneous velocity values. It gives the U_{mean}, too.

$$u_{rms} = \sqrt{\sum_{i=1}^{N}\frac{(U_i - \overline{U})^2}{N-1}} = \sqrt{\sum_{i=1}^{N}\frac{(u_i)^2}{N-1}} \tag{B.23}$$

The turbulence intensity is defined by

$$Tu = \frac{u_{rms}}{U_{mean}} \times 100\% \tag{B.24}$$

c) Integral length scale:

The instantaneous fluctuation velocity u_i is defined by

$$u_i = (U_i - \overline{U}) \tag{B.25}$$

where i is the numbering of sample, i = 1, 2 ..... N.

Then, A is defined as

$$A = \sum_{i}^{N} u_i^2 \tag{B.26}$$

And, B which shows the difference between two values of u_i for all (N-m) samples is defined by

$$B = \sum_{i=1}^{N-m} (u_i \times u_{i+m}) \tag{B.27}$$

From above equations, an autocorrelation is defined as,

$$\varsigma_i = \frac{\frac{B}{N-m}}{\frac{A}{N}} \tag{B.28}$$

It is a coefficient to correct the period of time. If the autocorrelation is close to one, it shows more accurate measurement.

The correct time in which sample (i) is gotten is ($\varsigma_i \Delta t_i$).

Thus;

$$\tau_\Lambda = \sum_{i=1}^{N} \varsigma_i \Delta t_i \tag{B.29}$$

where τ_Λ is the integral time scale, the period of time that all data is achieved.

In the experiment, Δt_i is a constant for i = 1 to N and it is equal to Δt . Thus,

$$\tau_\Lambda = (\sum_{i=1}^{N} \varsigma_i) \Delta t \tag{B.30}$$

Integral length scale is the length that flow with velocity of $\overline{U}$ passing during the integral time scale τ_Λ , i.e.

$$\Lambda = \overline{U} \cdot \tau_\Lambda \tag{B.31}$$

B.3.2 X-PROBE DATA:

a) Temperature of hot-wire:

To calibrate the X-probe, automatic calibrator was used and the change of temperature was considered automatically. All other explanations are similar as these for 1D-probe but, for 2 wires.

b) U_{mean}, u_{rms} and Tu

Instantaneous velocities, U_i and V_i, are found using the volt_corrected1 and volt_corrected2 data and the coefficients achieved from calibration, C_{01}, C_{11}, C_{21}, C_{31} and C_{41} and C_{02}, C_{12}, C_{22}, C_{32} and C_{42} and yaw angles α_1 and α_2:

$$U_{eff} = C_{01} + C_{11}E_{1c} + C_{21}E_{1c}^2 + C_{31}E_{1c}^3 + C_{41}E_{1c}^4 \quad (B.32)$$

$$V_{eff} = C_{02} + C_{12}E_{2c} + C_{22}E_{2c}^2 + C_{32}E_{2c}^3 + C_{42}E_{2c}^4 \quad (B.33)$$

$$\tan(\beta) = (U_{eff} - V_{eff})/[U_{eff} \times \tan(\alpha_2) + V_{eff} \times \tan(\alpha_1)] \quad (B.34)$$

$$U_i = (U_{eff} - V_{eff})/[2 + \tan(\beta) \times (\tan(\alpha_1) - \tan(\alpha_2))] \quad (B.35)$$

$$V_i = U_i \times \tan(\beta) \quad (B.36)$$

All the instantaneous velocity values can be found and the time averaged velocity, $\overline{U}$ and $\overline{V}$ of them can be calculated, too.

For each value, the difference between U_i and $\overline{U}$ is:

$$D = \sqrt{(U_i - \overline{U})^2} \quad (B.37)$$

The difference between V_i and $\overline{V}$ is:

$$D' = \sqrt{(V_i - \overline{V})^2} \quad (B.38)$$

The average of all data for D and D′ for all samples gives the u_{rms} and v_{rms}.

Previous data with following equation gives the turbulence intensity:

$$Tu = \frac{u_{rms}}{U_{mean}} \times 100\% \quad (B.24)$$

Turbulence intensity can be found for each sample and the average of them yields the final result.

c) Integral length scale:

Integral length scale is the length that flow with velocity of $\overline{U}$ passing during the integral time scale. The process of calculation of Λ for X-Probe is the same as 1D- Probe. Only, the velocity is used in equations are achieved by Equation B.35.

REFERENCES

Bradshaw, P., 1971, *An introduction to turbulence and its measurement*, Pergamon Press, Oxford.

Bruun, H. H., 1972, "Interpretation of a hot-wire signal using a universal calibration law," Journal of Physics E: Science Instruments, v 4, pp. 225-231.

Laufer, J., 1954, "The structure of turbulence in fully developed pipe flow," The National Association of Consumer Advocates (NACA) Technical Note No. 2954.

Bruun, H. H., 1996, *Hot-wire anemometry principles and signal analysis*, Oxford University, Chapter 5, pp. 132-160.

APPENDIX C: MATLAB PROGRAM

C.1 1D-PROBE

```
% MATLAB file for processing the measurement data obtained from Hot-wire
Anemometer.

m=0.2;              %Coefficient for air
T0=23;              %Ambient Temperature during calibration.        (ENTER VALUE
HERE)
alfa20=0.36/100;    %Coefficient of heat transfer from the probe
alfaref=alfa20/( 1+alfa20*(T0-23) );
Tw=(0.8/alfaref)+T0; %Hot wire temperature
kin_vis = 0.000015;  %Kinematic Viscosity of air

C0=  -116.3966;  %Factor obtained during calibration        (ENTER VALUE HERE)
C1=  226.0252;  %Factor obtained during calibration         (ENTER VALUE HERE)
C2=  -152.2691;  %Factor obtained during calibration        (ENTER VALUE HERE)
C3=   35.4997;  %Factor obtained during calibration         (ENTER VALUE HERE)
C4=   0.00000;  %Factor obtained during calibratio          (ENTER VALUE HERE)

sample =10000000; %Number of samples collected in each file (ENTER VALUE HERE)
cutoff =0.00003;    %Cutoff point for calc of Integral Length  (ENTER VALUE HERE)
sampling_frequency=80000;          %Sampling Frequency       (ENTER VALUE HERE)

Imax=1;          %Number of points in each quadrant          (ENTER VALUE HERE)
Jmax=1;          %Number of points in each quadrant          (ENTER VALUE HERE)

for loop=1:1;

for i=1:Imax,
for j=1:Jmax,
```

```
section=num2str(loop);
stri=num2str(i);
strj=num2str(j);
zero=num2str(0);
   if (i<1 & j<1)
   filename=['v500A100',section,stri,strj,'.txt'];
elseif (i>1)
   filename=['v500A100',section,zero,stri,strj,'.txt'];
elseif (j>1)
   filename=['v500A100',section,stri,zero,strj,'.txt'];
else
   filename=['v500A100',section,zero,stri,zero,strj,'.txt'];
end

filepath=fullfile('C:','Documents and Settings','Niloofar','Desktop','june-hotwirw','Plate
A',filename); %  (ENTER VALUE HERE)
data=load(filepath ,filename);

% Processing the raw signal to actaul voltage
volt_measured=data(1:sample,1);
volt_actual=(((volt_measured/4096)*10)/8)+1.5;

% Converting raw signal to temperature value
T_actual=((data(sample-1,1))/4096)*10*30;
Temp(i,j,loop)=T_actual;
   if (T_actual>T0)
        m = -0.2;
     else
        m = 0.2;
     end
```

```
volt_corrected=volt_actual*( (Tw-T0)/(Tw-T_actual) ).^(0.5*(1));
 % Converting Voltage to velocity
UU=C0 + C1*volt_corrected + C2*volt_corrected.^2 + C3*volt_corrected.^3 +
C4*volt_corrected.^4;
U=UU(1:sample);          % Deselecting the last value (because it is for temperature)
Um=mean(U);

% Calculating the required parameters
Umean(i,j,loop)=Um;
A=(U-Um).^2;
B=A.^0.5;
Urms(i,j,loop)= mean(B);
Intensity(i,j,loop)=(100*Urms(i,j,loop)/Umean(i,j,loop));

% Calculating the Intergal Length Scale
small_sample = sample;      % Initialising
length_n = 1;  flag=0;      % Initialising
row1=0; row2=0;             % Initialising

U_inst_small_sample = U(1:small_sample);
U_mean_small_sample = mean(U_inst_small_sample);
u_inst = U_inst_small_sample - U_mean_small_sample;
u_rms_small_sample = (mean( u_inst.^2 ))^0.5;

for n=0:small_sample-1,
        % break;        %  Can be switched ON when Integral length isn't needed
                        %  calculation is NOT required.
   flag=0;
   for k=1:small_sample-n,
      flag = flag + (u_inst(k)*u_inst(k+n));
   end
```

```
    row2(n+1) = (flag/(small_sample-n))/(u_rms_small_sample^2) ;

     %if (row2(n+1) < cutoff)
     if (row2(n+1) > cutoff)
        length_n = n;
        break;
     end
 end
   tau=sum(row2)/sampling_frequency;
   intergral_length(i,j,loop)=tau*U_mean_small_sample;

   filename
end
end
end
x=linspace(0,Imax-1,Imax);
y=linspace(0,Jmax-1,Jmax);
```

C.2 X-PROBE

```
gain=1;
offset=0;
C01=  -7.557750;  %Factor obtained during calibration      (ENTER VALUE HERE)
C11=  45.601498;  %Factor obtained during calibration      (ENTER VALUE HERE)
C21= -51.246670;  %Factor obtained during calibration      (ENTER VALUE HERE)
C31=  16.401369;  %Factor obtained during calibration      (ENTER VALUE HERE)
C41=   0.000004;  %Factor obtained during calibration      (ENTER VALUE HERE)
C02= -17.131353;  %Factor obtained during calibration      (ENTER VALUE HERE)
C12=  62.126469;  %Factor obtained during calibration      (ENTER VALUE HERE)
C22= -61.205242;  %Factor obtained during calibration      (ENTER VALUE HERE)
C32=  18.528982;  %Factor obtained during calibration      (ENTER VALUE HERE)
C42=   0.000004;  %Factor obtained during calibration      (ENTER VALUE HERE)
```

```
theta1= 41.7872000*pi/180;        %Factor obtained during calibration
        (ENTER VALUE HERE)
theta2= 41.5955000*pi/180;    %Factor obtained during calibration
        (ENTER VALUE HERE)
T0=20.3;  %Ambient Temperature during calibration.          (ENTER VALUE HERE)

alfa20=0.36/100;      %Coefficient of heat transfer from the probe
alfaref=alfa20/( 1+alfa20*(T0-20) );
Tw=(0.8/alfaref)+T0;  %Hot wire temperature
kin_vis = 0.000015    %Kinematics Viscosity of air

sample=10000000; %Number of samples collected in each file  (ENTER VALUE HERE)
cutoff=0.0001;    %Cutoff point for calc of Integral Length      (ENTER VALUE HERE)
sampling_frequency=80000;          %Sampling Frequency        (ENTER VALUE HERE)

Imax=1;          %Number of points in each quadrant              (ENTER VALUE HERE)
Jmax=1;          %Number of points in each quadrant              (ENTER VALUE HERE)

%Initialization
quadrants=1; temp_x=0; temp_y=0;
Umean_xyplot(1:Imax*Jmax*quadrants,1:1)=0;
Urms_xyplot(1:Imax*Jmax*quadrants,1:1)=0;
Uintensity_xyplot(1:Imax*Jmax*quadrants,1:1)=0;
Uskewness_xyplot(1:Imax*Jmax*quadrants,1:1)=0;
Uflatness_xyplot(1:Imax*Jmax*quadrants,1:1)=0;
Ueps_xyplot(1:Imax*Jmax*quadrants,1:1)=0;
Ukol_xyplot(1:Imax*Jmax*quadrants,1:1)=0;
Uintegral_length_xyplot(1:Imax*Jmax*quadrants,1:1)=0;
UV_xyplot(1:Imax*Jmax*quadrants,1:1)=0;

Vmean_xyplot(1:Imax*Jmax*quadrants,1:1)=0;
```

```
Vrms_xyplot(1:Imax*Jmax*quadrants,1:1)=0;
Vintensity_xyplot(1:Imax*Jmax*quadrants,1:1)=0;
Vskewness_xyplot(1:Imax*Jmax*quadrants,1:1)=0;
Vflatness_xyplot(1:Imax*Jmax*quadrants,1:1)=0;
Veps_xyplot(1:Imax*Jmax*quadrants,1:1)=0;
Vkol_xyplot(1:Imax*Jmax*quadrants,1:1)=0;
Vintegral_length_xyplot(1:Imax*Jmax*quadrants,1:1)=0;

for loop=1:1;

for i=1:Imax,
for j=1:Jmax,

   section=num2str(loop);
   stri=num2str(i);
   strj=num2str(j);
   zero=num2str(0);

   if (i<1 & j<1)
      filename=['v500A100',section,stri,strj,'.txt'];
   elseif (i>1)
      filename=['v500A100',section,zero,stri,strj,'.txt'];
   elseif (j>1)
      filename=['v500A100',section,stri,zero,strj,'.txt'];
   else
      filename=['v500A100',section,zero,stri,zero,strj,'.txt'];
   end

   filepath=fullfile('c:','Documents and Settings','Niloofar','Desktop','june-hotwirw','Plate
A',filename);  %  (ENTER VALUE HERE)
   data=load(filepath,filename);
```

```
% Separating the velocity data (U &V)
E1=data(1:sample,1);
E2=data(1:sample,2);

% Processing the raw signal to actaul voltage
volt_corrected1=volt_actual1=volt_measured1=(E1/4096)*10/gain+offset;
volt_corrected2=volt_actual2=volt_measured2=(E2/4096)*10/gain+offset;

% Converting Voltage to velocity
Ueff1=C01 + C11*volt_corrected1 + C21*volt_corrected1.^2 +
C31*volt_corrected1.^3 + C41*volt_corrected1.^4;
Ueff2=C02 + C12*volt_corrected2 + C22*volt_corrected2.^2 +
C32*volt_corrected2.^3 + C42*volt_corrected2.^4;
tan_Beta=(Ueff1-Ueff2)./(Ueff1*tan(theta2)+Ueff2*tan(theta1));
cos_Beta=cos(atan(tan_Beta));
U=(Ueff1+Ueff2)./(2+tan_Beta*(tan(theta1)-tan(theta2)));
V=U.*tan_Beta;

Um=mean(U);
Vm=mean(V);

% Calculating the required parameters (U)
Umean(i,j,loop)=Um;
Urms(i,j,loop)=( mean( (U-Um).^2 ) )^0.5;
Uintensity(i,j,loop)=(100*Urms(i,j,loop)/Umean(i,j,loop));
UV(i,j,loop)= mean( (U-Um).*(V-Vm) );

% Calculating the required parameters (V)
Vmean(i,j,loop)=Vm;
Vrms(i,j,loop)=( mean( (V-Vm).^2 ) )^0.5;
```

```
% Calculating the Intergal Length Scale (U)
small_sample = sample/2;     % Initialising
length_n = 1;  flag=0;       % Initialising
row1=0; row2=0;              % Initialising

U_inst_small_sample = U(1:small_sample);
U_mean_small_sample = mean(U_inst_small_sample);
u_inst = U_inst_small_sample - U_mean_small_sample;
u_rms_small_sample = (mean( u_inst.^2 ))^0.5;

for n=0:small_sample-1,
% break; %  Can be switched ON when Integral length          (ENTER VALUE HERE)
                    %  calculation is NOT required.
    flag=0;
    for k=1:small_sample-n,
      flag = flag + (u_inst(k)*u_inst(k+n));
    end

    row2(n+1) = (flag/(small_sample-n))/(u_rms_small_sample^2) ;

    if (row2(n+1) < cutoff)
      length_n = n;
      break;
    end

end

tau=sum(row2)/sampling_frequency;
Uintegral_length(i,j,loop) = tau*U_mean_small_sample*1000;          % Converted to
millimeters (mm)
```

```
   % Calculating the Intergal Length Scale (V)
   Vintegral_length(i,j,loop) = 0*1000;                    % Converted to millimeters
(mm)

   % Writing the data into xy_plots
   serial=1;

   Umean_xyplot(serial,1)=temp_x;
   Urms_xyplot(serial,1)=temp_x;
   Uintensity_xyplot(serial,1)=temp_x;
   Uintegral_length_xyplot(serial,1)=temp_x;
   UV_xyplot(serial,1)=temp_x;
   Vmean_xyplot(serial,1)=temp_x;
   Vrms_xyplot(serial,1)=temp_x;
   Vintegral_length_xyplot(serial,1)=temp_x;
```

APPENDIX D: SPHERE SETUP

As mentioned in Section 3.3, to minimize the influence of sphere support on the results, high strength polymer strings were used to position the sphere. Two threaded holes of 9 mm in diameter and 20 mm in depth are in each sphere, to allow the fastening of the supporting strings via two screws. After the screws were tightly secured to the sphere, the holes were filled with Epoxy. A total of eight strings were utilized, four of which were fastened to the top hole and another four to the bottom one. The other ends of the top strings were fastened firmly and laid symmetrically to the two side walls of the wind tunnel, with each making an angle of $\alpha \pm 0.3°$ with respect to the test section wall and $\beta \pm 0.3°$ to the streamwise direction of the wind tunnel; see Figure 21. In the case of the bottom strings, the other ends were secured firmly to the floor of the wind tunnel making an angle of $\alpha' \pm 0.3°$ with respect to the test section floor and $\beta' \pm 0.3°$ to the streamwise direction of the wind tunnel; see Figure 21.

In installation of PVC spheres, the mounting point on the side wall and tunnel floor varied for different spheres. Therefore, there were fixed values for α, β, α', and β' angles; see Table D.1. However, in the case of wood spheres, the mounting points were the same for all six spheres. Thus, the β and β' angles were fixed, 37.2° and 40.97°, respectively. But α and α' were varied in each setup; see Table D.2.

Table D.1: Springs angle in PVC sphere setup

Sphere diameter size	α	β	α'	β'
All three spheres (20 mm, 51 mm, 102 mm)	40.4°	63.5°	44.8°	59.7°

Table D.2: String angle in wooden sphere setup

Sphere diameter size	α	α'
20 mm	53.6°	49.8°
51mm	54.9°	51.2°
65 mm	55.4°	51.8°
102 mm	57.0°	53.4°
140 mm	58.7°	55.2°
210 mm	62.0°	58.7°

APPENDIX E: UNCERTAINTY ANALYSIS

The main source of uncertainty in the hot-wire measurement came from its calibration, which included three parts, i.e. the velocity measurement, the curve fitting and the digitized hot-wire anemometer output. In the second part of the experiment, drag force measurement was performed using a load cell to achieve drag coefficient on the three spheres. The uncertainty in the drag measurement came from four different sources, i.e. the sphere diameter measurement, the velocity measurement, the air density calculation, and the load cell measurement.

E.1 UNCERTAINTIES IN HOT-WIRE DATA

The uncertainty of hot-wire results came from the process of calibrating the hot-wire probe and the process of acquiring the instantaneous velocity data. In this appendix, the uncertainty in the time averaged flow velocity $\overline{U}$, the turbulence rms velocity, the turbulence intensity and the turbulence length scale, Λ will be specified.

The uncertainties in the above parameters were estimated on the basis of the uncertainty in the instantaneous velocity U_i In other words, the first step in this uncertainty analysis was to estimate the uncertainty in U_i. In fact, the instantaneous velocity U_i forms the starting point of all the subsequent data analysis.

E.1.1 CALIBRATION UNCERTAINTY

The calibration uncertainty was induced by three sources, i.e. the uncertainty in the velocity, U_{error}, used as the calibration standard; the uncertainty in voltage reading, E_{error}, corresponding to the U_{error}; and the uncertainty from the curve-fitting pairs of velocity and voltage values which give the coefficient used for calibration equation $U_{eff} = C_0 + C_1E_c + C_2E_c^2 + C_3E_c^3 + C_4E_c^4$. The uncertainty in the measured voltage reading, E_{error}, was negligible in compare with others. The relative velocity uncertainty, ΔU_{e_fit}, due to the curve fitting error is around 0.5%. When the relative velocity uncertainty ΔU_{e_vel} measured by Pitot-static tube, manual calibration system, was 2% at most. When the

relative velocity uncertainty ΔU_{e_vel} measured by auto calibrator was 1% at most. Thus, the total relative velocity uncertainties because of the calibrations are:

Manual calibration:

$$\Delta U_{e_cal} = \sqrt{(\Delta U_{e_vel})^2 + (\Delta U_{e_fit})^2} \cong 2.1\% \quad \text{(E.1)}$$

Automatic calibration:

$$\Delta U_{e_cal} = \Delta V_{e_cal} = \sqrt{(\Delta U_{e_vel})^2 + (\Delta U_{e_fit})^2} \cong 1.12\% \quad \text{(E.2)}$$

E.1.2 DATA ACQUISITION UNCERTAINTY

The data acquisition uncertainty resulted from two sources, i.e. the digitization uncertainty from digitizing, the analog signal from the hot-wire anemometer and the uncertainty from the probe positioning.

The uncertainty in the digitized hot-wire anemometer output voltage is ± 0.5 of the least significant bit, which, for the 12 bits A/D with an input range set as 0 to 10V, [Dantec dynamics Manual, 2000]:

$$\Delta E = {0.5 \times 10}/{2^{12}} = 0.0012V \quad \text{(E.3)}$$

The relative digitization uncertainty, ΔU_{e_dig} in the effective velocity is:

$$\Delta U_{e_dig} = \frac{\Delta E}{U_{eff}} \frac{dU_{eff}}{dE} = \frac{\Delta E}{U_{eff}} \frac{d\left(C_0 + C_1 E_c + C_2 E_c^2 + C_3 E_c^3 + C_4 E_c^4\right)}{dE} \quad \text{(E.4)}$$

In this study, for the range of velocity between 3 m/s to 12 m/s, the relative digitization uncertainty was less than 1% in Experiment I in which manual calibrator is used, and less than 0.4% in Experiment II in which Auto calibrator is used.

Aligning the hot-wire probe with the mean flow direction makes the probe positioning uncertainty, ΔU_{e_pos}.

$$\Delta U_{e_pos} = \frac{1}{\sqrt{3}}(1 - \cos\alpha) \quad \text{[Jorgensen, 1997]} \quad \text{(E.5)}$$

where α is the yaw angle. However, an error of $\pm 1^\circ$ when aligning it is possible. Thus, this uncertainty is 8.8×10^{-5}. It is too small and thus negligible.

The total relative uncertainty due to data acquisition can be estimated as:

$$\Delta U_{e_daq} = \sqrt{\left(\Delta U_{e_dig}\right)^2 + \left(\Delta U_{e_pos}\right)^2} \cong \left|\Delta U_{e_dig}\right| \tag{E.6}$$

Thus, the total relative velocity uncertainty in the effective velocity due to calibration and data acquisition is:

$$\Delta(U_{eff}) = \sqrt{\left[\Delta U_{e_cal}\right]^2 + \left[\Delta U_{e_daq}\right]^2} \cong \sqrt{\left[\Delta U_{e_cal}\right]^2 + \left[\frac{\Delta E}{U_{eff}}\left(C_1 + C_2E_c + C_3E_c^2 + C_4E_c^3\right)\right]^2} \tag{E.7}$$

All above calculations are for experiment with 1D hot-wire probe. In Experiment II, the X-probe, 2D hot-wire probe is used. In that situation, all the calculations are the same, except that there are two effective velocities, U_{eff} and V_{eff}. In ΔU_{eff} calculation, the E_{1c} voltage and C_{01}, C_{11}, C_{21}, C_{31} and C_{41} coefficients are used. And, in ΔV_{eff} calculation, the E_{2c} voltage and C_{02}, C_{12}, C_{22}, C_{32} and C_{42} coefficients are used.

E.1.3 UNCERTAINTY OF INSTANTANEOUS FLOW VELOSITY

For the 1D probe measurement, the absolute uncertainty in the effective velocity is:

$$W(U_{eff}) = W(U_i) = \Delta(U_{eff})U_{eff1} = U_{eff1}\sqrt{0.0004 + \left[\frac{\Delta E}{U_{eff1}}\left(C_{11} + C_{12}E_{1c} + C_{13}E_{1c}^2 + C_{14}E_{1c}^3\right)\right]^2} \tag{E.8}$$

For the 2D probe measurement, the absolute uncertainty in the effective velocity is:

$$W(U_i) = \sqrt{(\Delta(U_{eff})U_{eff1})^2 + (\Delta(V_{eff})V_{eff1})^2 + e} = \sqrt{\left(U_{eff}^2\left(0.0001 + \left[\frac{\Delta E}{U_{eff1}}\left(C_{11} + C_{12}E_{1c} + C_{13}E_{1c}^2 + C_{14}E_{1c}^3\right)\right]^2\right)\right) + \left(V_{eff}^2\left(0.0001 + \left[\frac{\Delta E}{V_{eff1}}\left(C_{21} + C_{22}E_{2c} + C_{23}E_{2c}^2 + C_{24}E_{2c}^3\right)\right]^2\right)\right) + e} \tag{E.9}$$

where e is the uncertainty because of yaw angle which is negligible.

Thus,

$$W(V_i) \approx W(U_i) \tag{E.10}$$

E.1.4 UNCERTAINTIES IN TURBULENCE PARAMETERS

1) The time-averaged flow velocities $\overline{U}$ and $\overline{V}$ is calculated as:

$$\overline{U} = \frac{1}{N}\sum_{i=1}^{N} U_i \tag{E.11}$$

and

$$\overline{V} = \frac{\sum_{i=1}^{N} V_i}{N} \tag{E.12}$$

of which the uncertainties are estimated by:

$$W(\overline{U}) = \sqrt{\sum_{i=1}^{N}\left(\frac{\partial \overline{U}}{\partial U_i} W(U_i)\right)^2} = \frac{1}{N}\sqrt{\sum_{i=1}^{N}(W(U_i))^2} \tag{E.13}$$

and

$$W(\overline{V}) = \sqrt{\sum_{i=1}^{N}\left(\frac{\partial \overline{V}}{\partial V_i} W(V_i)\right)^2} = \frac{1}{N}\sqrt{\sum_{i=1}^{N}(W(V_i))^2} \tag{E.14}$$

2) The variance of turbulence fluctuation velocities are calculated as:

$$\overline{u^2} = \frac{1}{N}\sum_{i=1}^{N}(U_i - \overline{U})^2 \tag{E.15}$$

and

$$\overline{v^2} = \frac{1}{N}\sum_{i=1}^{N}(V_i - \overline{V})^2 \tag{E.16}$$

of which the uncertainties are estimated by:

$$W\left(\overline{u^2}\right) = \sqrt{\left[\frac{\partial \overline{u^2}}{\partial \overline{U}} W(\overline{U})\right]^2 + \sum_{i=1}^{N}\left[\frac{\partial\left(\overline{u^2}\right)}{\partial U_i} W(U_i)\right]^2} = \frac{2}{N}\sqrt{\sum_{i=1}^{N}\left[(U_i - \overline{U})^2\left[W^2(\overline{U}) + W^2(U_i)\right]\right]} \tag{E.17}$$

and

$$W\left(\overline{v^2}\right)=\sqrt{\left[\frac{\partial\overline{v^2}}{\partial\overline{V}}W\left(\overline{V}\right)\right]^2+\sum_{i=1}^{N}\left[\frac{\partial\left(\overline{v^2}\right)}{\partial V_i}W\left(V_i\right)\right]^2}= \frac{2}{N}\sqrt{\sum_{i=1}^{N}\left[\left(V_i-\overline{V}\right)^2\left[W^2\left(\overline{V}\right)+W^2\left(U_i\right)\right]\right]} \tag{E.18}$$

therefore,

$$W(u)=\frac{\partial u}{\partial\overline{u^2}}W\left(\overline{u^2}\right)=\frac{1}{2u}W\left(\overline{u^2}\right) \tag{E.19}$$

and

$$W(v)=\frac{\partial u}{\partial\overline{v^2}}W\left(\overline{v^2}\right)=\frac{1}{2v}W\left(\overline{v^2}\right) \tag{E.20}$$

In Experiment I in which 1D hot-wire system used to measure the velocity, the maximum uncertainties in $\overline{U}$ and u_{rms} are estimated to be 2.3% and 3.7%, respectively, while their average uncertainties are estimated to be 2.15% and 3%, respectively.

In Experiment II in which 2D hot-wire system used to measure the velocity, the maximum uncertainties in $\overline{U}$ and u_{rms} are estimated to be 1.2% and 2%, respectively, while their average uncertainties are estimated to be 1.1% and 1.7%, respectively.

3) The turbulence intensity, Tu is calculated as:

$$Tu\%=\frac{u_{rms}}{\overline{U}}\times 100 \tag{E.21}$$

Thus, its uncertainty is estimated by:

$$\frac{W_{Tu}}{Tu}=\sqrt{\left(\frac{W_{\overline{U}}}{\overline{U}}\right)^2+\left(\frac{W_{u_{rms}}}{u_{rms}}\right)^2} \tag{E.22}$$

In Experiments I and II, the maximum uncertainties of turbulence intensity are 4.3% and 2.4%. And, the average ones are 3.7% and 2%, respectively.

4) The integral length scale Λ is calculated as explained in Sections 3.2.3, and its uncertainty is estimated as:

$$\frac{W_{\varsigma}}{\varsigma} = \sqrt{\left(\frac{W_{(\overline{u^2})}}{(\overline{u^2})}\right)^2 + \left(\frac{2W_u}{u}\right)^2} \tag{E.23}$$

and

$$\frac{W_{\tau_\Lambda}}{\tau_\Lambda} = \sqrt{\left(\frac{W_{\varsigma(i\Delta t)}}{\varsigma(i\Delta t)}\right)^2} \tag{E.24}$$

and

$$\frac{W_\Lambda}{\Lambda} = \sqrt{\left(\frac{W_{\overline{U}}}{\overline{U}}\right)^2 + \left(\frac{W_{\tau_\Lambda}}{\tau_\Lambda}\right)^2} \tag{E.25}$$

In Experiments I and II, the maximum uncertainties of integral length scale are 7.8% and 4.2%. And, the average ones are 6.5% and 3.6%, respectively.

E.2 UNCERTAINTIES IN DRAG MESURMENT

E.2.1 UNCERTAINTY IN SPHERE DIAMETER (d) MEASURMENT

The diameter of the sphere is measured with a dial-caliper. The caliper has a resolution of 0.0254 mm and an accuracy of ±0.0127 mm. On the other hand, the measurement showed that the spheres are not completely perfect. Their maximum inaccuracy is ± 0.8 mm. Thus, the maximum and average uncertainties of sphere diameter measurement are 4% and 1.8%, respectively.

E.2.2 UNCERTAINTY IN REYNOLDS NUMBER

To find the Reynolds number, the atmospheric temperature and pressure of the lab are measured with a mercury thermometer and barometer with resolution of 1°C and 0.1mmHg, respectively, giving an accuracy of ±0.5°C and ±0.05 mmHg. The maximum variation in the room temperature is about ±1°C and the maximum variation in the room pressure is ±5 mmHg. The zero order precision error is considered to be based on unsteadiness in temperature and the readability of the instrument. Thus, the maximum relative uncertainty in the measurement of temperature and pressure are about 5.6% and

0.7%, respectively. And, the averaged relative uncertainty in the measurement of temperature and pressure are about 3% and 0.4%, respectively.

To adjust the wind tunnel power, the mean flow velocity in the wind tunnel is measured by Pitot-static tube and the digital manometer, too. Also, the data can be used to compare with hot-wire data. The resolution of the digital manometer is 0.1 Pa. Thus, its accuracy is ±0.05 Pa. The variation of measurement in each time is about ±1 Pa. The mean flow velocity is calculated by:

$$\Delta P = \frac{1}{2}\rho_{air} U^2 \tag{E.26}$$

where the air density is pre-determined from the measured values of the lab temperature and pressure, and by applying the ideal gas law. Equation E.26 is changed to the following form by substituting for ρ_{air}:

$$U = \sqrt{\frac{(2\Delta P)RT_{air}}{P_{air}}} \tag{E.27}$$

Finally, the uncertainty of the mean flow velocity is obtained by:

$$\frac{W_U}{U} = \sqrt{\left(\frac{1}{2}\frac{W_{\Delta P}}{\Delta P}\right)^2 + \left(\frac{1}{2}\frac{W_T}{T}\right)^2 + \left(\frac{1}{2}\frac{W_P}{P}\right)^2} \tag{E.28}$$

Thus, the maximum and averaged uncertainties of velocity by Pitot-Static tube measurement are 3.3% and 3.12%.

Now, to calculate the uncertainty of Reynolds number, Equation E.30 is used,

$$Re = \frac{Ud}{\nu} \tag{E.29}$$

$$\frac{W_{Re}}{Re} = \sqrt{\left(\frac{W_U}{U}\right)^2 + \left(\frac{W_d}{d}\right)^2 + \left(\frac{W_\nu}{\nu}\right)^2} \tag{E.30}$$

The maximum and average relative uncertainties of Reynolds numbers based on Pitot-static tube and the digital monometer measurement are 5.18% and 3.6%. Using the result of the hot-wire measurement uncertainty with manual calibration, the maximum and average relative uncertainties of Reynolds numbers are 4.61% and 2.17%. Using the result of the hot-wire measurement uncertainty with automatic calibration, the maximum and average relative uncertainties of Reynolds numbers are 4.17% and 2.11%.

E.2.3 UNCERTAINTY IN DRAG FORCE AND DRAG COEFFICIENT

The load cell gives the data in mili-voltage with a resolution of 0.0001 (mV) and accuracy of achieved data as ±0.00005 (mV). By calibrating the load cell, the amplifier data are converted to force with an accuracy of ±0.00005 (N) because of the linear relation between them. It causes the maximum uncertainty of 9.5% and the averaged one of 7.4%.

Finally, since the drag coefficient C_D is calculated by:

$$C_D = \frac{F_D}{\frac{1}{2}\rho U^2\left(\frac{\pi d^2}{4}\right)} \tag{E.23}$$

The overall uncertainty of the drag coefficient is estimated as:

$$\frac{W_{C_D}}{C_D} = \sqrt{\left(\frac{W_{F_D}}{F_D}\right)^2 + \left(\frac{1}{2}\frac{W_d}{d}\right)^2 + \left(\frac{1}{2}\frac{W_U}{U}\right)^2 + \left(\frac{W_\rho}{\rho}\right)^2} \tag{E.24}$$

Also, in the installation of sphere, a force in drag force direction is in the downstream wires. It is equal to the difference of force because of the angle of the installation. It can cause less than 1% more uncertainty in drag coefficient.

In this study, the maximum and average uncertainties of drag coefficient are around 10.5% and 7.8%.

E.2.4 UNCERTAINTY IN ROUGHNESS

Westerman and Sharcos [1966] showed that mechanically the smooth model should have roughness less than 1μm. As shown in Figures E.1 and E.2 the PVC and wooden spheres have roughness of 0.97 μm and 16.99 μm, respectively. Thus, the PVC spheres are mechanically smooth but wooden spheres are not completely smooth. Also, Hunt and Vaughan [1996] showed that related to Moody diagram the smooth model has relative roughness less than 0.000001. But, maximum relative roughness of PVC and wooden spheres are 0.00005 and 0.0008, respectively. These values make 2.5% and 15.5% different with smooth models. But on the other hand, the minimum relative roughness for sphere to have some visible effect of C_D is around 0.0015 which is bigger than these models. Thus, the roughness has negligible effect.

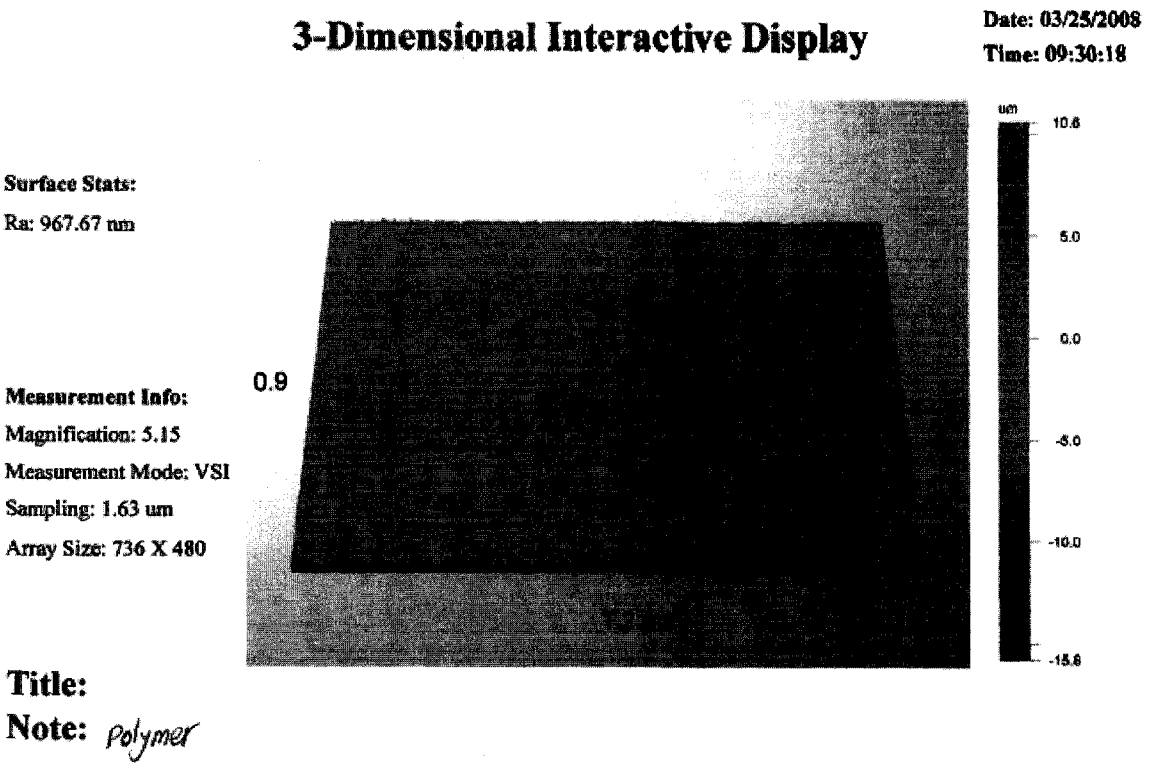

Figure E.1: The roughness of PVC spheres

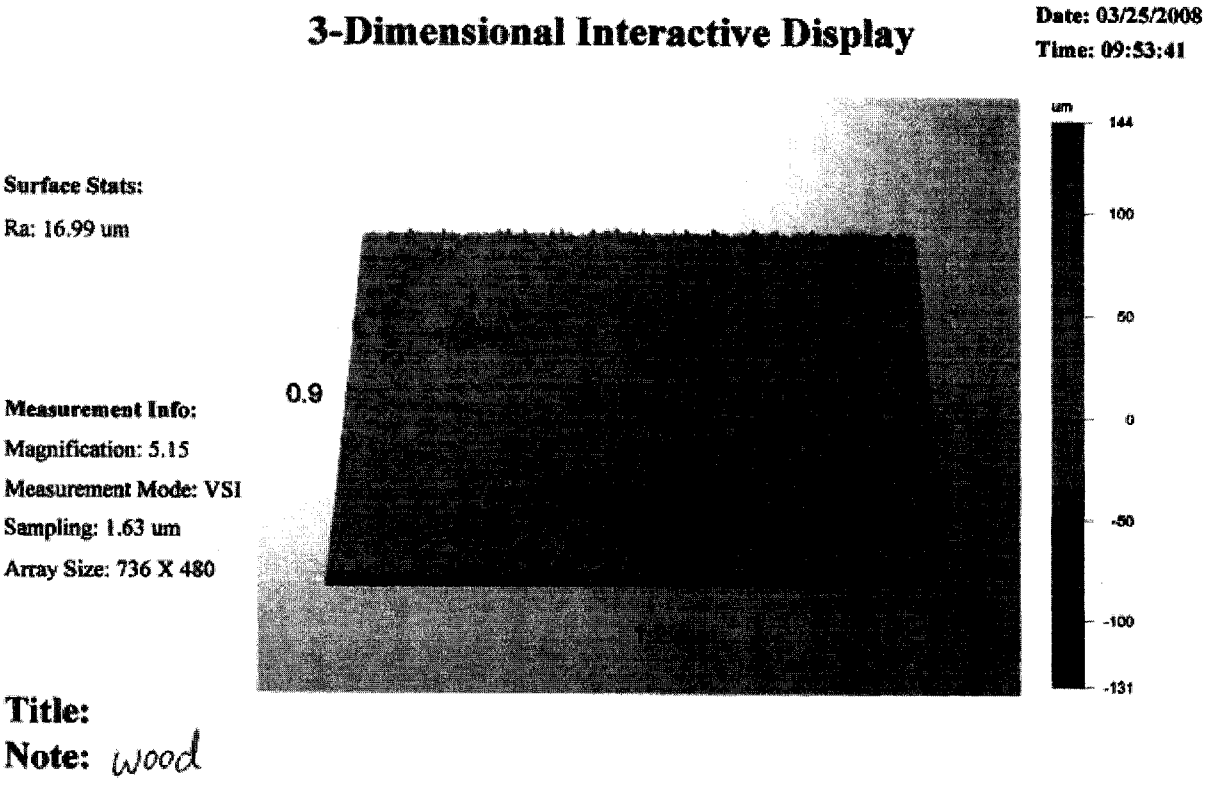

Figure E.2: The roughness of wooden spheres

REFERENCES

"Streamline_streamware installation and users guide," Dantec dynamics, Denmark, 2000.

Jorgensen, F. E., Hammer, M., 1997, "Hot-wire anemometry behavior at very high frequencies," Measurement Science Technology, v 8, p 221.

Westerman, J., Sharcos, E., 1966, "DIN 140 Standard (classified surface quality grade)" No. 1304 standard, pp.160-200.

Hunt, T. M., Vaughan, N., 1996, *Hydraulic Handbook*, 9th Edition, Elsevier, p 8-A-2.

APPENDIX F: X-PROBE RESULTS

The X-Probe hot-wire measurement gives the results of the velocity, the root square velocity, turbulence intensity and integral length scale measured by X-Probe. The velocity in y components V is close to zero. In fact, V is changed from 0.018 (m/s) to 0.081 (m/s) which is close to 0. The following figures present the root square velocity, turbulence intensity and integral length scale. Figure F.1 shows the variation of the rms velocity versus (x/D) in different mean velocities, where x is the distance between the hot-wire and the orificed perforated plate with hole diameter D. Figure F.2 shows the turbulence intensity versus (x/D) in different mean velocities. And, the integral length scales corresponding to turbulent flow at different mean velocities are shown in Figure F.3.

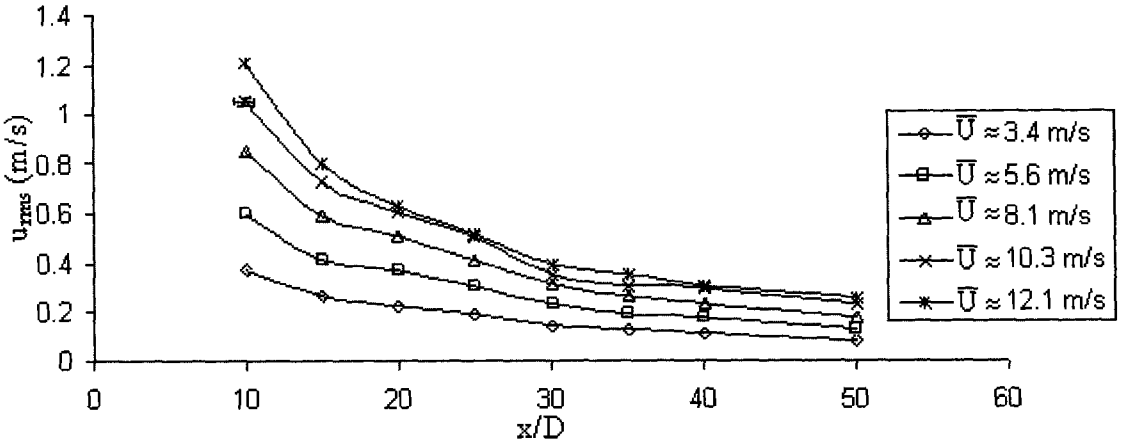

(a) Plate D = 25 mm

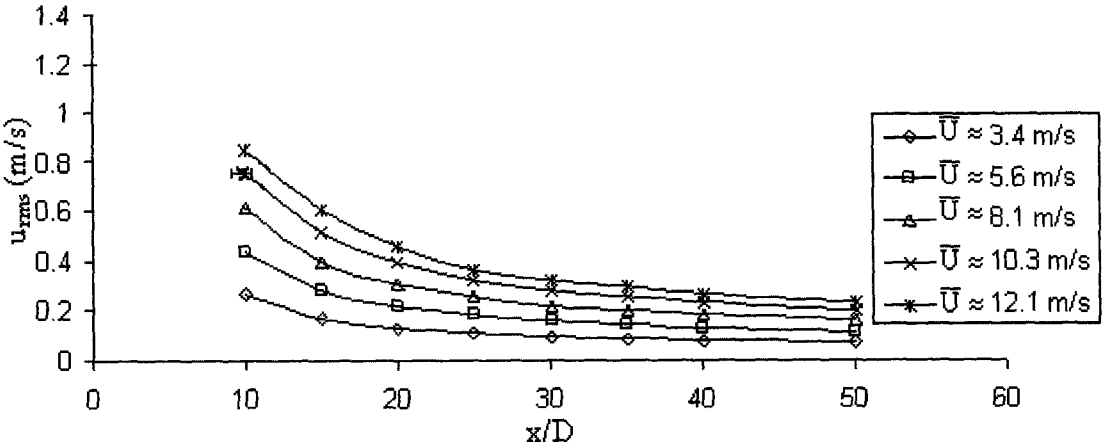

(b) Plat D = 37.5 mm

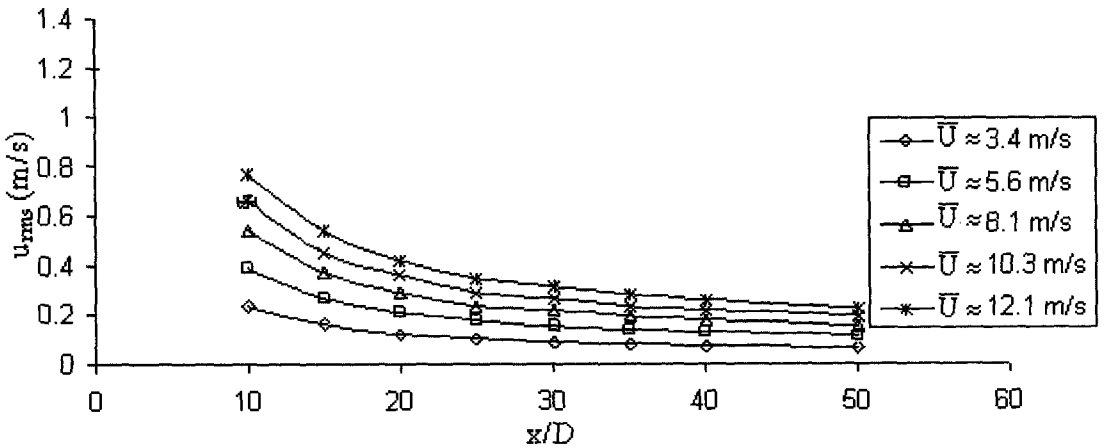

(c) Plate D = 50 mm

Figure F.1: Variation of rms velocity (m/s) in x direction with respect to (x/D) in 2D hot-wire measurement: (a) with perforated plate D-25 (b) with perforated plate D-37.5 and (c) with perforated plate D-50

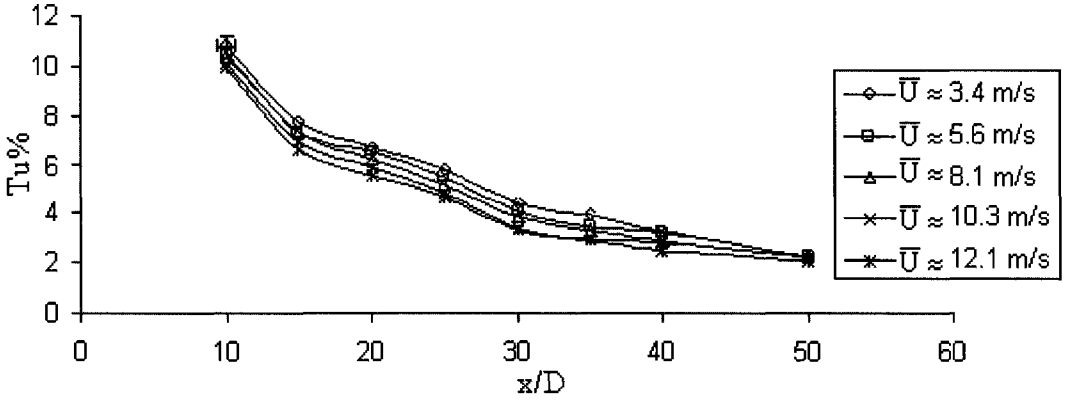

(a) Plate D = 25 mm

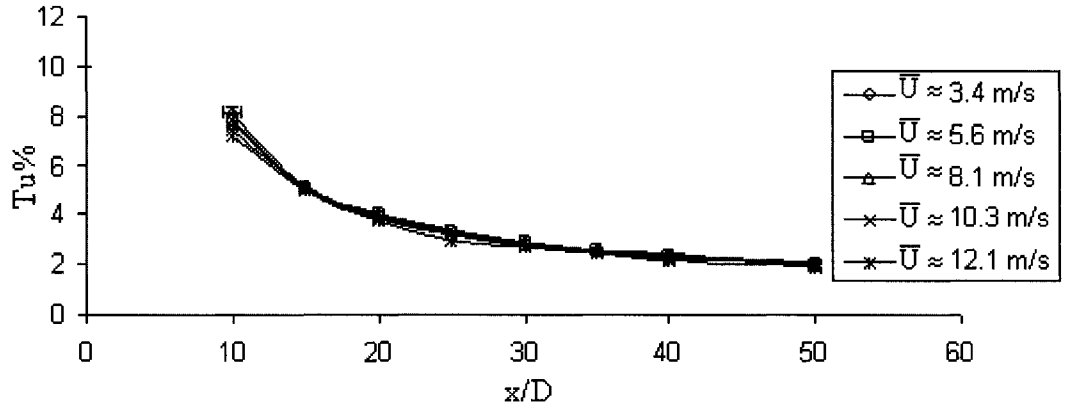

(b) Plate D = 37.5 mm

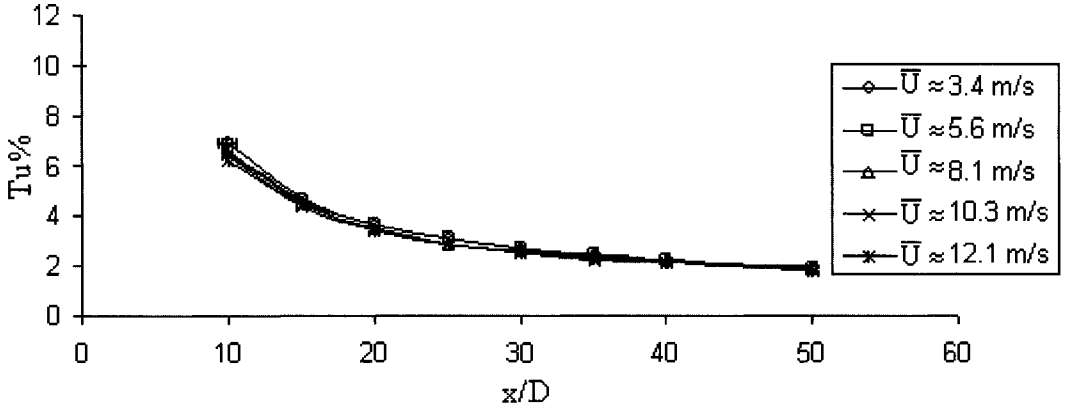

(c) Plate D = 50 mm

Figure F.2: Variation of relative turbulence intensity with respect to (x/D) in 2D hot-wire measurement: (a) with perforated plate D-25 (b) with perforated plate D-37.5 and (c) with perforated plate D-50

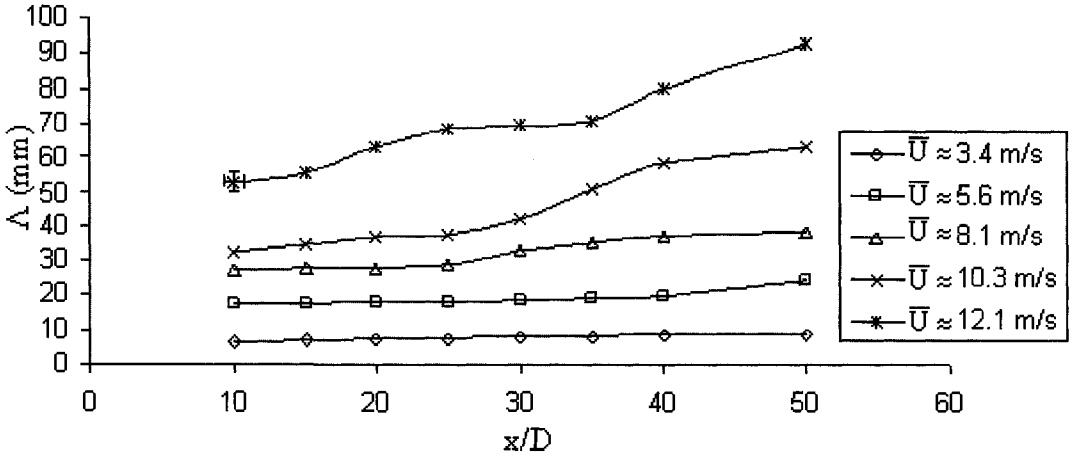

(a) Plate D = 25 mm

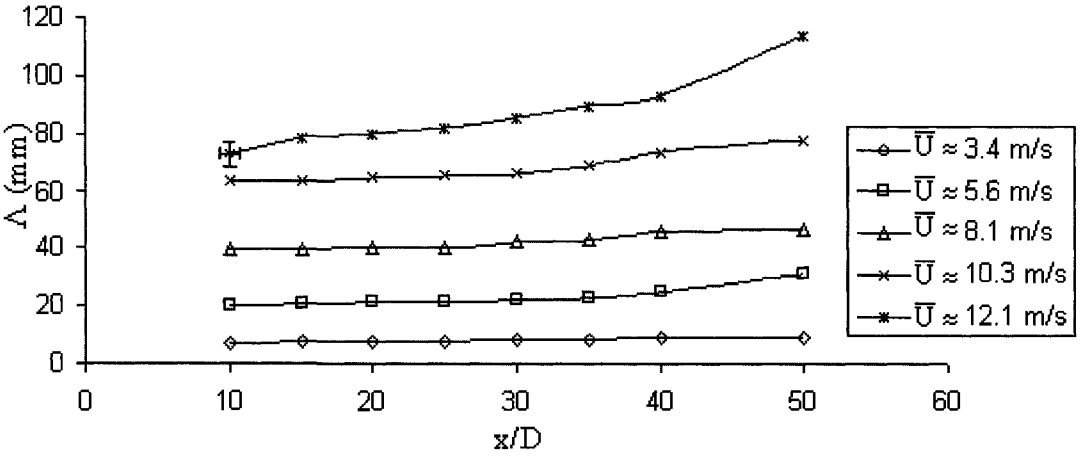

(b) Plate D = 37.5 mm

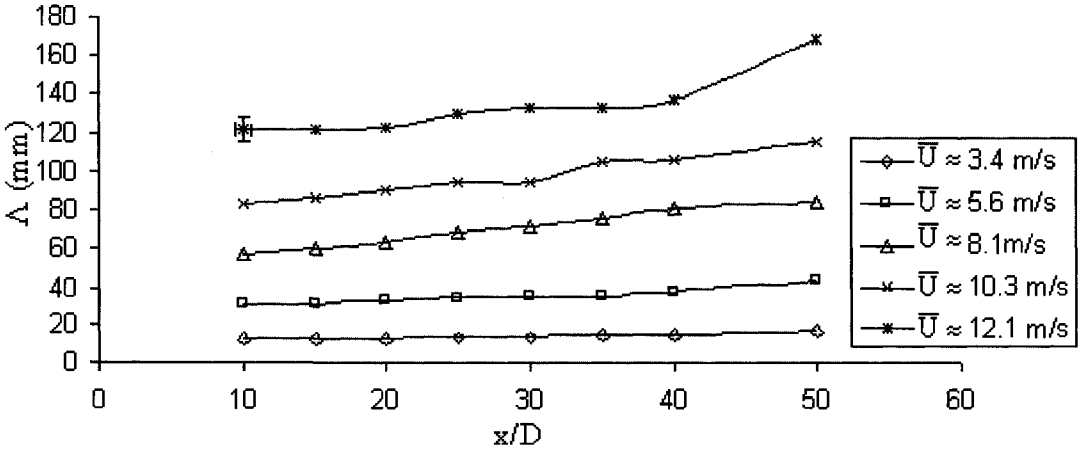

(c) Plate D = 50 mm

Figure F.3: Variation of integral length scale with respect to (x/D) in 2D hot-wire measurement: (a) with perforated plate D-25 (b) with perforated plate D-37.5 and (c) with perforated plate D-50

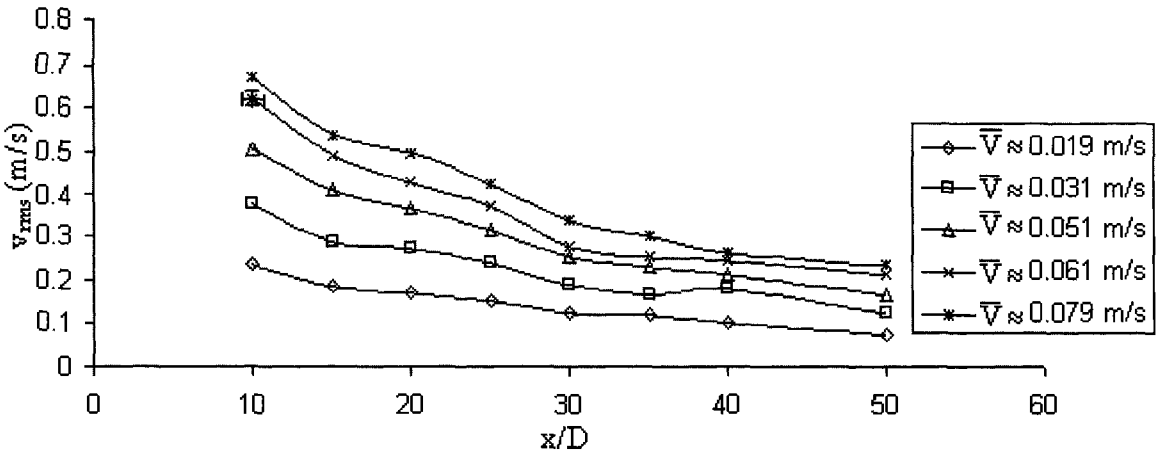

(a) Plate D = 25 mm

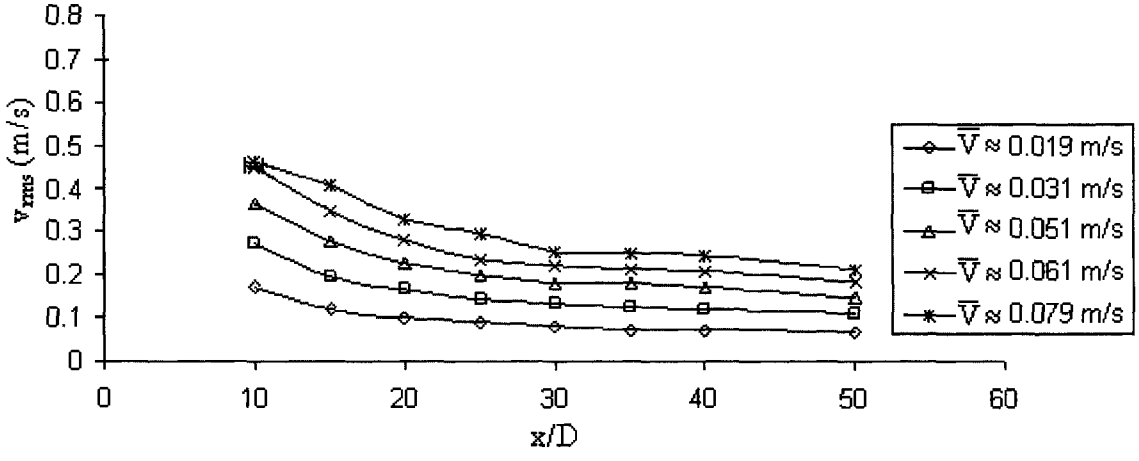

(b) Plat D = 37.5 mm

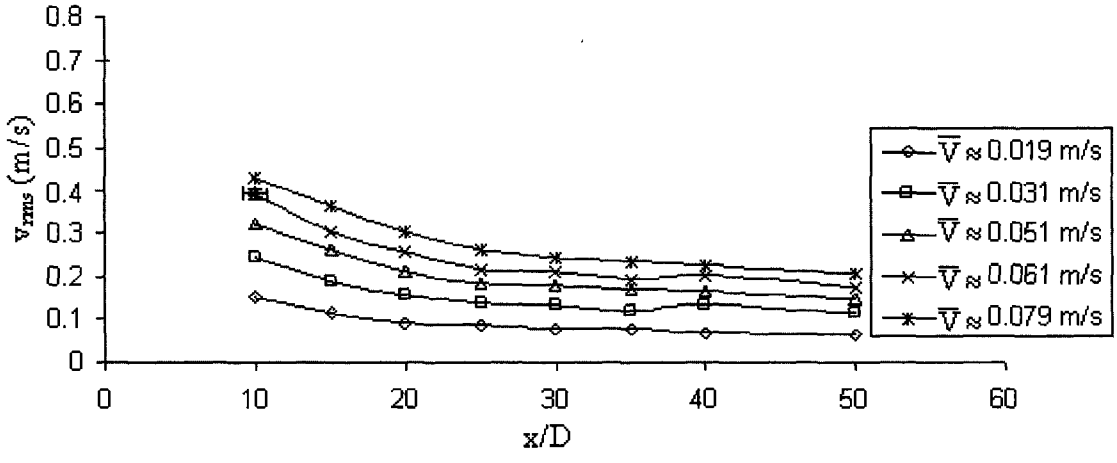

(c) Plate D = 50 mm

Figure F.4: Variation of rms velocity (m/s) in y direction with respect to (x/D) in 2D hot-wire measurement: (a) with perforated plate D-25 (b) with perforated plate D-37.5 and (c) with perforated plate D-50

APPENDIX G: DETAILS OF SPHERE SIZE IN RESULTS

G.1 THE RESULTS OF PVC SPHERES

G.1.1 EFFECT OF INTEGRAL LENGTH SCALE AND RELATIVE INTEGRAL LENGTH SCALE

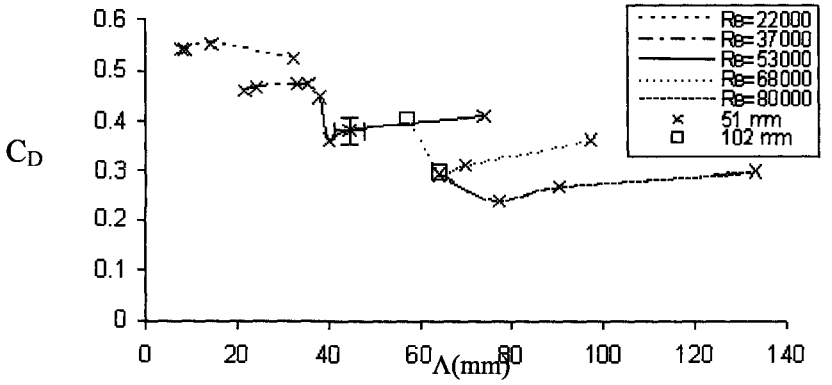

(a) Tu = 2.5%

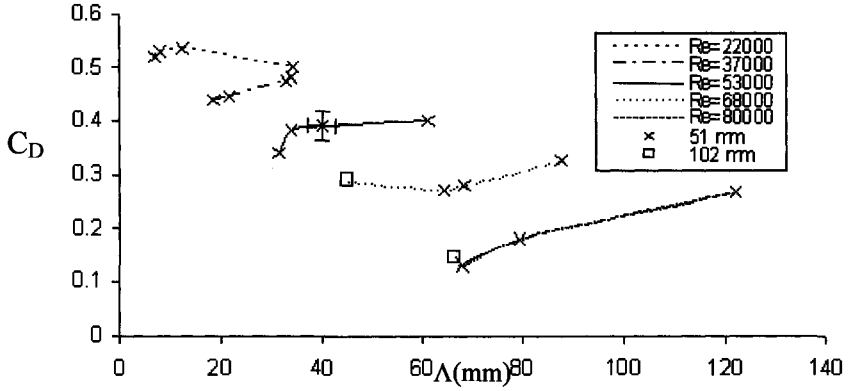

(b) Tu = 4%

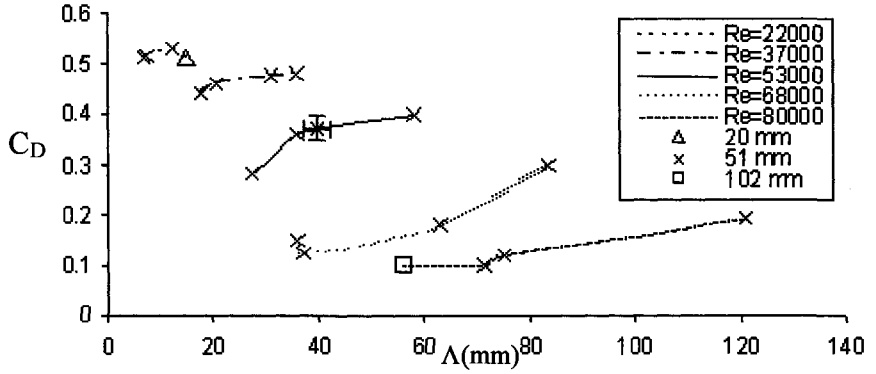

(c) Tu=6.3%

Figure G.1: Impact of integral length scale on PVC sphere drag when (a) Tu = 2.5% (b) Tu = 4% (c) Tu = 6.3%

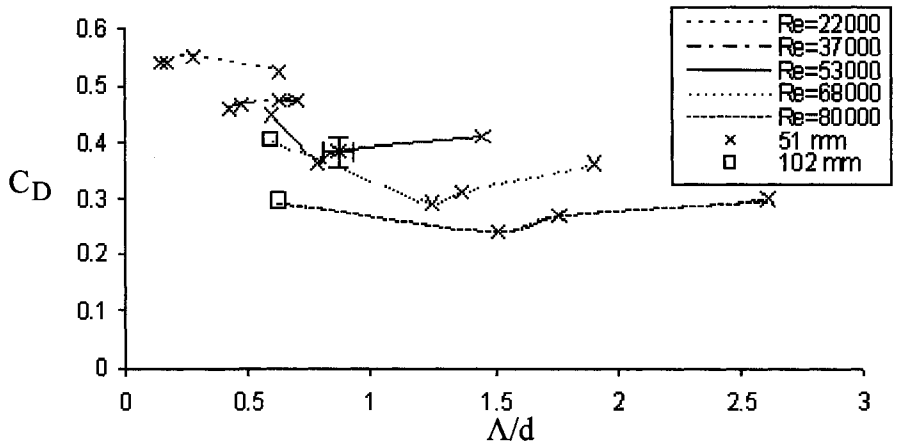

(a) Tu = 2.5%

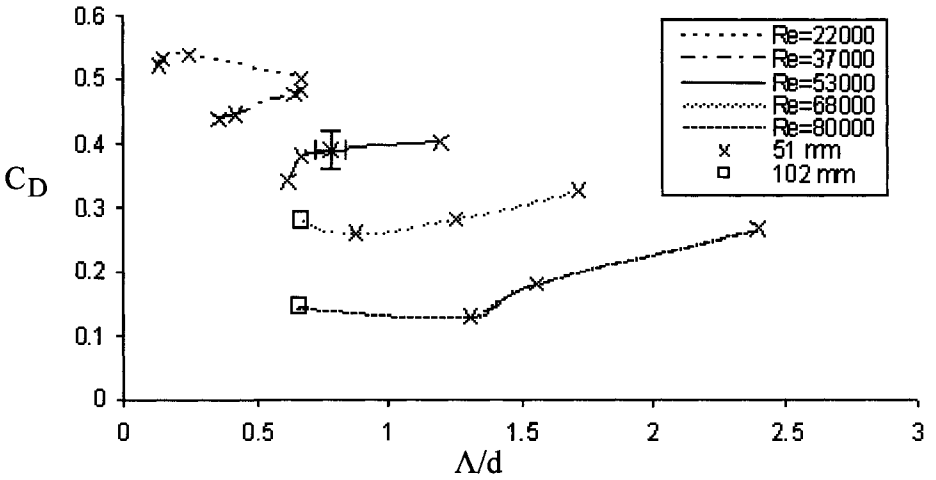

(b) Tu = 4%

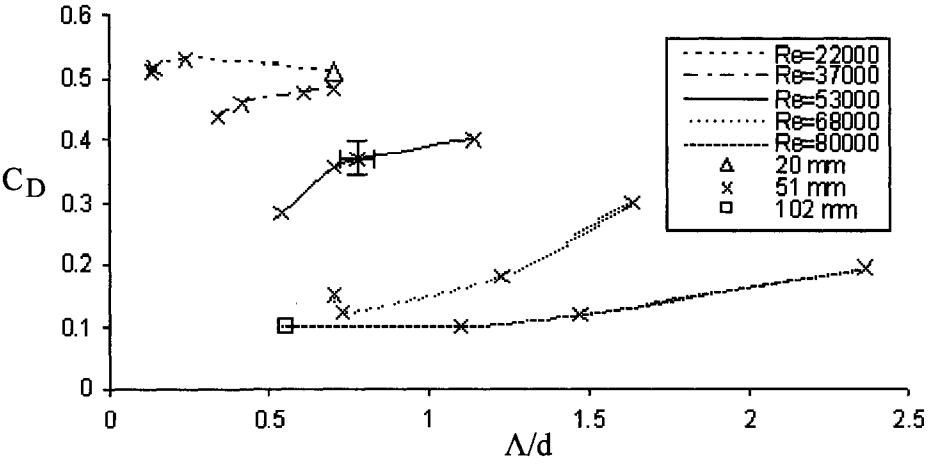

(c) Tu = 6.3%

Figure G.2: Impact of relative integral length scale on PVC sphere drag when (a) Tu = 2.5% (b) Tu = 4% (c) Tu = 6.3%

G.1.2 EFFECT OF TURBULENCE INTENSITY

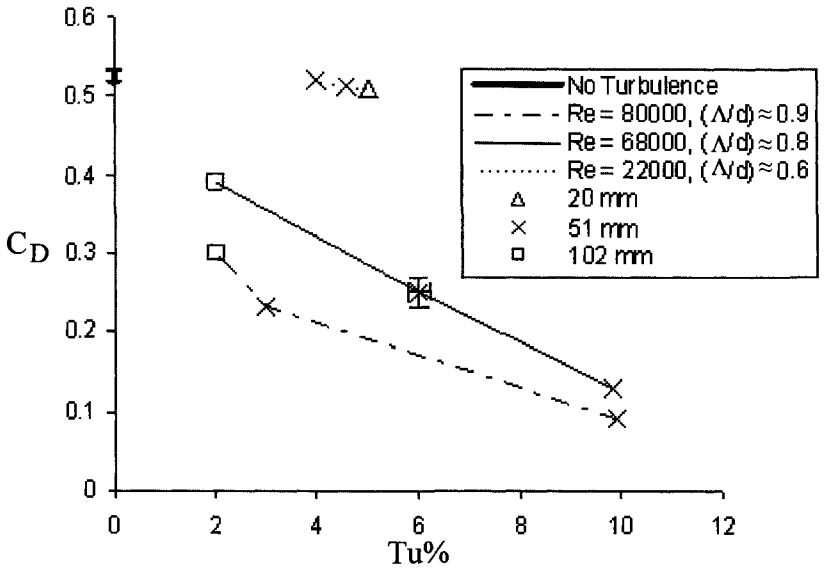

Figure G.3: Impact of turbulence intensity on PVC sphere drag

G.1.3 EFFECT OF REYNOLDS NUMBER

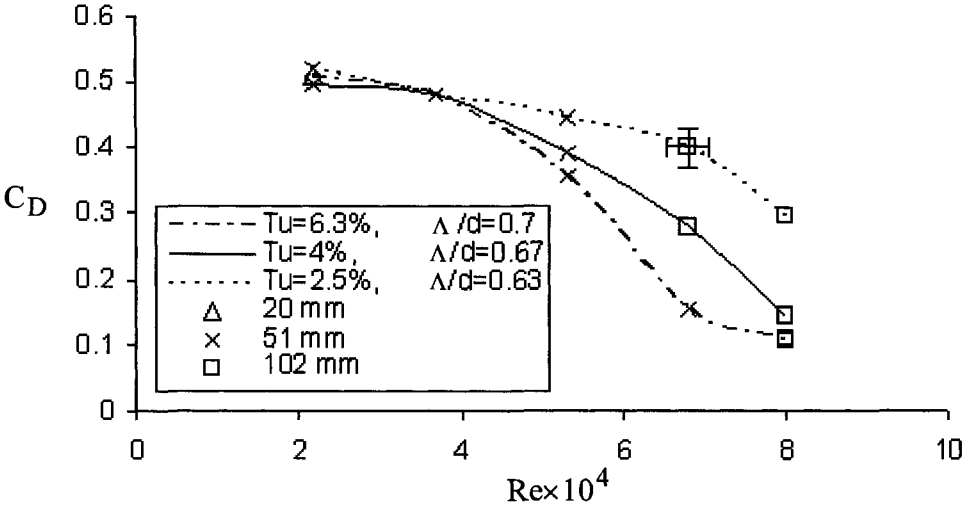

Figure G.4: Impact of Reynolds number on PVC sphere drag

G.2 THE RESULTS OF WOODEN SPHERES

G.2.1 EFFECT OF RELATIVE INTEGRAL LENGTH SCALE

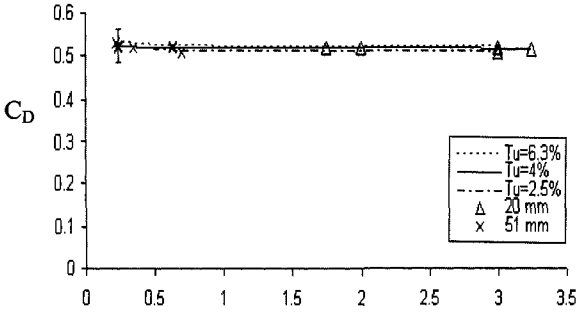

(a) Re = 2.2×10^4

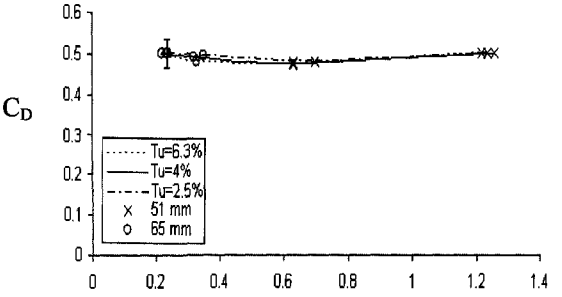

(b) Re = 3.7×10^4

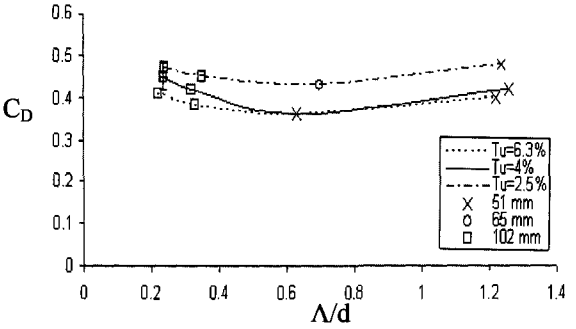

(c) Re = 5.3×10^4

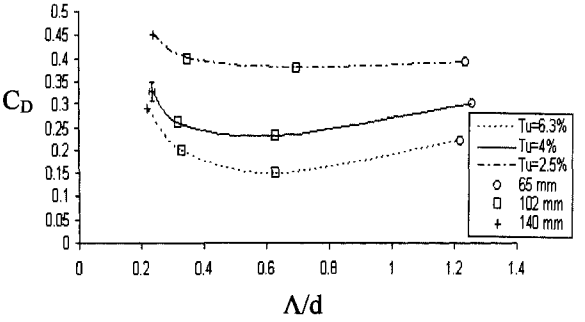

(d) Re = 6.8×10^4

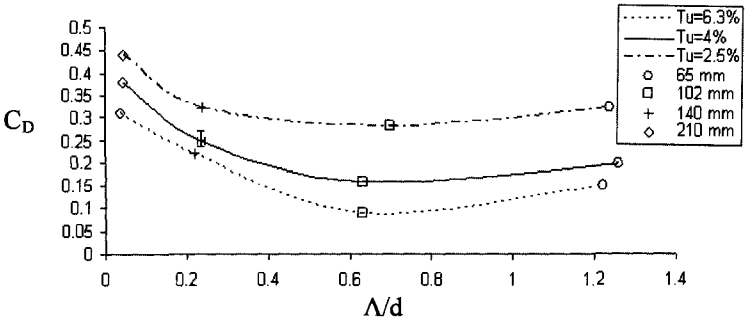

(e) Re = 8×10^4

Figure G.5: Impact of relative integral length scale on wooden sphere drag when (a) Tu = 2.5% (b) Tu = 4% (c) Tu = 6.3%

G.2.2 EFFECT OF TURBULENCE INTENSITY

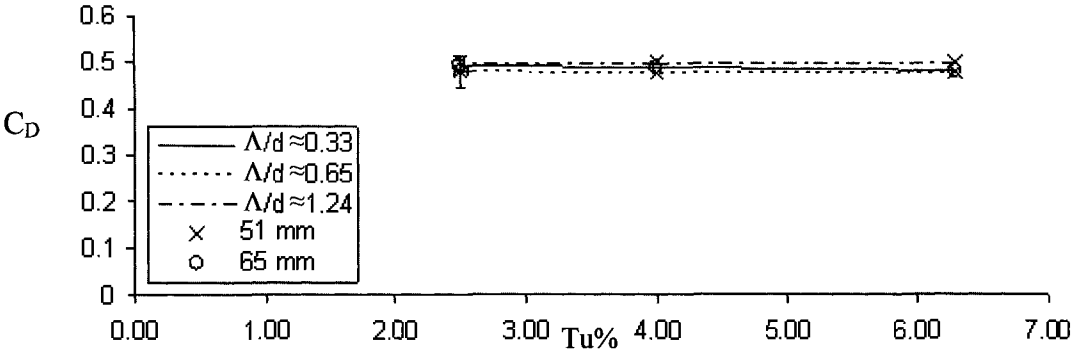

(a) Re = 3.7×10^4

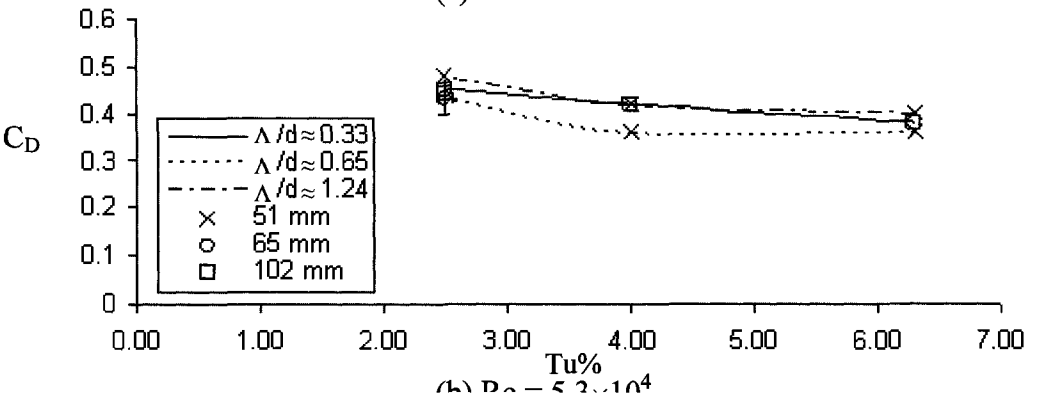

(b) Re = 5.2×10^4

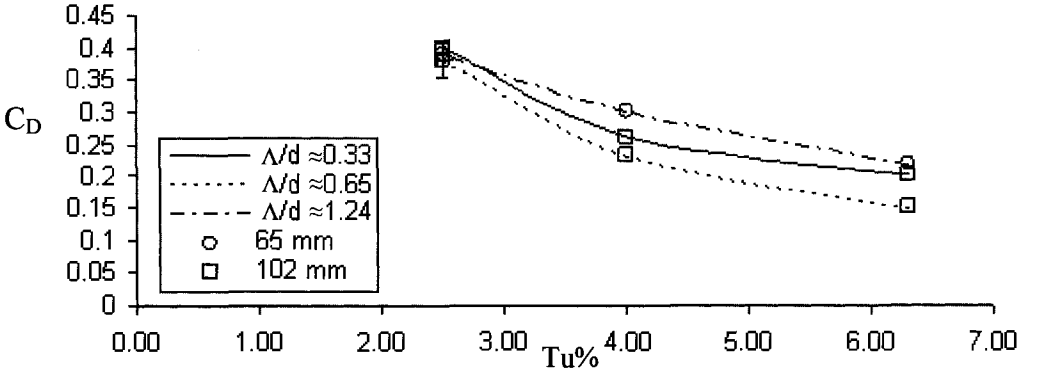

(c) Re = 6.8×10^4

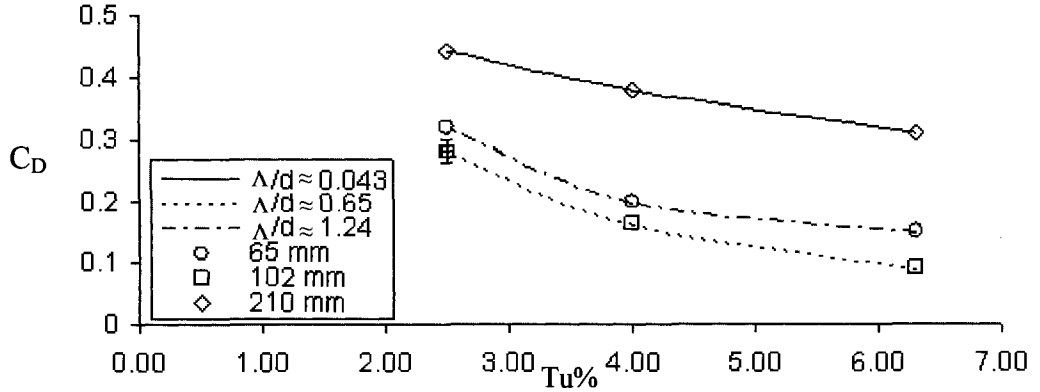

(d) Re = 8×10^4

Figure G.6: Impact of turbulence intensity on wooden sphere drag

G.2.3 EFFECT OF REYNOLDS NUMBER

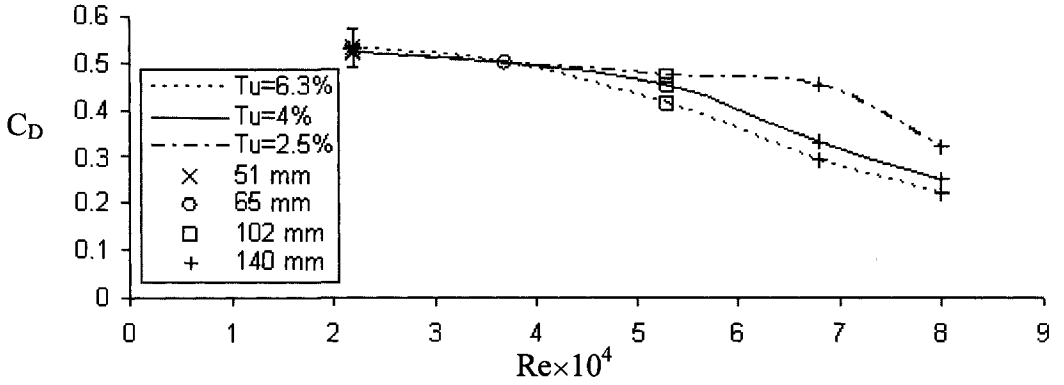

(a) $\Lambda/d \approx 0.22$ ($\Lambda/d = 0.21 \sim 0.26$)

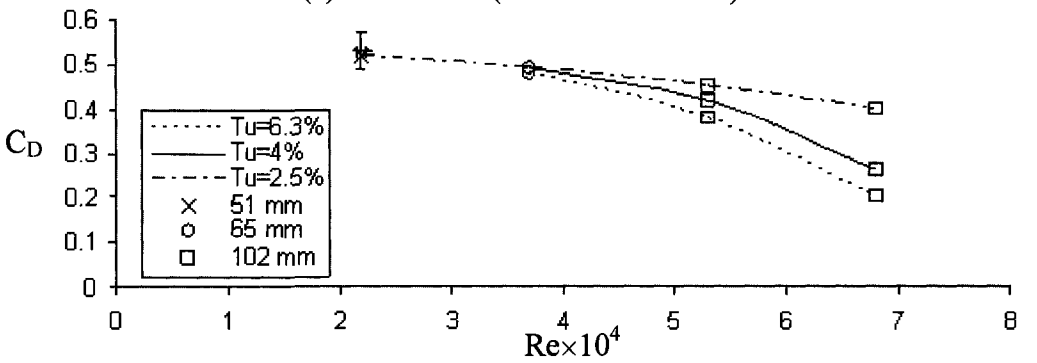

(b) $\Lambda/d \approx 0.33$ ($\Lambda/d = 0.3 \sim 0.35$)

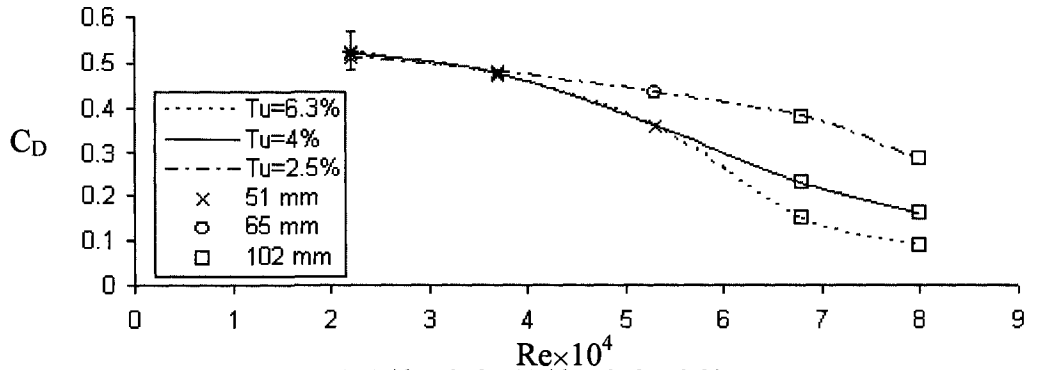

(c) $\Lambda/d \approx 0.65$ ($\Lambda/d = 0.6 \sim 0.7$)

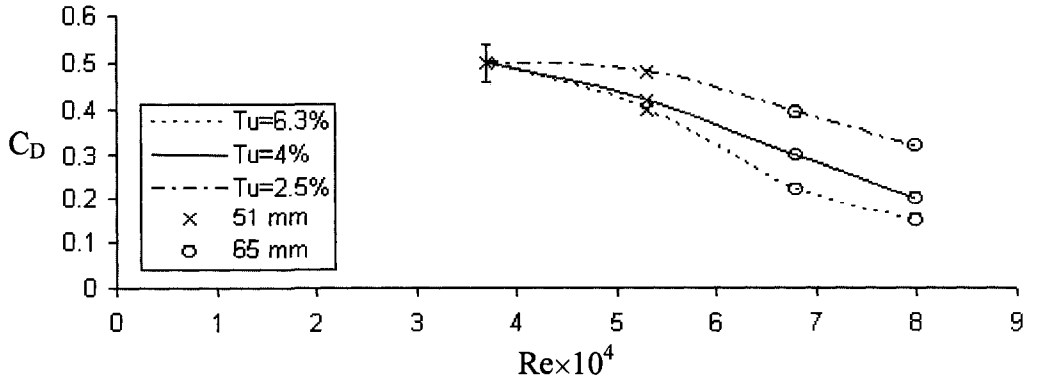

(d) $\Lambda/d \approx 1.2$ ($\Lambda/d = 1.12 \sim 1.35$)

Figure G.7: Impact of Reynolds number on wooden sphere drag

APPENDIX H: FREE BODY DIAGRAM OF THE SPHERE

As mentioned in Section 3.3, the sphere was supported by 8 strings. There were 4 symmetrical strings on the top, each making an angle of $\alpha \pm 0.3°$ with respect to the test section wall and $\beta \pm 0.3°$ to the streamwise direction of the wind tunnel. And, there were 4 symmetrical strings at the bottom, each making an angle of $\alpha' \pm 0.3°$ with respect to the test section floor and $\beta' \pm 0.3°$ to the streamwise direction of the wind tunnel. Each string resists a force; see Figures H.1.

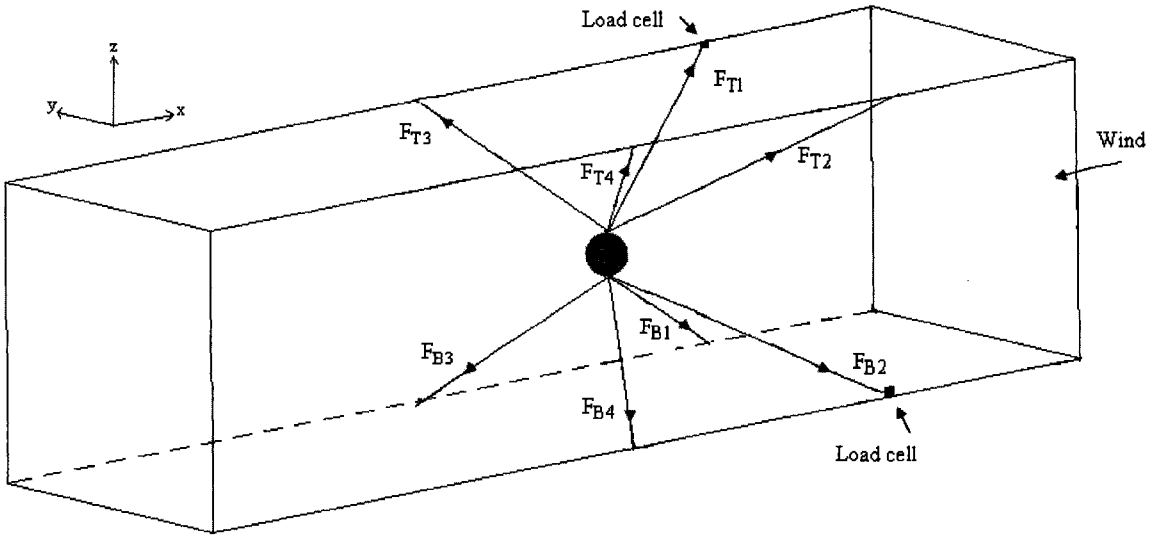

Figure H.1: Schematic of net forces of the strings in the sphere and load cell setup

H.1 'NO FLOW' CONDITION

Due to symmetry, force because of the weight of the sphere in each of the top strings equals to each other, and same applies to those in the bottom strings i.e.

$$F_{T1} = F_{T2} = F_{T3} = F_{T4} \tag{H.1}$$

$$F_{B1} = F_{B2} = F_{B3} = F_{B4} \tag{H.2}$$

In this situation, the load cell in one of the top or bottom strings was set to zero. Every time when the loadcell is connected to the top or bottom string as shown in figure H.1, the output was set to zero before the wind tunnel is turned on. In fact, it is adjusted to assume all the net forces before turning the wind tunnel on is zero.

$$F_{T1} = F_{T2} = F_{T3} = F_{T4} = F_{B1} = F_{B2} = F_{B3} = F_{B4} = 0 \tag{H.3}$$

H.2 IN THE PRESENCE OF FLOW

Base on the definition of the coordinate system as portrayed in Figure H.2, the flow pushes the sphere in the negative x direction. Thus, the upstream strings resist the force and the downstream strings become loose. Due to the symmetrical setup the force is resisted by upstream top strings, F_{T1} and F_{T2} equals to each other. Then, because of same reason we have $F_{T3} = F_{T4}$, $F_{B1} = F_{B2}$ and $F_{B3} = F_{B4}$. Figure H.2 shows the component of flow force in x direction for top strings 1 and 3. The calculation of the drag force in top strings 2 and 4 are similar to the top strings 1 and 3.

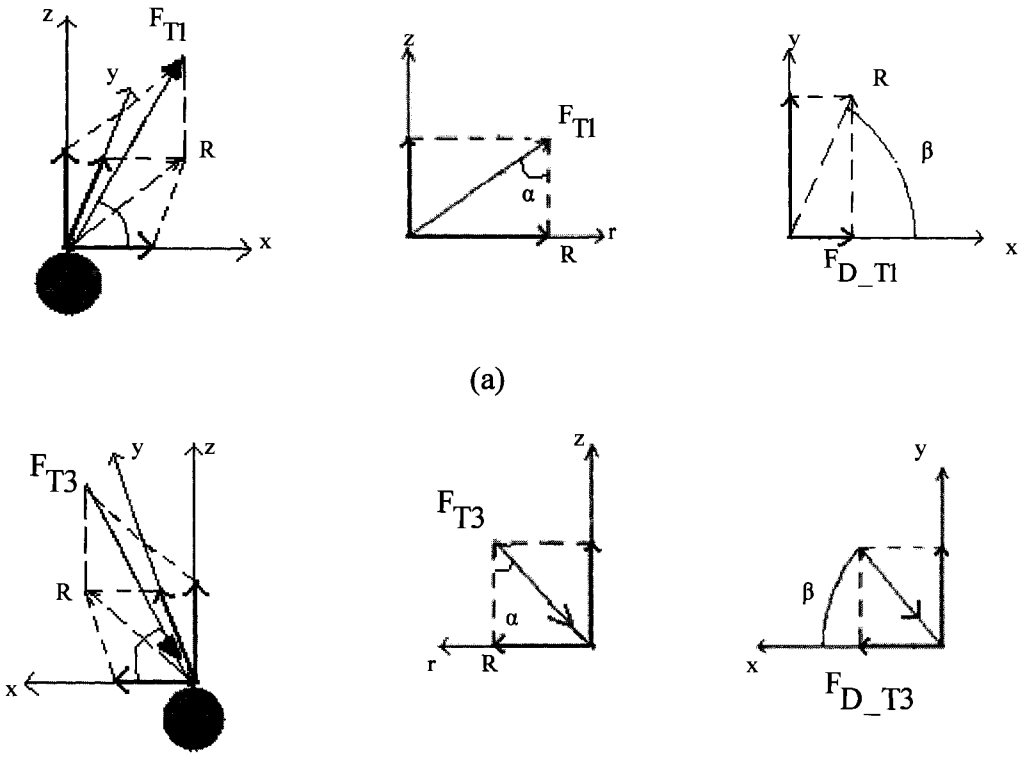

Figure H.2: Decomposition of forces in the top strings

The downstream strings have negative forces because of getting loose in wind. These negative values affect the positive forces of upstream strings. Thus, in reality the force measured in upstream strings includes the force in downstream strings, too. Therefore, in the experiments, to measure the drag force, only the forces in upstream strings were measured. And, due to the geometrical symmetric setup, one time load cell

was connected to one of the top upstream strings and one time to one of the bottom upstream strings.

VITA AUCTORIS

NAME:	Niloofar Moradian
PLACE OF BIRTH:	Isfahan, Iran
YEAR OF BIRTH:	1983
EDUCATION	National Organization for Development of Exceptional Talents(NODET) High School, Isfahan, Iran 1997-2001
	Isfahan University of Technology, Isfahan, Iran 2001-2005 B.Sc.
	University of Windsor, Windsor, Ontario, Canada 2006-2008 M.Sc
	McGill University, Montreal, Quebec, Canada 2008-N/A Ph.D.

LIST OF PUBLICATIONS

4- Moradian, N., Ting, D. S-K, Cheng, S., "Advancing the Drag Crisis of a Sphere via Integral Length Manipulation," Journal of Fluids Engineering (under preparation).

3- Moradian, N., Ting, D. S-K, Cheng, S., 6-8 June 2008, "The role of integral length scale on freestream turbulence effect on the drag of a sphere," *The Canadian Society of Mechanical Engineers (CSME – Forum)*, Ottawa, Canada.

2- Moradian, N., Ting, D. S-K, Cheng, S., "The effects of freestream turbulence on drag coefficient of a solid sphere," Experimental Thermal and Fluid Science (submitted).

1- Moradian, N., Ting, D. S-K, Cheng, S., 3-7June 2007, "The drag of a solid sphere in freestream turbulence," *The 21st Canadian Congress of Applied Mechanics (CANCAM)*, Toronto, Canada.